UNIVERSITÀ DEGLI STUDI DI TRIESTE

XXVIII CICLO DEL DOTTORATO DI RICERCA IN
NANOTECNOLOGIE

IN SITU AND IN OPERANDO STUDY OF GRAPHENE GROWTH AND PROPERTIES ON METAL SURFACES

settore scientifico-disciplinare: FIS/03 - Fisica della Materia

DOTTORANDO:
Laerte Luigi PATERA

COORDINATORE:
Prof. Lucia PASQUATO

SUPERVISORE DI TESI:
Dr. Cristina AFRICH

Academic year 2014-2015

UNIVERSITÀ DEGLI STUDI DI TRIESTE

XXVIII CICLO DEL DOTTORATO DI RICERCA IN
NANOTECNOLOGIE

IN SITU AND IN OPERANDO STUDY OF GRAPHENE GROWTH AND PROPERTIES ON METAL SURFACES

settore scientifico-disciplinare: FIS/03 - Fisica della Materia

DOTTORANDO:
Laerte Luigi PATERA

COORDINATORE:
Prof. Lucia PASQUATO

SUPERVISORE DI TESI:
Dr. Cristina AFRICH

Academic year 2014-2015

Abstract

Graphene, a single layer of C atoms, has been recently proposed as a good candidate for post-silicon technology, providing a new platform that could allow improving electronic device performances, as described by the Moore's Law. Chemical Vapour Deposition (CVD) is a suitable synthesis method for large-scale production of high quality graphene. This process exploits the catalytic activity of transition metal surfaces in dissociating hydrocarbon molecules.
Among the possible catalysts, Ni is an appealing choice, due to the low price and the possibility to obtain graphene layers at temperature as low as 450 °C. From a more fundamental point of view, graphene growth on the (111) surface of Ni represents a peculiar case of lattice-matching, being a good model system for the study of the substrate effects on graphene properties.
In this thesis, we study the growth process, the morphology and the electronic properties of graphene on Ni(111), by means of Scanning Tunneling Microscopy (STM), Photo-Emission Spectroscopy (PES) and spectro-microscopy techniques. First, the different graphene structures are identified through a combined experimental and theoretical approach, revealing the coexistence of three epitaxial adsorption geometries and the possibility to obtain graphene domains that exhibit a rotation with respect to the underlying substrate. Band structure mapping reveals specific changes in the electronic properties, depending on the degree of graphene orbital hybridization with the metal.
Based on these findings, graphene growth is investigated by *in situ* STM and XPS, clarifying the atomistic mechanisms under different experimental conditions and assessing the crucial roles played by surface carbide and C-contamination. In particular, we study the correlation between the CVD parameters, the growth process and the final graphene structures, being able to provide recipes for the synthesis of graphene layers with tailored morphologies.
The atomic structure of graphene edges is studied, both during growth, by means of high-speed STM measurements, and after cooling down to room temperature, addressing the importance of dangling bonds passivation. Then, employing the video-rate capability of our STM system, we identify the active sites for C attachment during growth, revealing the role of Ni adatoms.
Next, intrinsic defective structures are examined at the atomic scale by STM and *ab-initio* calculations, showing the presence of substitutional Ni adatoms trapped in the graphene matrix, as well as grain boundaries and lattice distor-

tions.
Finally, the growth and electronic properties of bi-layer graphene are investigated, suggesting the intriguing possibility to exploit the lattice match between graphene and Ni(111) to limit the formation to two layers only.

Sommario

Il grafene, un singolo strato di atomi di carbonio, è stato recentemente proposto come un buon candidato per la tecnologia post-silicio, fornendo una piattaforma che permetterebbe di migliorare le prestazioni di dispositivi elettronici, come descritto dalla legge di Moore. La produzione su larga scala di grafene di alta qualità è tipicamente effettuata attraverso la deposizione da vapori chimici (CVD). Questo processo sfrutta l'attività catalitica delle superfici di metalli di transizione per dissociare molecole di idrocarburi. Tra i possibili catalizzatori, il nichel è particolarmente interessante, per il suo basso costo e per la possibilità di ottenere strati di grafene a temperature a partire da 450 °C. Da un punto di vista di ricerca fondamentale, la crescita di grafene sulla superficie (111) del nichel rappresenta inoltre un caso particolare di epitassia, offrendo un buon modello per lo studio degli effetti del substrato sulle proprietà del grafene.
In questa tesi, si sono studiati il processo di crescita, la morfologia e le proprietà elettroniche del grafene su Ni(111), mediante microscopia a scansione ad effetto tunnel (STM), spettroscopia di foto-emissione da raggi X (XPS) e tecniche di spettro-microscopia.
Nella prima parte, le diverse strutture di grafene sono identificate tramite un approccio combinato sperimentale e teorico, rivelando la coesistenza di tre geometrie di adsorbimento epitassiale e la possibilità di ottenere domini di grafene che presentano una rotazione rispetto al substrato. La mappatura della struttura a bande rivela cambiamenti importanti nelle proprietà elettroniche delle diverse fasi, a seconda del grado di ibridazione degli orbitali del grafene con il metallo.
Sulla base di questi risultati, la crescita del grafene è indagata tramite *in situ* STM e XPS, in modo da chiarire i meccanismi in diverse condizioni sperimentali e valutare il ruolo cruciale svolto dal carburo di superficie e dalla contaminazione di carbonio. In particolare, si è studiata la correlazione tra i parametri di CVD, il processo di crescita e le strutture di grafene finali, fornendo ricette utili per la sintesi di strati di grafene con morfologie specifiche.
La struttura atomica dei bordi delle isole di grafene è studiata sia durante la crescita, mediante misure STM ad alta velocità, che dopo il raffreddamento a temperatura ambiente, dimostrando l'importanza della passivazione dei legami non saturi. Successivamente, utilizzando la capacità del nostro sistema STM di acquisire filmati a *video-rate*, abbiamo identificato i siti attivi per l'attaccamen-

to di carbonio durante la crescita, rivelando il ruolo fondamentale giocato dalla presenza di adatomi di nichel. La struttura dei difetti intrinseci è esaminata su scala atomica tramite STM e calcoli *ab-initio*, rivelando la presenza di adatomi di nichel intrappolati nella matrice di grafene, così come di bordi di grano e distorsioni reticolari.
Infine, sono studiate la crescita e le proprietà elettroniche del grafene bi-strato, suggerendo la possibilità di sfruttare l'epitassia tra grafene e Ni(111) per limitare la formazione a due soli strati.

Contents

Chapter 1

Introduction

Graphene is a single layer of carbon atoms, tightly packed in a hexagonal honeycomb lattice. Due to its peculiar band structure, with electrons behaving like massless particles, in the recent years graphene attracted the attention of the scientific community, being an extraordinary platform to study quantum effects in condensed matter.[1] Moreover, properties like the remarkable electron mobility at room temperature,[2] a Young's modulus of 1 TPa[3] and the very high thermal conductivity[4] make graphene appealing for an almost limitless number of technological applications.
Nevertheless, the commercial exploitation of this material calls for a suitable production method, able to sustain mass-scale production. Chemical vapor deposition (CVD), a process exploiting the catalytic activity of transition metal surfaces in dissociating hydrocarbon molecules, is widely seen as the most versatile and promising technique for this purpose,[5] as shown by the recently reported production of 30-inch graphene films on copper foils.[6] However, a clear comprehension of the mechanisms governing the graphene growth is still missing, limiting further improvements. Concerning the catalyst choice, despite polycrystalline copper represents at the moment the best candidate for a potential large-scale production, Ni captured the attention thanks to its high catalytic activity, which allows the synthesis of high quality graphene at temperature as low as 450 °C.[7]
In order to improve the understanding of the atomistic mechanisms underlying the CVD process, the usage of model catalysts has been shown to provide helpful information. Indeed, since the early stages of surface science, well-defined single crystal surfaces were extensively used to mimic the situation occurring on real operating catalysts. To this purpose, we chose the Ni(111) surface as a model substrate for catalytic graphene growth on Ni, since this facet is the most stable one. Furthermore, on this substrate the lattice constant is very close to the graphene's one, allowing for a pure epitaxial growth.
In this thesis, we used different state-of-the-art surface science techniques, combined with Density Functional Theory (DFT) calculations, in order to invest-

igate not only the structural and electronic properties, but also the atomistic growth mechanisms, clarifying the overall picture on this system. Scanning Tunneling Microscopy (STM) has been used to characterize the graphene morphology at the atomic-scale, as well as the growth mechanisms at high temperatures and during hydrocarbon exposure. X-ray Photoelectron Spectroscopy (XPS) provided complementary information on the chemical signatures of the structures involved in the growth process and of the final graphene phases. Cathode lens spectro-microscopy measurements allowed characterizing the coexisting graphene structures on the meso-scale, giving access also to the electronic dispersion along the K point.
All the growth measurements were performed *in situ* under *in operando* conditions, i.e. monitoring the surface evolution at high temperature and during hydrocarbon exposure. This approach represents a major difference compared to most of the literature studies on this topic, where measurements are conducted after cooling down to RT.[8,9] Moreover, the video-rate capability of the FAST module, coupled with our VT-STM, allowed us to characterize details of the growth mechanisms not attainable with standard STM systems, revealing transition steps and rapidly-evolving structures involved in graphene formation processes, which are typically not present under post-reaction conditions.
The aim of this work is to explore the possibility to devise a strategy for the synthesis of graphene layers with tailored properties. In order to obtain such result, it is first of all necessary to thoroughly characterize the structural and electronic properties of all the graphene phases that can contribute to the final layer. Then, it is fundamental to unveil the different growth mechanisms that drive graphene formation down to the atomic level and how these are influenced by CVD and external parameters.
In Chapter 2, a brief introduction to graphene properties and production methods is given. In part I, the different experimental techniques are introduced. The main results of the thesis are described in part II. Chapter 6 presents a detailed structural characterization of the different graphene phases. In Chapter 7, we investigate the phases shown in the previous Chapter, by means of spectro-microscopy measurements, providing a clear spectroscopy characterization. In Chapter 8 we study graphene growth mechanisms in a temperature range between 400 and 600 °C, by means of *in situ* STM and XPS, assessing the role of surface carbide and of the near-surface C concentration. In Chapter 9, we report the edge morphology of EG islands grown on top of a Ni terrace. By means of high-speed STM, we compare the structures present during growth and after cooling down to RT, focusing on the changes in dangling bonds passivation. In Chapter 10, we exploit the capability of the FAST module (described in Chapter 3) to acquire atom-resolved images above video-rate. In this way, we report for the first time the mechanism involved in the attachment of C atoms at the growing edges, unveiling the important role of Ni adatoms.
Then, in Chapter 11, we investigate graphene defects originating from the growth process, revealing the presence of several different structures. Chapter 12 is de-

voted to the study of the growth and the electronic properties of bi-layer graphene (BLG). *In situ* spectro-microscopy measurements allow clarifying the formation process, providing a characterization of the top-layer band structure. In Chapter 13, the thesis is summarized and perspectives for future investigations are given.

Most of the work presented in this thesis has been done in Trieste, at the CNR-IOM, Laboratorio TASC, where the STM system is housed. Spectro-microscopy measurements were performed at the Nanospectroscopy beamline (Elettra Sincrotrone Trieste), while the high-pressure XPS ones were carried out at the ISISS beamline (BESSY II Synchrotron, Berlin). DFT calculation have been performed by the group of Prof. Maria Peressi (University of Trieste).

Chapter 2

Graphene

In this chapter we review relevant aspects of graphene research that motivated the scientific project described in this thesis. First, we introduce graphene and its peculiar electronic properties. Then, the main production techniques will be presented, focusing on Chemical Vapour Deposition (CVD), in particular on Ni substrates.

2.1 Free-standing graphene

Graphene displays a honeycomb lattice of C atoms, as shown in Figure 2.1, that can be seen as a triangular lattice with a basis of two atoms per unit cell.[10] The lattice vectors can be written as:

$$\mathbf{a_1} = \frac{a}{2}(3, \sqrt{3}), \quad \mathbf{a_2} = \frac{a}{2}(3, -\sqrt{3}), \tag{2.1}$$

where a is the C-C distance ($\simeq$ 1.42 Å). The reciprocal lattice vectors can be expressed as:

$$\mathbf{b_1} = \frac{2\pi}{3a}(1, \sqrt{3}), \quad \mathbf{b_2} = \frac{2\pi}{3a}(1, -\sqrt{3}), \tag{2.2}$$

The two points K and K' at the corners of the graphene Brillouin zone (BZ) are of particular importance for the physics of graphene and they are named Dirac

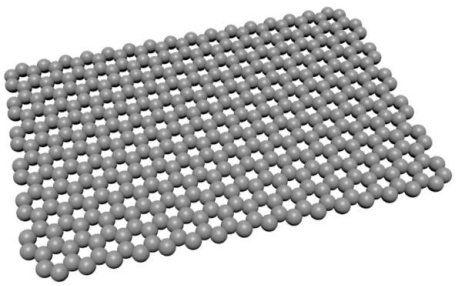

Figure 2.1: Free-standing graphene.

points. Their positions in momentum space are given by:

$$\mathbf{K} = \left(\frac{2\pi}{3a}, \frac{2\pi}{3\sqrt{3}a}\right), \quad \mathbf{K}' = \left(\frac{2\pi}{3a}, -\frac{2\pi}{3\sqrt{3}a}\right). \tag{2.3}$$

The tight-binding Hamiltonian for electrons in graphene, considering that electrons can hop to both nearest- and next-nearest-neighbor atoms, has the form (units choosen such that $\hbar = 1$)

$$H = -t \sum_{<i,j>,\sigma} \left(a^{\dagger}_{\sigma,i}, b_{\sigma,j} + H.c.\right) - \quad t' \sum_{<<i,j>>,\sigma} \left(a^{\dagger}_{\sigma,i} a_{\sigma,j}, b^{\dagger}_{\sigma,i} b_{\sigma,j} + H.c.\right), \tag{2.4}$$

where $a_{i,\sigma}$ ($a^{\dagger}_{i,\sigma}$) annihilates (creates) an electron with spin σ ($\sigma = \uparrow, \downarrow$) on site $\mathbf{R_i}$ on sublattice A (an equivalent definition is used for sublattice B), t (~ 2.8 eV) is the nearest-neighbor hopping energy between different sublattices, and t' is the next nearest-neighbor hopping energy in the same sublattice. The energy bands derived from this Hamiltonian have the form:[11]

$$E_{\pm}(\mathbf{k}) = \pm t\sqrt{3 + f(\mathbf{k})} - t' f(\mathbf{k}) \tag{2.5}$$

$$f(\mathbf{k}) = 2\cos(\sqrt{3}k_y a) + 4\cos\left(\frac{\sqrt{3}}{2}k_y a\right)\cos\left(\frac{3}{2}k_x a\right), \tag{2.6}$$

where the plus sign applies to the upper (π^*) and the minus sign the lower π band. It is clear from equation 2.5 that the spectrum is symmetric around zero energy if t' = 0. For finite values of t', the electron-hole symmetry is broken and the π and π^* bands become asymmetric.

In Figure 2.2, the full band structure of graphene with both t and t' is shown. In

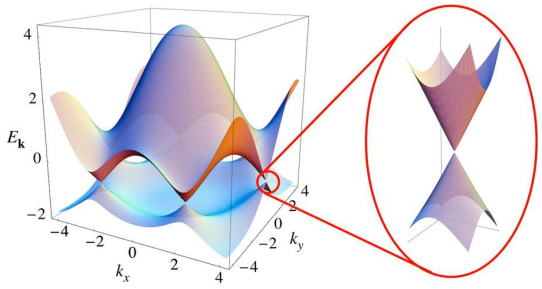

Figure 2.2: Electronic dispersion in the honeycomb lattice. Left: energy spectrum (in units of t) for finite values of t and t', with t = 2.7 eV and t' = -0.2 t. Right: zoom in of the energy bands close to one of the Dirac points. Reproduced and adapted from Castro Neto et al. [10]

the same figure, it is also shown a zoom on the band structure close to one of the Dirac points (ie. K or K'). This dispersion can be approximated by expanding the full band structure,[11] equation 2.5, close to the $\mathbf{K}$ (or $\mathbf{K}'$) vector, equation 2.3, as $\mathbf{k} = \mathbf{K} + \mathbf{q}$, with $|\mathbf{q}| \ll \mathbf{K}$:

$$E_{\pm}(\mathbf{q}) = \pm v_F |\mathbf{q}| + O[(q/K)^2], \tag{2.7}$$

where **q** is the momentum measured with respect to to the Dirac points and v_F is the Fermi velocity, given by $v_F = 3ta/2$, with a value $v_F \simeq 1 \times 10^6$ m/s.
Due to this peculiar electronic behavior, graphene shows several interesting properties: extremely high room temperature electron mobility ($2.5 \times 10^5\ cm^2 V^{-1} s^{-1}$);[2] a Young's modulus of 1 TPa and intrinsic strength of 130 GPa;[3] very high thermal conductivity (above 3,000 WmK^{-1});[4] optical absorption of $\simeq$ 2.3% in the infrared limit;[12] impermeability to any gases;[13] ability to sustain extremely high densities of electric current (a million times higher than Cu).[14] Another property of graphene, already demonstrated,[15] is that it can be readily chemically functionalized.[16]

2.2 Production methods

The appealing possibility to exploit graphene properties in next generation technology devices requires the development of adequate scalable synthesis processes that can sustain mass-scale production.[5] Specific requirements on graphene characteristics can be achieved by a suitable choice of the production method, as shown in Figure 2.3. In the following, the main methods currently available to obtain graphene flakes with various dimensions, shapes and quality will be presented.

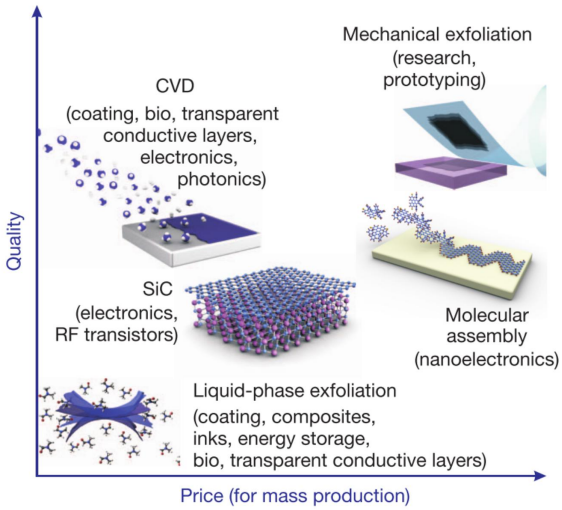

Figure 2.3: Graphene production methods, classified by price for mass production and quality. Reproduced from Novoselov et al.[5]

2.2.1 Liquid-phase exfoliation

Liquid-phase graphite exfoliation can be achieved by exposure of the sample to a non-aqueous solvent having a surface tension that favors an increase in the

total area of graphite flakes dispersed in the aqueous solution.[17] By means of sonication treatments, graphite is split in thinner platelets, with a significant fraction of monolayer flakes in the suspension, which can be further enriched by centrifugation.[18] A similar approach can be exploited using graphite oxide, where graphite pellets are first oxidized and then ultrasonically exfoliated in an aqueous solution.[19] After centrifugation treatment, the solution can be deposited as a thin film on almost any surface and partially reduced.
Even if the resulting material is composed mainly by few-layer graphene flakes, it still preserves many of the appealing properties of single-layer graphene and can be successfully used for several application, such as graphene based paints and ink-jet printed conductive circuits.[20]

2.2.2 Silicon carbide graphitization

Graphitic layers can be grown either on Si or C faces of a Silicon carbide (SiC) wafer.[21] This process is based on element-specific decomposition of the SiC surface at high temperature: indeed, while C atoms are stable at temperatures even higher than 2,000 °C, Si evaporates between 1,000 and 1,500 °C.[22,23] Initially, the C-terminated face of SiC was used to grow polycrystalline multi-layers,[24] but recently it has been shown that the number of graphene layers can be properly tuned.[25] The quality of such graphene can be very high, with flake size approaching hundreds of micrometers.[26] The major drawbacks of this approach are the high cost of the SiC wafers and the high temperatures required (above 1,000 °C), which are not directly compatible with silicon electronics production, and the low degree of uniformity, due to a preferential multilayer formation at the step-edges.

2.2.3 Molecular assembly

Surface-assisted polymerization of specific organic molecules can be exploited in order to synthesize graphene nano-ribbons with tunable width and edges structure.[27–29] This bottom-up approach allows opening a band gap up to 2.5 eV in graphene nanostructures,[28] being promising for the integration in field-effect transistors.[30] Nevertheless, this fabrication approach is not cost-effective and presents several limitation, such as the requirement of high-vacuum conditions and atomically flat metal substrates. For this reason it is unlikely that it will become commercially viable in the next decade.

2.2.4 Chemical Vapour Deposition

Chemical Vapour Deposition (CVD) exploits the catalytic decomposition of hydrocarbon molecules on metallic surfaces, yielding formation of extended graphene layers.[31] Large-areas of poly-crystalline monolayer graphene films have been synthesized on copper foils,[6] being promising for several applications where

high-quality graphene is required.[32] Even though the complete process typically requires transfering from the metal support to a dielectric surface,[33] the production of graphene with lateral dimensions up to a meter has already been achieved.[6] CVD films show transport properties equivalent to those of exfoliated graphene on both SiO_2 and hexagonal boron-nitride substrates (see Figure 2.3). Despite the presence of defects, domain boundaries, presence of mul-

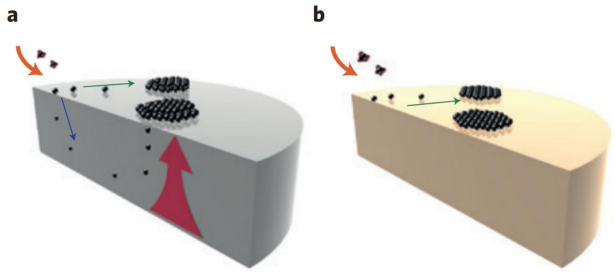

Figure 2.4: Schematic illustration of elementary steps involved in the CVD process through (a) bulk mediated growth and (b) surface growth. The orange arrow represents the introduction of precursor, the blue arrow indicates the dissolution of C species, the magenta arrow represents the subsequent segregation from the bulk and the green arrow denotes the surface-catalytic process. Reproduced and adapted from Lin et al.[34]

tilayer, such materials already match the requirements for the use in transparent conductive coating applications.
Recently, graphene growth has been successfully demonstrated on several transition metal surfaces,[35,36] such as Ni, Co, Fe, Cu, Pd, Pt, Ir, Rh, Re and Ru. Depending on the level of C solubility in the metal, the growth process can occur through two different pathways,[34] schematized in Figure 2.4:

- *Bulk-mediated growth*
  C atoms originating from hydrocarbons decomposition diffuse on the surface and dissolve into the catalyst bulk, due to the high C solubility. Once C supersaturation level is reached, they segregate on the surface, leading to graphene islands nucleation and growth. This is the case of Ni, Co, Pt, Rh and Re surfaces.

- *Surface growth*
  upon hydrocarbon dissociation, C remains on the surface and aggregates to form graphene flakes. On Cu and Ir surfaces, graphene grows following this pathway.

Among all the possible catalysts listed above, the substrates currently more used for a potential large-scale production are copper and nickel, mainly due to their low price and the possibility to synthesize high-quality graphene.[31] Besides Cu

has been recently proposed as the best candidate for industrial exploitation of CVD graphene production,[6] Ni stood out for its high catalytic activity, that allows graphene growth at temperature as low as 450 °C.[7] This is a distinguished feature compared to CVD on copper surfaces, where temperatures of about 1000 °C are needed to completely dehydrogenate the gaseous C precursors.
From a more fundamental point of view, nickel is a good example of strongly interacting metal, that leads to important modifications of graphene properties,[37] as well as, in the case of (111) surface, a unique case of a lattice-matched system.[38] Indeed, since the lattice mismatch between the Ni(111) and graphene is less than 1%, graphene flakes are preferentially aligned with the substrate, resulting in a pure epitaxial growth. Nevertheless, recently also rotated graphene has been reported to grow on this surface,[9] suggesting a process driven by kinetics factors.[39] However, despite several efforts have been made in order to optimize the CVD procedure on Ni substrates,[40] the growth process and underlying atomistic mechanisms have yet to be fully understood. Moreover, the high C solubility of Ni adds further complexity, usually leading to graphene multilayer formation, which hinders large-scale samples uniformity.[41]

Part I

Experimental techniques

Chapter 3

Scanning Tunneling Microscopy

The invention of the scanning tunneling microscope (STM) by Binnig and Rohrer is considered a milestone in the field of nanotechnology, allowing scientists to see atoms on a surface for the first time.[42]
In this Chapter, the fundamental principles of STM operation will be discussed, in order to understand most of the experiments described in this thesis and to motivate the choice of this technique for the study of chemical processes occurring on metal surfaces. First, we discuss the operating principle of STM, explaining the physical origin of the atomic resolution capability. Then, the experimental setup used for this thesis is described.

3.1 Operating principle

The high resolution capability of STM is achieved by exploiting the tunneling effect, a quantum mechanical phenomenon, where a particle tunnels through a barrier that classically could not be surmounted.
When a metallic tip is approached to a conductive surface, a potential barrier forms between the two objects, due to the vacuum gap. If a bias voltage is applied between them, and their distance is small enough, so that their wavefunctions can overlap, an electrical current flows, due to the tunneling effect (see Figure 3.1). In Figure 3.2, a scheme of a basic STM set-up is depicted. Since the tunneling current depends on the electrode distance, changes of the sample corrugation down to picometers can be detected. When the tip is scanned over an area of the surface with sub-Å lateral resolution, images can be obtained in the following two modes:

- **Constant-height**:
  the tip is kept at a constant height while scanning, and the tunneling current I, which is recorded in every scan point, is color-coded to form a $I(x;y)$ image.

- **Constant-current**:

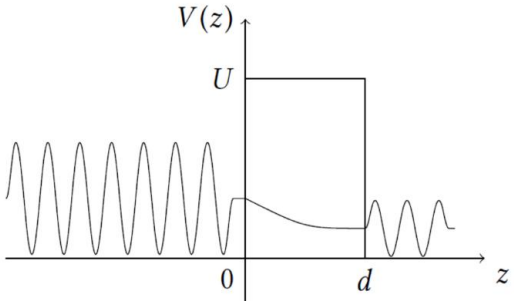

Figure 3.1: An electron impinging from the left on a one-dimensional potential barrier can cross the barrier even if E < U provided the width d is small enough.

during the scan, the tunneling current is kept constant by changing the tip height z by means of an electronic feedback system, and the STM image is formed by color-coding the tip height $z(x;y)$ in every scan point.

The former mode enables higher scanning speeds because no limitation is imposed by the response time of the feedback electronics, but has the critical drawback that the tip may accidentally crash on surface asperities. For this reason, STM measurements are usually performed in constant current mode.

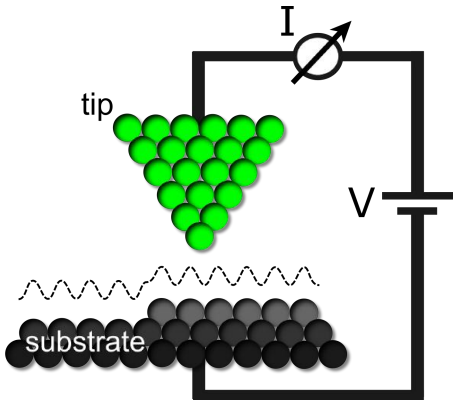

Figure 3.2: Schematic of a STM: a conductive tip is brought close to a conductive substrate. The tunneling current I is measured upon applying the bias voltage V. The dashed line represents the tip movement along a line scan, when the microscope operates in constant current mode.

3.1.1 Simple model of electron tunneling

If the potential barrier has a height U, and an electron represented by the wave function $\Psi(z)$ travels from the left with energy E (see Figure 3.1), the Schrödinger

equation of the system is:

$$-\frac{\hbar^2}{2m}\frac{d^2}{dz^2}\Psi(z) + V(z)\Psi(z) = E\Psi(z). \tag{3.1}$$

The general solution in the region $0 \leq z \leq d$ is given by:

$$\Psi(z) = Ae^{-kz} + Be^{kz},$$

where

$$k = \frac{1}{\hbar}\sqrt{2m(U-E)}. \tag{3.2}$$

The probability for an electron to tunnel between the two electrodes is given by the transmission coefficient of the junction:

$$T \propto e^{-2kd}. \tag{3.3}$$

As schematized in Figure 3.3, if a positive bias is applied to the sample with respect to the tip, the electrons will tunnel from the tip into the sample empty states, while for a negative bias they will tunnel from the occupied sample states to the tip. Applying this model to a metal-vacuum-metal junction, the potential

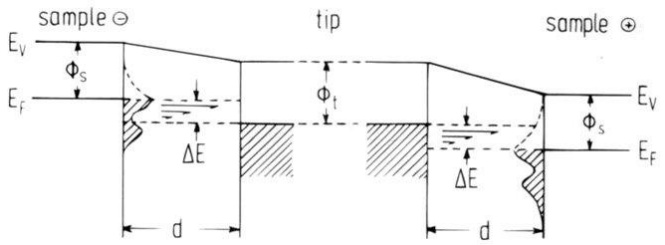

Figure 3.3: Tunneling from the tip to empty sample states (positive sample bias, on the right) and from occupied sample states to the tip (negative sample bias, on the left).

barrier can be approximated as the work function value ϕ of the electrode surface, that is the minimum energy required to extract an electron from a bound state to the vacuum level. Neglecting the thermal energy contribution:

$$E_F = -\phi. \tag{3.4}$$

For electronic levels close to E_F:

$$I \propto e^{-2\sqrt{2m\phi/\hbar^2}d}, \tag{3.5}$$

where d is the electrodes distance. If we consider a typical metal work function $\Phi \approx 4$ eV, we obtain the typical value of the decay constant of 1 Å^{-1}. This gives an estimate of the rate of change of the current with the distance: the current

increases by a factor 3 when the distance changes by one Bohr radius (Δd = 53 pm). This exponential dependence of the tunneling probability versus the tip-sample distance, as we will see below, is the physical property of the tip-sample system which enables picometer resolution in the direction orthogonal to the sample surface.

3.1.2 Bardeen model

In order to understand STM images, it is necessary to extend the one dimensional tunneling problem to the three dimensional case. To this purpose, we follow the formalism introduced by Bardeen.[43] In this approach, the tip and sample are treated separately and the overlap is calculated through the Fermi golden rule. The tunneling probability from a state Ψ, on one side of the barrier, to a state χ, on the other side, can be expressed as:

$$M = \frac{\hbar}{2m}\int_{z=z_0}\left(\chi^*\frac{\partial\Psi}{\partial z} - \Psi\frac{\partial\chi^*}{\partial z}\right)dS, \tag{3.6}$$

where $z = z_0$ is any separation surface lying entirely within the two electrodes. Then, the tunneling current can be expressed as:

$$I = \frac{4\pi e}{\hbar}\int_{-\infty}^{+\infty}[f(E_F - eV + \epsilon) - f(E_F + \epsilon)]\cdot\rho_S(E_F - eV + \epsilon)\rho_T(E_F + \epsilon)|M|^2 d\epsilon \tag{3.7}$$

and by assuming that $k_B T$ is small enough to approximate the Fermi distribution with a step function, equation 3.7 simplifies to:

$$I = -\frac{4\pi e}{\hbar}\int_{E_F}^{E_F+eV}\rho_S(E_F - eV + \epsilon)\rho_T(E_F + \epsilon)|M|^2 d\epsilon. \tag{3.8}$$

Eventually, if the M matrix is assumed to be almost constant within the energy range of interest, we obtain a final, simplified expression for the tunneling current:

$$I \propto \int_0^{eV} d\epsilon\,\rho_S(E_F - eV + \epsilon)\,\rho_T(E_F + \epsilon). \tag{3.9}$$

This equation clearly shows that the tunneling current, within Bardeen's extension of the one-dimensional tunneling problem, is a convolution of the DOS of two electrodes. However, assuming that the tip has only one s-like orbital in the apex atom (the so-called Tersoff-Hammann approximation),[44] the tunneling current can be approximated as:

$$I \propto \int_0^{eV} d\epsilon\,\rho_S(\vec{r_T},\epsilon), \tag{3.10}$$

where $\rho_S(\vec{r_T},\epsilon)$ is the local density of states of the sample at the tip apex position.

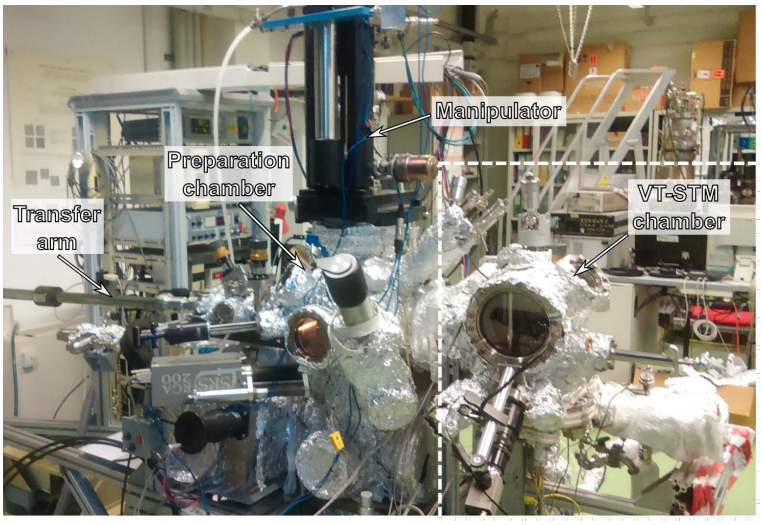

Figure 3.4: The experimental system.

3.2 Experimental setup

The UHV setup used for this thesis is located at CNR-IOM, Laboratorio TASC (Trieste) and is based on a commercial Omicron Variable Temperature Scanning Tunneling Microscope (VT-STM), modified in order to improve the mechanical stability and to work under reaction conditions (i.e. wide range of sample temperatures and during gas exposure). The system consists of one chamber for the sample preparation connected to another one where the STM is housed (see Figure 3.4). The background pressure, in the low 10^{-10} mbar range, is maintained by means of a magnetic levitation turbo molecular pump, an ion getter pump and a Ti-sublimation pump. Particular attention has been devoted to an efficient mechanical decoupling between the turbo molecular pump and chamber, in order to not affect the performance of the microscope.

3.2.1 Preparation chamber

The preparation chamber is equipped with a manipulator that allows cooling the sample down to 90 K, by filling the hollow tube of the manipulator with liquid nitrogen, and heating up to 1300 K, by means of a graphite heating element supported by a pyrolytic boron nitride (PBN) plate, hosted inside the sample holder. The manipulator head consists of a copper-aluminium alloy (GLIDCOP) block which is thermally coupled but electrically isolated from the manipulator axis by a sapphire plate. The manipulator head is provided with two sample stages that host the electrical connections for the temperature read-out (by means of K-type thermocouples) and the sample heating. One of them is thermally decoupled from the remaining part of the manipulator, allowing reaching high temperat-

ures (above 1000 K), while the other is characterized by a good contact between the back of the sample-holder and the manipulator head, offering the possibility to cool the sample (down to 90 K). A magnetic arm allows transferring the sample from the stage on the manipulator to a carousel hosted in the STM chamber. The preparation chamber is also equipped with:

- Sputter gun for sample cleaning by ion bombardment (Ar^+);
- Quadrupole mass spectrometer;
- Low Energy Electron Diffraction (LEED) system;
- Fast Entry Lock;
- Gas line (C_2H_4, H_2, O_2, CO and CO_2);
- Different types of molecule and metal evaporators;
- Hot filament ion gauge;

3.2.2 VT-STM

All the STM measurements presented in this thesis are conducted with a commercial Omicron Variable Temperature STM (VT-STM) system, capable of operating in a temperature range between 140 K, reached by filling a liquid nitrogen bath cryostat, and 900 K, reached by means of the PBN supported heating element inside the sample holder. The metallic tip is mounted on a magnetic stage

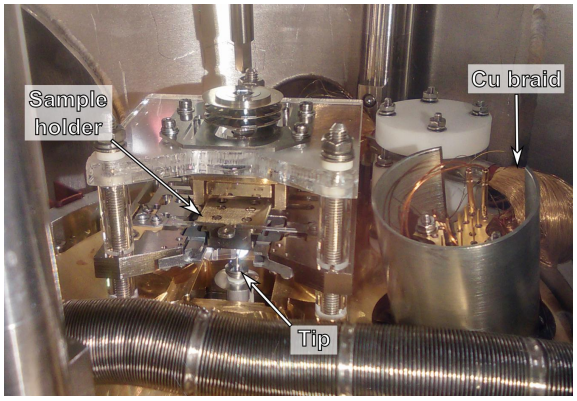

Figure 3.5: The Omicron VT-STM.

fixed on a single tube scanner with a maximum scan range of about 15×15 μm^2 and a z-travel of about 1 μm. A small radiation shield is fitted on top of the scanner, preventing heat radiation from the hot sample from slowly heating up the scanner tube, which would result in a long term drift. In Figure 3.5, it is possible to observe on the right the copper braid that connects the cryostat to a

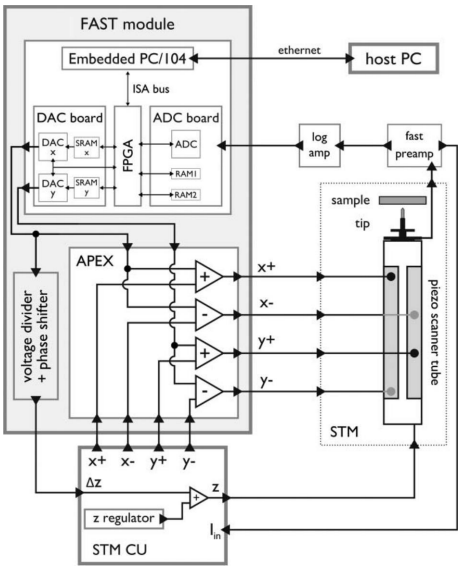

Figure 3.6: Schematic representation of the first complete setup, where the FAST module is inserted between the STM Control Unit and the scan system. For current detection, a fast preamplifier (fast preamp) and a subsequent logarithmic amplifier (log amp) are additionally inserted. The acquisition is controlled via Ethernet by the host PC. Reproduced from Esch et al. [45]

cooling block that can be placed in direct contact with the back of the sample holder (see Figure 3.5). In order to obtain a precise temperature read-out, the sample holder and the STM wiring have been modified to measure the temperature directly on the sample, by means of a K-type thermocouple directly spot-welded on the sample side. The sample is mounted in the STM sample stage with the surface pointing downwards and the tip is approached to the sample from the bottom. The coarse approach, up to some tens of microns, is monitored by a CCD-camera. The fine approach is then performed automatically. Mechanical isolation is achieved by means of a spring system, which suspends a heavy base platform of the STM. The base platform suspension is damped by an eddy current system: the platform is surrounded by copper plates, which are centered between permanent magnets, fixed on the chamber. The original current preamplifier has been replaced by a FEMTO DLPCA-200, in order to increase the cut-off frequency (from 50 kHz to 220 kHz, with a transimpedence of 10^8 V/A).

3.2.3 FAST module

Since the typical image acquisition times of commercial STM are of the order of seconds or even more, the time resolution is one of the biggest limitations. This usually hinders access to most steps of non-equilibrium processes, involved for

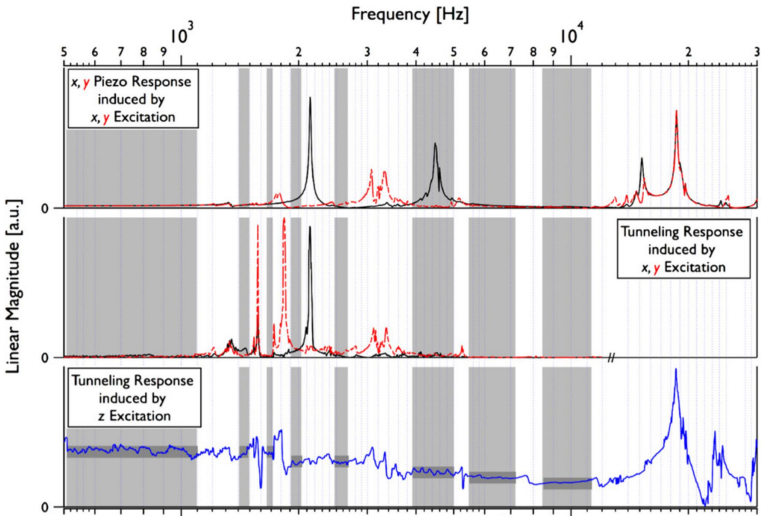

Figure 3.7: Resonance behavior of the VT-STM scanning stage in various measurement setups: under *out of tunneling* conditions upon lateral excitation (top panel), under tunneling conditions upon lateral excitation (middle panel) and under tunneling conditions upon vertical z excitation (bottom panel). In the first case, the voltage modulation induced in the piezo quadrant opposite the excited one has been measured, while in the two latter cases the tunneling current was recorded as a function of the x, y and z excitation, respectively. Excitation in the x and y directions corresponds to solid and dashed curves, respectively. The frequency windows where high, stable and reproducible resolution can be achieved, are indicated as gray areas. The horizontal dark gray bars in the bottom panel indicate the plateau regions. Reproduced from Dri et al. [50]

instance in chemical reactions, thin-film growth and molecular self-assembly with an adequate temporal resolution. In order to bridge this gap, several efforts have been made in the last 20 years, especially through the design of systems with high frequency resonances of the scanner tube, above the desired scan speeds, to avoid any interference between the probe motion and the mechanical response of the system. [46–49] However, the possibility to drive commercial systems in the fast operating mode is intriguing, allowing in this way the upgrade of existing expensive instruments, working in different environments (air, liquid, electrochemical, high pressure, variable temperature, etc...). [45]
A custom-made add-on module with this unique capability has been developed in our laboratory (see Figure 3.6). [45] Through a careful analysis of the mechanical behavior of the piezo scanner tube (see Figure 3.7), it has been possible to identify frequency windows, even above the first resonance frequency of the scanning stage, where atomic resolution can be achieved even for frame rates up to 100 Hz. [50] For this purpose, a pure sine wave is used as the fast excitation signal, as firstly reported by Wintterlin et al. [49] Since the tip speed is therefore

non-uniform, in order to correct for this effect the images must be suitably resampled during the post-processing. Time-series consist in forward or backward sequences of images acquired during the up and down movement of the slow excitation wave. During the acquisition, the microscope operates in quasi-constant height mode. Indeed, a proper tip height correction feedback circuit, besides requiring a very high bandwidth circuit (in the MHz range), would excite further mechanical resonances in the piezo, undermining the stability of the system. In order to take into account the sample tilt in the fast direction, which commonly exceeds the actual surface corrugation of interest, it is necessary to correct this tilt to access the full dynamic range of the preamplifier ($I_{max}/I_{min} \simeq 10^4$, corresponding to about 4-5 Å). For this purpose an active correction is applied to the vertical movement piezo.[45]
During my PhD, a second version of the FAST module has been developed, in collaboration with the Instrumentation and Detector Lab (Elettra Sincrotrone Trieste). In this way, we improved the imaging performances, introducing also a fully automatized tilt correction system and the possibility to acquire other experimental data, such as sample temperature and imaging parameters. For this upgrade both the hardware and software have been changed. The hardware upgrade mainly consists in a Full Programmable Gate Array (FPGA) driving two 16-bit Digital-to-Analog converter (DAC) with 100 Msample/s for the fast tip movement and an 14-bit Analog-to-Digital converter (DAC) with 100 Msample/s for the current measurements. For the generation of the signals of the slow movements, a 16-bit DAC with 833 ksample/s has been used. The imaging parameters (bias voltage and feedback current) and the sample temperature are measured by means of a 16-bit DAC and saved as file metadata. All the parts used are commercial (National Instruments). In addition, the current log-amp has been replaced by a high-pass filter ($\nu_{cut} = 50Hz$). Indeed, with this configuration it is possible to maximize the usage of the ADC dynamics for the AC current components measurements, that represent the useful signal. The new software driving the FPGA is based on LabVIEW. The files are saved as raw data in $hdf5$ format and post-processed by a Python code.
In this way, atom-resolved movies with a frame rate up to 100 Hz and 100×100 pixels can be routinely acquired, as shown in Figure 3.8.

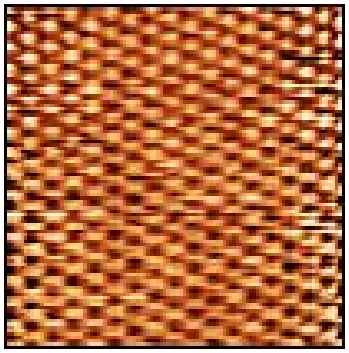

Figure 3.8: Atomically resolved imaging above video-rate: raw image acquired with the FAST unit on epitaxial graphene/Ni(111) [100 Hz, 4×4 nm^2].

Chapter 4

Photoemission Spectroscopy

The photoemission spectroscopy is an experimental technique that consists in the analysis of the kinetic energy distribution of electrons extracted from a material through the photoelectric effect.
During this thesis, PES has been used to investigate the electronic properties of CVD graphene, providing informations on the sample composition, on the band structure and on the state of chemical bonds, being an helpful complement to the STM measurements.
In this Chapter, the basic concepts of the experimental techniques are briefly reported. The presentation is limited to the fundamentals that are directly useful to the understanding of the experimental data discussed. A more detailed and complete discussion can be found, for example, in the proceedings of the International Conferences on the Structure of Surfaces.[51]

4.1 Operating principle

When an incident photon beam interacts with a material, to a first approximation, electrons at binding energy lower than photon energy can be ejected from the surface. Within a single particle picture, the kinetic energy distribution of the emitted electrons mimics the distribution in energy of the occupied electron states in the ground state.[52] In this case, the kinetic energy E_k of the photoelectron coming out from the sample is approximately given from the following relation:

$$E_k = h\nu - E_b - \phi_s, \tag{4.1}$$

where E_b is the binding energy of the photoelectron relative to the Fermi level, $h\nu$ the used photon energy and ϕ_s is the work function of the sample.[53] In order to be detected, the photoelectrons must overcome the potential barrier $\phi = \phi_A - \phi_s$, where ϕ_A is the work function of the electron analyzer. As a consequence, equation 4.1 becomes:

$$E_k = h\nu - E_b - \phi_A, \tag{4.2}$$

which is independent from the sample work function. Even if the photons penetrate into a solid for several μm, photoemission is a surface sensitive technique. In fact, the sampling depth in the photoemission process is determined by the mean free path of the photoelectrons in the solid. This quantity follows the so-called universal curve of the energy-dependent inelastic mean free path of electrons in solids, and it changes as a function of the electron kinetic energy from about 4 Å to about 50 Å (see Figure 4.1).[54] In a one-particle framework, given

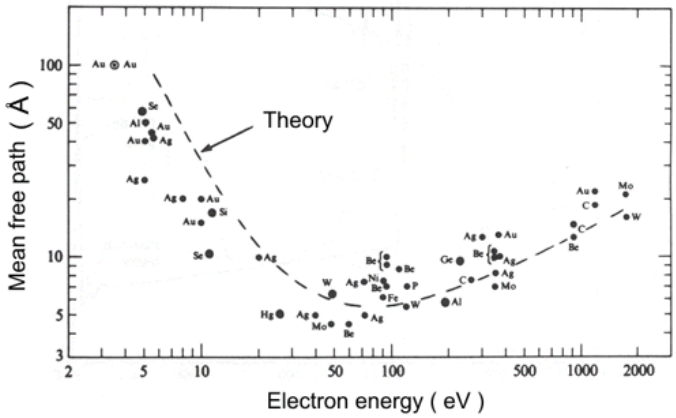

Figure 4.1: Inelastic mean free path of electrons in solids.

an impinging flux of photons, the current density of photoelectrons can be expressed in terms of Fermi's Golden Rule formula, where the matrix element, in the dipole approximation, can be written as:

$$M_{fi} = < \Psi_f | \mathbf{A}\,\mathbf{p} + \mathbf{p}\,\mathbf{A} | \Psi_i > \tag{4.3}$$

where Ψ_f and Ψ_i are, respectively, the final and initial state electron wave functions, **A** is the electromagnetic vector potential and **p** is the electron momentum. To a first approximation, a photoemission spectrum provides the distribution of the binding energies of the electron states in a solid. The intensities of the photoemission structures reflect the density of states and depend furthermore on the cross sections of the photoemission processes involving electrons of different energy levels.

4.2 X-ray photoemission spectroscopy

The excitation of most core levels requires at least soft X-rays, which explains the more usual acronym of the technique, X-ray photoemission spectroscopy (XPS). A measured XP spectrum is shown in Figure 4.2, which is characterized by sharp peaks, usually called primary structures. These structures are superimposed to a mostly featureless background, which exhibits a huge peak (not shown) in the

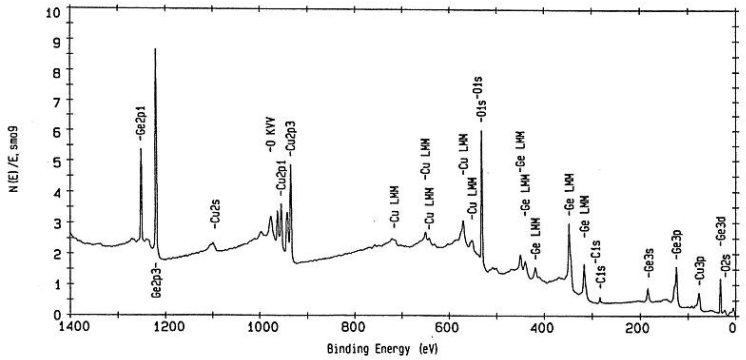

Figure 4.2: Photoemission spectrum from a $CuGeO_3$ single crystal ($h\nu$=1253.6 eV). Core levels and Auger peaks are indicated.

low kinetic energy region ($\simeq$ 5-10 eV). This background is ascribed to the almost continuum distribution of the secondary electrons which are produced after inelastic scattering within the solid, thus having lost memory of their primary energy. The most intense and sharp peaks correspond to the emitted electrons from the core levels of the atoms of the solid. Because of the discreteness of the core levels energies, each core level distribution is a fingerprint of a specific chemical element, thereby making photoemission spectroscopy an atom-specific technique. Handbooks collecting XPS spectra for each solid element are currently available, and used as reference data base for core level identification.[55] A very important point is related to the so-called core level shift. Actually, a core level binding energy depends on the chemical bonds and local environment of a specific atomic site. Thereby the identification of the chemical state of an atom in an unknown solid system is made possible, consistently with the energy resolution and the actual size of the core level shift. The broad structure at the higher kinetic energies of the photoemission spectrum corresponds to the energy distribution of the valence band states. The typical feature of these shallow states is their delocalized character, compared to the local nature of core levels. They are thus expected to markedly change their distribution in energy as the chemical bonds are changed. In the photoemission spectra also other structures are visible, typically Auger peaks, shake up losses and correlation satellites due to relaxation processes, i.e. excitation and de-excitation of the system after the creation of the hole.
The width of a photoemission core level depends on many different factors, schematically indicated in Figure 4.3. Even if some of these contributions may be not trivially connected, they can be schematically listed in the following points:

1. **Mean lifetime of the photo-hole**: every core level in the photoemission spectrum has an intrinsic width, which is determined by the mean lifetime of the hole created in the photoemission process. The hole de-excitation

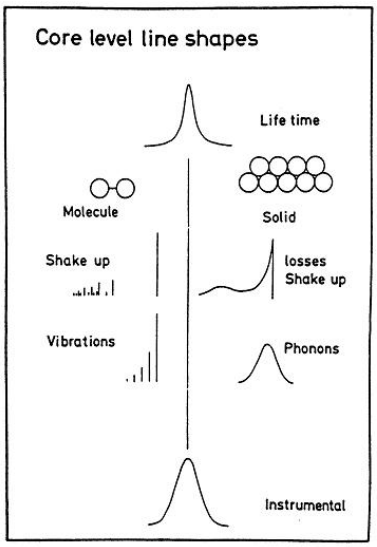

Figure 4.3: Scheme of the different contributions of the photoemission lineshape in a isolated molecule and a solid.

goes through radiative or Auger processes in typical times of the order of 10^{-14}-10^{-15} s, and gives a contribution to the photoemission peak width with a Lorentzian line-shape.

2. **Electronic excitations**: the hole creation modifies all the electronic states of the system. This perturbation creates excited electronic states in the $N-1$ electrons system. In molecules or insulating systems this leads to satellite peaks usually well separated from the core level, while in metallic systems, where infinitesimal excitations are possible across the Fermi level, this leads to the presence of the characteristic asymmetric lineshape of the photoemission peak towards lower kinetic energies.[56]

3. **Phonon coupling**: the extraction of an electron from a solid generally brings with it the excitation of the vibrational modes of the system. This is due to the fact that the curves of potential energy of the N electrons system, as a function of the nuclear distance, may change after the ionization.

4. **Instrumental broadening**: this is generally the most dominant broadening in a photoemission spectrum and it is due to the finite instrumental resolution of the electron energy analyzer and to the non-monochromatic character of the light source. These contributions give a Gaussian broadening to the photoemission peaks.

4.3 Angle Resolved Photo-Electron Spectroscopy

The electronic valence band dispersion can be mapped by means of PES, using low photon energy (4-90 eV) and measuring the photo-electron kinetic energy distribution as a function of the emission angle (Angle Resolved Photo-Electron - ARPES). In this way, it is possible to obtain information on the direction, speed and scattering process of valence electrons in the sample being studied. Due to presence of the surface, only the parallel component of electron momentum is conserved:

$$\hbar k_{i\parallel} = \hbar k_{f\parallel} = \sqrt{2mE_k}\sin\theta \tag{4.4}$$

An ARPES spectrum is recorded collecting the outgoing electrons within a finite energy resolution and acceptance angle and binning the electrons according to their momentum and kinetic energy. A typical ARPES spectrum is shown in Figure 4.4, revealing dispersion of the Shockley state (SS) in a Ni(111) surface.

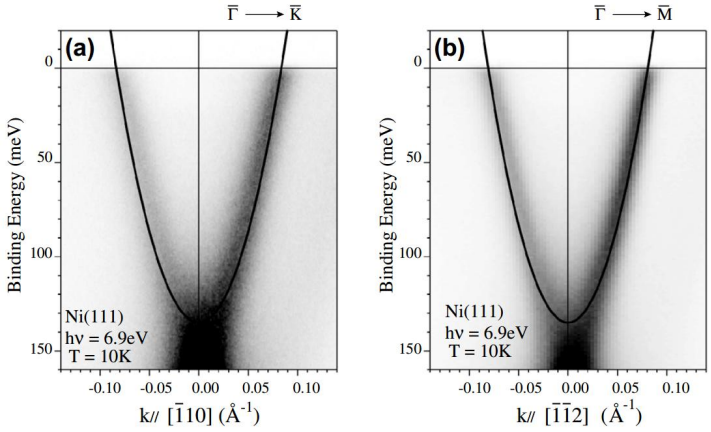

Figure 4.4: ARPES results of Ni(111) surface state along the (a) Γ-K and (b) Γ-M directions. Reproduced from Higashiguchi et al. [57]

Chapter 5

Cathode Lens Electron Spectro-Microscopy

In order to obtain complementary information to the ones provided by STM, experiments have been performed using the Spectroscopic Photo-Emission and Low Energy Electron Microscope (SPELEEM) operating at the Nanospectroscopy beamline of the Elettra synchrotron in Trieste. The SPELEEM combines Low Energy Electron Microscopy (LEEM), with Photo-Emission Electron Microscopy (PEEM), being able to probe the crystal structure and stoichiometry of surfaces on the micro-scale, with lateral resolution of few tens of nanometers. First, the imaging, diffraction and spectroscopic methods of cathode lens microscopy are discussed. Then, the SPELEEM setup is presented, describing the different operating modes.

5.1 Low Energy Electron Microscopy

Low energy electron microscopy (LEEM) is a surface-sensitive method based on the backscattering of elastic electrons that interact with a surface. [58,59] The high electron backscattering cross section in the energy range from 2 to 20 eV warrants an intense electron yield, enabling acquisition with high image intensity. The energy dependence of the backscattering intensity on the electron energy is not trivial due to high multiple scattering cross section of electron at such energies. Nevertheless, the backscattered intensity strongly depends on the structural an chemical properties, giving LEEM the sensitivity to probe surface morphology.
Figure 5.1 shows a schematic view of the of the LEEM instrumental concept design. [60] The electrons produced by an e-gun are accelerated to an energy of several keV, by a bias V_0. Subsequently deflected by the separator, the e-beam is forced to approach the sample in normal incidence. When traveling through the objective lens, the e-beam is decelerated by the same voltage potential V_0 used at the electron source. However, a bias voltage (known as start voltage, V_{start}) is

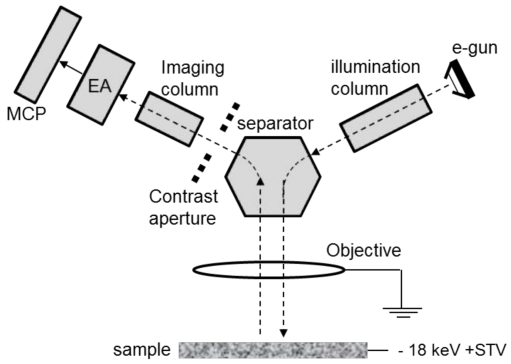

Figure 5.1: Scheme of the LEEM microscope at the Nanospectroscopy beamline.

applied to the sample in order to set the desired electron energy. Back-scattered electrons are accelerated by V_0 through the objective that produces a magnified image of the sample. The image is further magnified by the lenses in the imaging column. The final image is projected onto image detector with micro-channel plate and a phosphorous screen. The fluorescence light is collected by a CCD camera which acquires the image.

Imaging modes When the low energy electrons are scattered from the sample surface, they produce a diffraction pattern, depending on the beam that is selected, two different methods can be employed:[61]

- **Bright-field imaging**
  Using the specular (0,0) beam, the contrast is purely structural and depends on the local differences in diffraction for the different surface phases present on the sample.

- **Dark-field imaging**
  By selecting a secondary diffracted beam, a dark field image of the surface is produced. In this way, all areas that contribute to the formation of the selected beam appear bright.

5.2 Low Energy Electron Diffraction

Low Energy Electron Diffraction (LEED) is a commonly used technique that allows determining the crystal structure of surfaces or thin films.[62] A simple inspection of a LEED pattern provides a powerful tool to study the surface lattice symmetry, the lattice constants and the presence of contaminants. To understand the principle of LEED, a kinematic theory of scattering must be taken into account. According to Bragg elastic scattering theory, the diffraction spot occurs

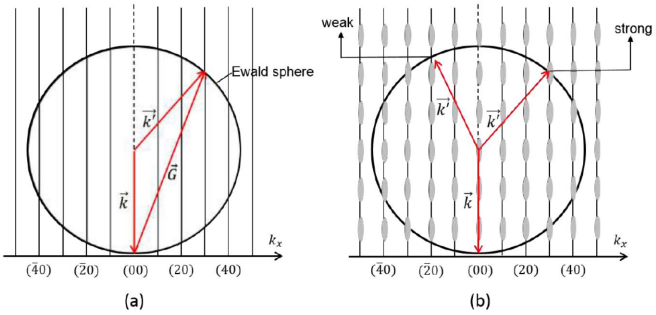

Figure 5.2: Ewald construction for elastic scattering on a 2D surface lattice for an ideal (a) and realistic (b) surface. $\vec{k}$ and $\vec{k}'$ are the incident wave vector and scattered wave vector, respectively. $\vec{G}$ is the reciprocal space vector, defined in equation5.1. The corresponding 2D reciprocal lattice point are displayed on a cut along k_x.

if the following condition is fulfilled:

$$K_{\parallel} = k'_{\parallel} - k_{\parallel} = G_{\parallel} \tag{5.1}$$

where $K_{\parallel}$ is the difference between parallel component to the surface of incident scattering vector ($k_{\parallel}$) and scattered vector ($k'_{\parallel}$). $G_{\parallel}$ is the parallel component to the surface of reciprocal vector $\vec{G}$. Figure 5.2 shows a geometrical explanation of LEED principle. The Ewald sphere is the sphere having a radius equal to $|k| = |k'|$. Equation 5.1 is fulfilled for every point at which the sphere crosses a reciprocal lattice rod. For 2D systems, we can relax the restriction on $k_{\perp}$ (third Laue law); as consequence diffraction condition is satisfied more frequently respect to 3D systems. For a real surface, bulk contribution can not be neglected since primary electrons penetrate more than the first atomic layer. The resulting LEED pattern is therefore modulated. A realistic model that takes into account both surface and bulk contribution is shown in Figure 5.2b. If a diffracted vector $\vec{k}'$ crosses a reciprocal lattice rod, the corresponding spot intensity will be weak, whereas if $\vec{k}'$ crosses a *thicker* region of the rods the spot intensity will be strong.

5.3 Photo-Emission Electron Microscopy

Photo-emission electron microscopy (PEEM) images a sample that is illuminated by UV or X-ray photon beam,[63,64] exploiting the photoelectric effect (see Chapter 4). The emitted electrons are accelerated by an intense electric field (tens of keV/mm) that is applied between the sample (cathode) and the objective (anode). The objective lens produces a magnified image of the specimen, which may be further magnified by other lenses along the imaging column. The magnified image is projected onto a detector consisting of the MCP, the phos-

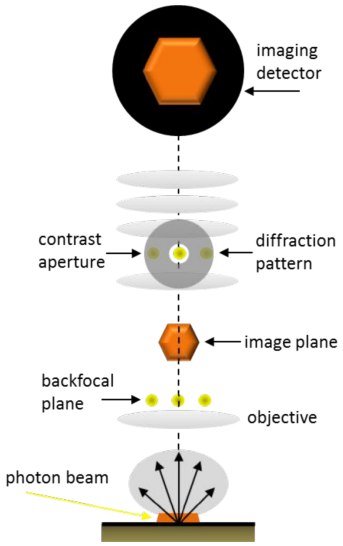

Figure 5.3: PEEM simplified configuration.

phorous screen and the CCD camera. The angular acceptance of emitted electrons is reduced by an aperture (contrast aperture) in the back focal plane of the objective. Figure 5.3 shows a simplified sketch of the PEEM configuration. In the example, the sample is at a negative potential with respect to the objective and imaging column, kept at ground. The PEEM detects photo-electrons emitted from a surface and produces an image in the real space. Using an energy filter, only the electrons emitted with a particular kinetic energy are collected to form the image.

5.4 SPELEEM operating modes

The SPELEEM combines LEEM and PEEM methods. The electron beam is produced by the LaB6 electron gun and is subsequently collimated by three condensor lenses. The separator deflects the beam towards the objective lens, of which the sample is part. Interaction with the specimen occurs in normal incidence. Spot size on the sample is about 80 μm in diameter. Three apertures inserted in the beam separator allow the illuminated area to be reduced to a diameter of 5, 1 and 0.5 μm. In the SPELEEM, the electron energy can be regulated by applying a bias voltage to the sample (-5, +700 eV). The choice of the bias voltage defines the start energy of the electrons that reach the detector. After interaction with the surface, backscattered electrons are accelerated towards the objective. The beam separator bends the beam towards the imaging column, where a set of optical elements is used to set the operation mode and change the magnification. The magnified image of the specimen is eventually projected on a micro-channel plate coupled with a phosphorous screen. A very sensitive

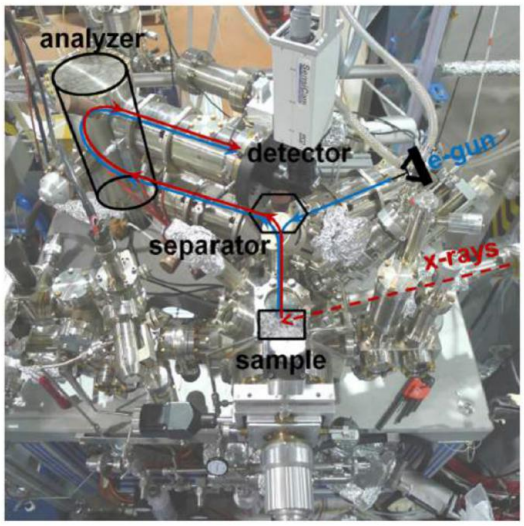

Figure 5.4: The SPELEEM instrument at the Nanospectroscopy beamline at Elettra facility. The scheme of the basic set-up is superimposed onto the photograph. Reproduced from Menteş et al. [61]

CCD camera (PCO Sensicam QE) enables image acquisition with video-rate exposure.
Using the photon beam as probe, the microscope enables implementing laterally resolved versions of the two principal synchrotron-based spectroscopies, X-ray absorption spectroscopy (XAS) and X-ray photoemission spectroscopy (XPS). While in the former secondary electrons are used for image formation, in the latter photoelectrons emitted from core levels or the valence band are detected. The photon beam impinges on the specimen at grazing incidence, at an angle of 16 degrees with respect to the surface. The minimum spot size on the surface is 20 μm x 3 μm (horiz. x vert.). The electron beam is magnified by the objective lens and by the combined action of field and intermediate lenses in the imaging column. The magnified image is filtered in energy by the energy analyzer which consists of combined retarding and and imaging lens system, a hemispherical analyzer and a combined accelerating and imaging lens system. Finally, two lenses project the image onto the detector.
A photograph of SPELEEM at the Nanospectroscopy beamline is shown in Figure 5.4, colored lines indicate the optical path of electrons (blue) and of photons (red). The most important electron-optical elements and essential components are indicated. Figure 5.5 shows the three different SPELEEM electro-optical configurations,[61] summarized as follow:

- **Imaging mode**: the electron optics produces a real-space, magnified image of the specimen. Lateral resolution is ~9 nm in LEEM and ~25 nm in XPEEM.

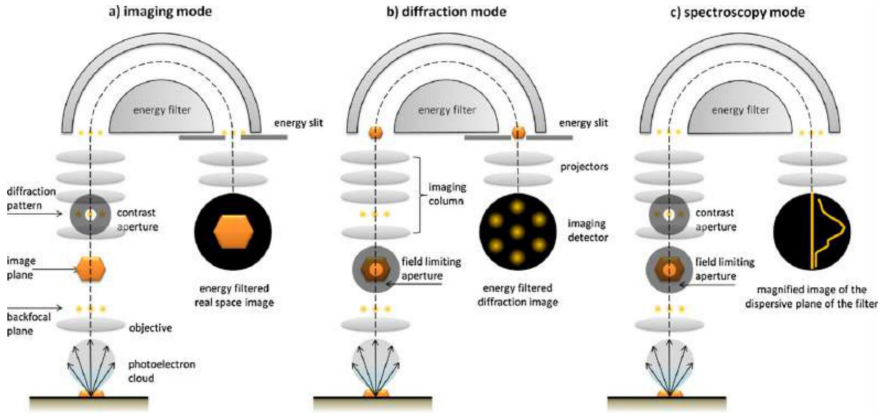

Figure 5.5: Electron-optic configuration of the SPELEEM instrument in the three different operating modes.

- **Diffraction mode**: the electron optics is configured to produce a magnified image of the objective back-focal plane, that is a magnified image of the diffraction figure found in the objective back-focal plane. Depending whether photons or electrons are used as probe, μ-LEED or μ-ARPES measurements are possible.

- **Microprobe-spectroscopy**: the dispersive plane of the analyzer is imaged. In this way, acquisition of spectra is fast and the instrument reaches its best energy resolution.

Part II

CVD Graphene on Ni(111)

Chapter 6

Adsorption structures

This Chapter presents a study of graphene adsorption geometries on Ni(111), synthesized by CVD under UHV conditions. In the first part, we provide a detailed description of geometric structures of epitaxial graphene (EG) at the atomic scale by means of joint experimental and theoretical approach, clarifying an open point in the current literature. Then, we investigate the rotated graphene (RG) structures, also showing how a different graphene-substrate interaction can be exploited in order to interpose a Nickel carbide layer between graphene and the metal. Most of the results presented here have been published in the *Journal of Physical Chemistry Letters*,[65] and in *Scientific reports*.[66]

6.1 State of the art

Since the early stages of surface science, graphitic overlayers on Ni surfaces were reported.[67,68] In particular, the atomic structure of EG on Ni(111) has been thoroughly investigated and several possible configurations proposed. Pioneering experiments by Rosei et al.[38] suggested a hcp-fcc configuration (i.e. with the C atoms of the unit cell on hcp and fcc sites), later ruled out by LEED-IV experiments,[69] which first proposed top-fcc and top-hcp arrangements (i.e. with the two C atoms of the unit cell in top and fcc, and in top and hcp positions respectively). These and other alternative structures were proposed as the most stable ones in many experimental and theoretical investigations, without reaching a general consensus. In particular, top-fcc, top-hcp and hcp-fcc structures have all been proposed in a work based on density functional theory (DFT), neglecting dispersion forces and using generalized gradient approximation (GGA) for the exchange correlation functional.[70] In this context, Fuentes-Cabrera et al.[71] found that the top-bridge as the most stable configuration using the local density approximation (LDA) and, showing that there are significant discrepancies between GGA and LDA results, pointed out the need to include van der Waals interactions.[71] Recently, DFT-GGA calculations with semi-empirical corrections for dispersive interactions established that graphene chemisorbs on Ni(111) only

in two possible stable configurations (top-bridge and top-fcc), while in other high-symmetry arrangements (including top-hcp) does not have a stable chemisorbed minimum or can only physisorb.[72,73] Despite of this, all the high symmetry structures studied by Kozlov et al.[73] display very similar adsorption energies, and therefore could co-exist on the surface. Indeed, scanning tunneling microscopy (STM) images by Lahiri et al.[74] demonstrated the co-existence of top-fcc and top-hcp graphene, evidenced by the formation of an extended defect at the boundary. More recently, DFT-GGA calculations using a slightly different dispersive force correction term, confirmed top-fcc as the energetically most favourable geometry, followed by top-bridge, top-hcp and hcp-fcc.[75] Recently, the formation of graphene domains misoriented respect to the underlying Ni(111) substrate has been reported, tentatively ascribing this effect to a growth process occuring on top of Ni_2C islands.[9] However, *in situ* LEEM studies later revealed the growth of rotated graphene (RG) to happen directly on clean Ni, at temperatures above 650 °C.[39]

6.2 Results and discussion

6.2.1 Epitaxial graphene

The Ni(111) sample has been cleaned by standard Ar^+ sputtering (2 keV) and flash annealing (600 °C) cycles. EG was prepared by exposure of the clean Ni surface to ethylene (p = 2×10^{-7} mbar) at temperatures in the 400-500 °C range. The epitaxial matching is evident from the LEED pattern in Figure 6.1, where

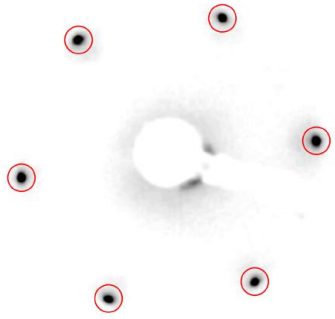

Figure 6.1: LEED pattern of the epitaxial graphene phase on Ni(111) (E = 70 eV). Red circles indicate the (1 × 1) spots of the substrate.

only a (1×1) structure is visible. *In situ* high-resolution STM images of graphene on Ni(111) show a significant contrast variation in distinct areas of the same region, unambiguously indicating the co-existence of different configurations, as shown in Figure 6.2. The STM contrast of graphene overlayers on Ni(111) was already discussed in previous DFT papers,[72,74,76,77] but presenting only a limited comparison with experiments, not sufficient for a safe interpretation of our im-

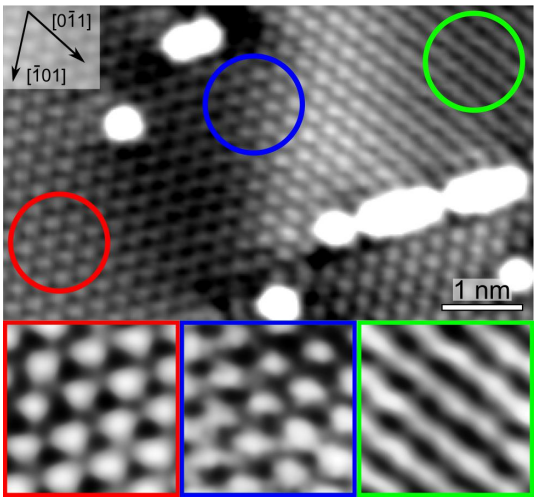

Figure 6.2: Epitaxial graphene on Ni(111). (Top) atomically resolved STM image showing the coexistence of different contrasts. (Bottom) Zoom on the regions highlighted with circles in the top image [V = 3 mV, I = 0.7 nA].

ages. Furthermore, in literature experiments graphene/Ni(111) usually appears as a homogeneous triangular array of bright protrusions, while in our images it is possible to distinguish additional features, related to the different adsorption geometries. To obtain specific fingerprints of graphene configurations, we thus investigate in more details by DFT the energetics and the STM images of some selected arrangements. DFT calculations have been performed focusing on the top-fcc, top-hcp and top-bridge adsorption configurations,[65] yielding the lowest chemisorption energies according to the values reported in literature.[72,73,75] The stick-and-ball models of the optimized structures are shown in Figure 6.3a-b. Our calculations clearly establish that using DFT-GGA with dispersion forces corrections, stable chemisorbed structures are obtained in all three cases, with a graphene-metal surface distance of about 2.1 Å and a small reduction of the interplanar distance between the two outermost Ni planes. The chemisorption energy per C atom is -0.16, -0.14 and -0.15 eV in top-fcc, top-hcp and top-bridge configurations respectively, basically equivalent within our numerical accuracy of ~ 0.02 eV. Notably, the three configurations are not stable for DFT-GGA without dispersion interaction corrections. Our findings are consistent with the available experimental data[69,72] and, extending the conclusions drawn by Mittendorfer et al.,[78] reconcile most of other previous theoretical results based on different techniques.[70–74,77,79] Figure 6.3c shows the simulated constant current STM images of filled states close to the Fermi level, at small tip-sample distances; specifically, we mapped an ILDOS iso-surface lying ~2-3 Å above graphene. The top-fcc structure exhibits two triangular arrays of bright (above fcc C atoms) and grey (above top C atoms) spots.[72,76,77] The appearance of the STM image for top-hcp structure, which to our knowledge was never simulated be-

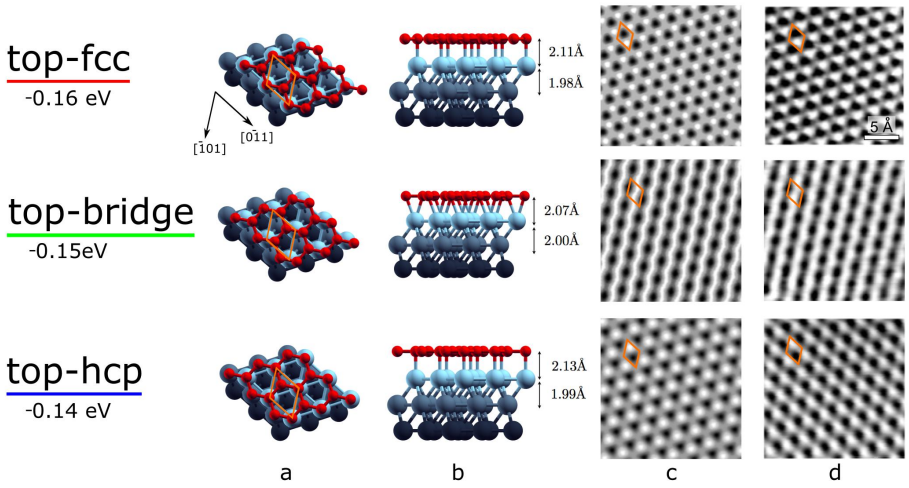

Figure 6.3: Different epitaxial graphene/Ni(111) configurations. Stick-and-ball models: (a) top-view and (b) side-view. Corresponding STM simulated (c) and experimental (d) STM images. Adsorption energies are indicated in brackets below the name of each configuration. Scanning parameters: top-fcc [V = -300 mV, I = 2 nA], top-bridge [V = -10 mV, I = 25 nA], and top-hcp [V = -100 mV, I = 20 nA].

fore, is very similar: bright spots corresponding to hcp C atoms form a triangular arrangement, with grey features above on-top sites. The top-bridge geometry, conversely, gives a completely different simulated image: zig-zag bright stripes along a Ni close-packed crystallographic direction alternate to lines of *holes* almost centered on hcp Ni sites. The three different contrasts obtained in

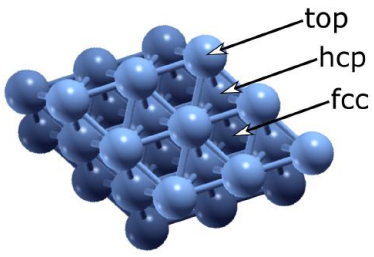

Figure 6.4: Ball-and-stick model of the Ni(111) surface, oriented as the sample used in the experiments. Arrows indicate top, hcp and fcc sites.

simulated STM images nicely correspond to those highlighted in Figure 6.2, typically characterizing our experimental images. It is important to note that all the experimental images shown are oriented along the same crystallographic direction, as determined by the sample mounting. In such configuration, the relative position of the second layer of Ni atoms has been determined (see Figure 6.4), by means of an atomically resolved image acquired across a single Ni step edge

(not shown). In Figure 6.3d, experimental high-resolution images acquired at high tunneling current and close to the Fermi level are reported next to simulations. It is clear that:

1. a triangular array of protrusions, with grey features in the center of each triangle pointing towards the top of the image is associated to top-fcc graphene domains;

2. a triangular array of protrusions with grey shadows in the center of each triangle pointing towards the bottom of the image represents top-hcp regions;

3. zig-zag stripes oriented along one of the close-packed directions of the underlying substrate correspond to top-bridge areas.

We highlight that discrimination between top-fcc and top-hcp depends on our capability to image top C atoms appearing as grey features, as predicted by DFT, and on the identification of the crystallographic orientation of the substrate. By joining adjacent on top C atoms we can mark the same unit cell for both structures, thus identifying the position of the second C atom within it. Notably, the top C atoms, and therefore the differences between the two configurations, are visible in our images only for scanning parameters corresponding to a short tip-sample distance, estimated in ~ 2 Å for typical scanning values of I = 30 nA and V = 10 mV.[80] For larger distances, only the usual triangular array, or faint stripes are observed, as expected by analyzing the calculated ILDOS iso-surfaces.
Our results, demonstrate the possibility of identifying the actual graphene geometry by its STM contrast, thus allowing for a statistical analysis of the surface distribution of its different configurations. By examining about 60 high-resolution images we found the top-fcc as the statistically most abundant configuration ($\sim 65\%$), in agreement with the results of the LEED I-V study on epitaxial graphene grown by ethylene CVD in UHV,[69] even though in that case a higher growth T was used. A minor contribution is given by top-bridge ($\sim 22\%$) and top-hcp ($\sim 13\%$) configurations. Nicely, the relative order of the calculated adsorption energies follows the one of the observed coverage: stronger adsorption corresponds to larger coverage. However, the three configurations are practically equivalent from DFT predictions and reasonably also factors other than thermodynamics, such as growth kinetics from graphene nuclei with different configurations, influence the observed coverage balance.

6.2.2 Rotated graphene

A sample consisting mainly of RG has been prepared by exposure of a clean Ni(111) surface to ethylene ($p = 2 \times 10^{-7}$ mbar) at 600 °C for 2 h. As shown in Figure 6.5, the LEED pattern presents small arches, centered around $\pm 17°$, in addition to the substrate spots, indicating the coexistence of different rotation angles.[9,39] The presence of only a limited number angles can be explained by

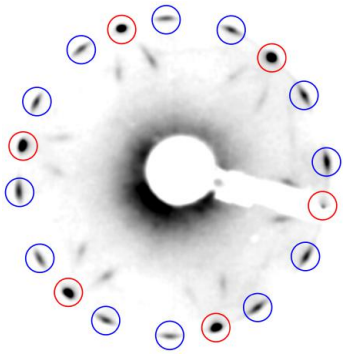

Figure 6.5: LEED pattern of rotated graphene on Ni(111) (E = 70 eV). Red and blue circles indicate the spots of the substrate and of the graphene domains respectively.

means of lattice coincidence and commensurability arguments,[81] as well as kinetics factors.[82]
The misorientation between the graphene layers and the Ni surface gives rise to specific moiré superlattices. From a geometrical point of view, the superlattices periodicity is defined as:

$$D = \frac{d}{2 \cdot \sin(\theta/2)}, \tag{6.1}$$

where d is the lattice parameter 0.249 nm, assumed to be the same for graphene and Ni(111), and θ the misorentation angle.
Experimentally, a LEED analysis can directly probe the angular distribution (i.e. θ) of the rotated flakes, while STM measurements can get access safely only to D, since thermal drift and creep effects hinder an absolute θ assignment. In order to compare the information coming from this two techniques, in Figure 6.6 we showed representative STM images of RG and a quantitative analysis of the angular distribution, obtained from μ-LEED patterns of 69 domains with lateral dimensions larger than 500 nm. Then, by using equation 6.1 (see blue line in Figure 6.6d), it is possible to unambiguously relate the complementary results. The STM images in Figure 6.6a-c present periodicities of 1.2, 1 and 0.85 nm, corresponding to θ values of 12, 14 and 17°respectively. This matches well with μ-LEED analysis, that show a broad peak centered around 17°, and a minor component at about 12°.

6.2.3 Rotated graphene on Ni carbide

Upon cooling a RG layer to RT, a different STM contrast appears in some regions of the surface (see Figure 6.7a). This peculiar STM appearance was previously observed and attributed to the presence of Ni_2C islands underneath a rotated graphene flake (RGC).[9] Indeed, the Fast Fourier Transform (FFT) pattern of the STM image (see Figure 6.7b) exhibits square-like features character-

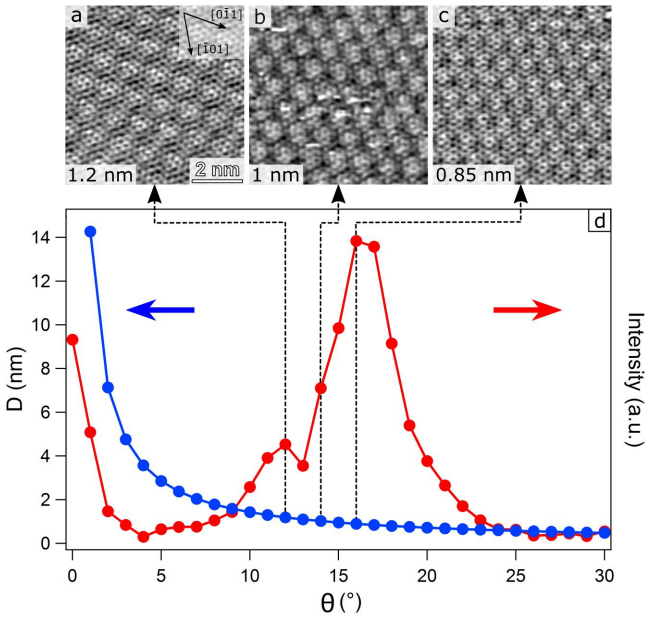

Figure 6.6: (a-c) STM images of RG exhibiting different moiré structures [(a) V = 0.02 V; I = 4 nA, (b) V = 0.025 V; I = 1 nA, (c) V= -0.2 V; I= 2 nA]. (d) Dependence of moiré periodicity (blue) and μ-LEED statistical analysis (red) of θ.

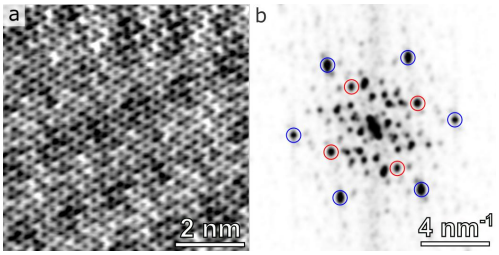

Figure 6.7: (a) STM image of a RGC domain [V= -0.2 V; I= 2 nA]. (b) FFT of (a), graphene (blue) and Ni_2C (red) spots are indicated.

istic of the surface carbidic phase on Ni(111).[9,83] Indeed, the adsorption of C atoms on Ni(111) induces a surface stress, which is relaxed by a displacement of Ni atoms and by the removal of about 13 atom% of the first metal layer.[83] The Ni and C atoms thereby rearrange into a $\sqrt{39}R16.1° \times \sqrt{39}R16.1°$ overstructure, with an almost square 5×5 Å^2 cell. In this structure, the Ni surface undergoes a *clock* reconstruction, which is reached by squares of Ni atoms rotating clock- and anti-clockwise. Since the formation of carbide underneath the graphene is typical of the RG phase only, as we will show in Chapter 7, this suggests that the RG is characterized by a different binding with the substrate than the EG, due to the lack of a direct Ni top-C interaction.[78] Figure 6.8 presents an STM

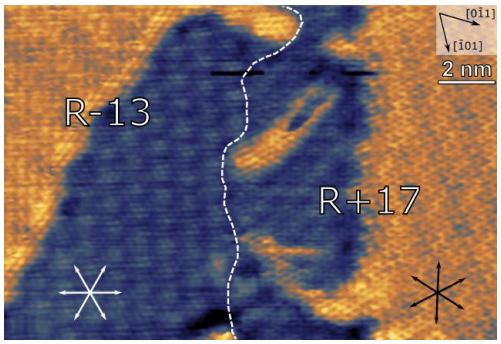

Figure 6.8: STM image at the boundary between graphene domains oriented -13 / 17°off the Ni(111) main crystallographic directions (indicated on the top right corner) [V = -0.2 V; I = 2 nA]. The dashed line marks the boundary.

image acquired on an area where regions of RG with different rotation angle co-exist, as evidenced by the different moiré pattern (blue areas). This shows that the Ni_2C nucleation occurs underneath RG regardless of the specific graphene misorientation angles. Indeed, RG is oriented -13° / +17°off the Ni(111) main crystallographic directions on the left / right side of the boundary, respectively.

6.3 Summary

In conclusion, we demonstrated the co-existence of different chemisorbed graphene configurations on Ni(111). By comparison of experimental and simulated STM images we were able to unambiguously discriminate between top-fcc, top-hcp and top-bridge graphene, inferring a general predominance of top-fcc in all our preparations. We showed also the presence of rotated graphene domains, characterized by specific moiré patterns in STM images. Moreover, upon cooling to RT, we found Ni_2C patches underneath RG islands only.

Chapter 7

Electronic properties

In this Chapter, we characterize the electronic properties of the different graphene phases on Ni(111) presented in Chapter 6, by means of spectro-microscopy measurements. Then, we show the possibility of reversibly decoupling graphene and substrate *from below*, i.e. by inducing the formation/ dissolution of carbide at the graphene/metal interface through the control of temperature. Some of the results presented here have been published in *Scientific reports*.[66]

7.1 State of the art

In CVD graphene, the presence of a metal substrate can strongly modify the peculiar properties of the graphene layer. Indeed, the interaction with the underlying catalyst can induce charge transfer mechanisms, altering the graphene doping,[84,85] or, through a strong orbital hybridization, dramatically affect the Dirac cones.[86,87] Even if for technological applications the catalyst hinders the full exploitation of graphene unique properties and, for this reason, has to be removed, from a more fundamental point of view the presence of the metal substrate paves the way for a fine tuning of the electronic properties of supported graphene flakes. In the last decade, several studies have been carried out in this direction, showing the actual possibility to synthesize metal-supported graphene with well-defined properties.[37,87–89] Among the possible substrates, the (111) surface of Nickel is a peculiar choice, offering the possibility to obtain different graphene phases, as we have shown in Chapter 6. In addition, Ni(111) is characterized by a strong interaction with the graphene overlayers,[37] that has been recently revealed to induce a fragmentation of the Dirac cone in EG.[86]
An alternative strategy to modify the properties of supported graphene is interposing buffer layer, that ensure decoupling from the metal substrate.[90–92] Such decoupling is usually obtained chemically or by intercalation procedures.[88,90,93]
In this context, the results shown in Chapter 6, concerning the surface carbide formation underneath rotated graphene flakes appear as a suitable way to decouple graphene from the Ni substrate.

7.2 Results and discussion

7.2.1 Spectro-microscopy identification

A graphene layer exhibiting the coexistence of the three phases (EG, RG, RGC) has been obtained on clean Ni(111) by exposing the sample to C_2H_4 ($p = 3 \times 10^{-6}$ mbar) at 550 °C. Subsequently, the sample was cooled to RT with a cooling rate of about 1 K/s. The bright-field (BF) LEEM image in Figure 7.1a illustrates the typical mesoscale morphology of the graphene layer at RT. As the primary diffracted beam is employed, here the structural image contrast does not distinguish between equivalent rotational domains. Analysis of the image intensity reveals the presence in the film of three coexisting phases, distinguished by different grey levels and labeled I, II and III respectively. Notably, laterally averaged LEED

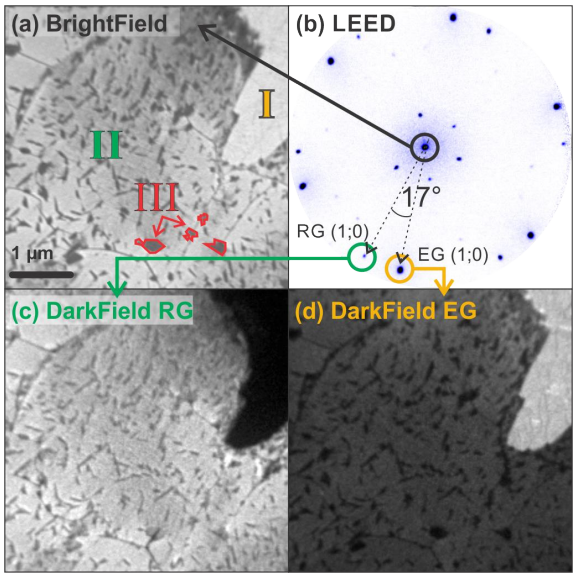

Figure 7.1: Co-existing graphene domains at the mesoscale. (a) BF-LEEM image at V_{start} = 12 V; three different graphene phases, appearing in light, neutral and dark grey, can be distinguished as regions I, II and III, respectively. Few prototypical patches of region III are highlighted by red contours. (b) μ-LEED on the same surface, V_{start} = 55 V; coexisting epitaxial and 17° rotated graphene spots are indicated. (c) DF-LEEM obtained using one of the 17° rotated spots in (b), V_{start} = 50 V. (d) DF-LEEM using one of the spots aligned with the Ni(111) lattice directions in (b) [V_{start} = 50 V].

data over the whole area (see Figure 7.1b) show only two patterns corresponding to EG and RG. The spots that closely surround the (00) beam are ascribed to double scattering processes between the Ni and RG lattices. Similar diffraction features are also found around the first order RG spots, but become clearly visible only at higher electron energies. To resolve each phase in real space, we

imaged the film using darkfield (DF) LEEM, a method that uses secondary diffracted beams to map the lateral extent of a given surface phase. As shown in Figure 7.1c-d, the images obtained using the first-order diffraction of epitaxial and rotated graphene readily assign region I (II) with EG (RG). The identifica-

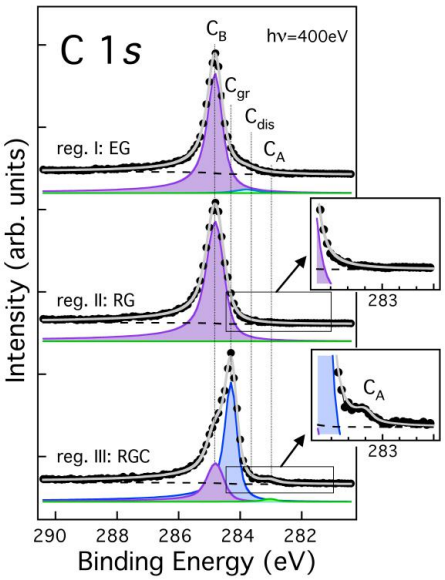

Figure 7.2: C 1s core level spectra of the different graphene phases extracted from laterally resolved XPEEM measurements [$h\nu$ = 400 eV]. Top panel: region I, corresponding to EG phase (top panel); mid Panel: region II, corresponding to RG phase; bottom panel: region III, corresponding to RGC phase.

tion of the small patches labeled III is less straightforward. Their localization within the RG phase, small lateral size (≤ 250 nm) and irregular shape suggest that they correspond to RGC areas, as previously imaged by STM.[9,94] To verify this hypothesis, we performed laterally resolved X-ray photoemission electron microscopy (XPEEM) measurements on the same region. C 1s core level spectra extracted from a sequence of XPEEM images as a function of photoelectron energy are shown in Figure 7.2. Here, each data point represents the average image intensity within well-defined areas located inside regions I, II, and III (top, central and bottom panel, respectively). Data were fitted according to the procedure introduced by Weatherup et al.,[7] using four components which were attributed to specific carbon species, as follows: C_A (green component, 283.2 eV) - surface nickel carbide; C_{Dis} (light blue component, 283.8 eV) - interstitial carbon dissolved into the near surface Ni layers; C_{Gr} (blue component, 284.4 eV, i.e. the same energy as for HOPG graphite) - weakly interacting graphene; and C_B (purple, 284.8 eV) - strongly interacting graphene. We note that both components originating from below graphene (C_{Dis} and C_A) have very small intensity, limited by the low effective photoelectron attenuation length (~ 4.4 Å) at the

kinetic energy used.[95] Surprisingly, the C 1s spectrum of both the EG and RG phases is fitted by a single peak corresponding to C_B, thus indicating that carbon has a similar interaction with the substrate in the two cases. The apparent larger width of the C_B peak ($\sim 28\%$) in RG regions is to be expected, considering that, while only two distinct sites contribute to the EG phase,[65] a larger number of adsorption sites is involved when the epitaxial match is lost due to rotation. Conversely, the spectrum extracted from regions III is remarkably different. It still shows a spurious C_B peak, originating from the adjacent RG regions: this contribution arises due to the limited lateral resolution of the microscope. However, the main peak is of C_{Gr} type, with a small but evident (see inset) carbide component (C_A) on the low-binding energy side. Such component, absent in the spectrum from region II (see inset), confirms that region III corresponds to the RGC phase. Notably, the lower value of the C_{Gr} binding energy with respect to C_B is typical of systems characterized by a weak interaction between graphene and the metal support.[96]

The π band dispersion of the three different graphene phases was investigated by microprobe angle-resolved photoelectron spectroscopy (μ-ARPES). Since our data are collected from a region measuring about 2 microns in diameter, the contributions of the RG or RGC phases in the rotated regions cannot be separated. In Figure 7.3 left we plot momentum distribution curves (MDC) through one of the K points along a plane normal to $\Gamma - K$ (see insets) for EG (left top) and mixed RG + RGC (left bottom). On EG regions we find the typical dispersion already reported in literature,[37,97,98] with a single main feature exhibiting linear dispersion crossing 2.66±0.02 eV below the Fermi energy E_F, plus a number of minor features at lower binding energies, already attributed to nickel and hybrid graphene-nickel states.[78,99] The nature of the strongest structure is presently under debate: previously assigned to the presence of a band-gap induced by the interaction with the substrate, this feature might alternatively be related to a Dirac cone shifted away from E_F, as suggested by experiments performed at 40 K,[98] or, as proposed more recently, to the main part of a fragmented Dirac cone.[86] In the MDC from mixed RG and RGC regions (Figure 7.3 left bottom), two evident structures show up. One of them (marked in green) closely resembles the main structure found for EG but is shifted about 0.45 eV towards lower binding energy (i.e. 2.20±0.06 eV); the other structure (marked in red) is centered very close to the Fermi level (0.19±0.11 eV), indicating the presence of areas with almost zero doping, and thus of quasi-free-standing nature. To correctly correlate the MDC features with the different phases, we used the dark-field XPEEM (DF-XPEEM) method,[100] using photoelectrons emitted from graphene's π band at the reciprocal space K point, close to E_F to image the surface. In the micrographs on the right hand side of Figure 7.3, obtained using this method for each of the observed features, the image intensity is proportional to the local density of states in the film. These images confirm that the MDC single structure at 2.66 eV (yellow) stems from surface areas covered by EG, and allow a clear identification of the two MDC structures recorded from the mixed RG+RGC region:

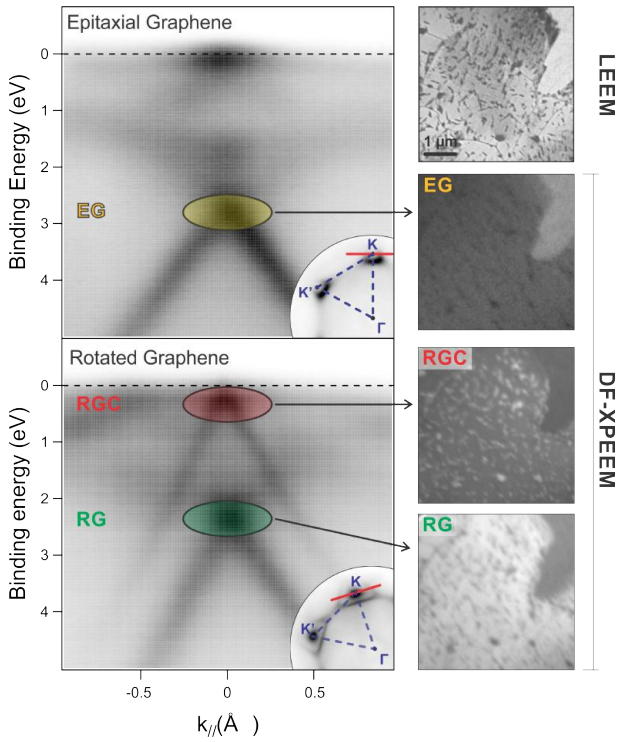

Figure 7.3: μ-ARPES measurements on epitaxial and rotated graphene regions. Left: momentum distribution curves [$h\nu$ = 40 eV]. The corresponding angular distributions of photoelectrons are shown in the insets acquired at E_B = 3.56 eV and E_B = 2.58 eV for epitaxial and rotated graphene regions, respectively. Right: Investigated graphene area as imaged by LEEM (top) [V_{start} = 12 V], and by DF-XPEEM. The dark-field images were acquired positioning an aperture at the K point in the diffraction plane, at binding energies corresponding to highlighted structures in the MDC curves on the left.

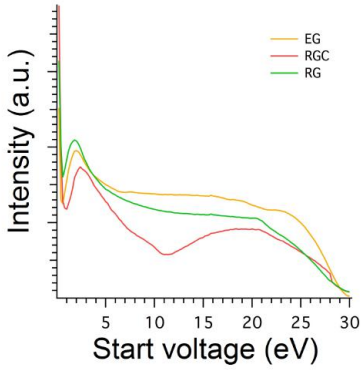

Figure 7.4: I-V curves acquired on the different graphene phases.

the lower energy structure (green), similar to the EG one, is assigned to areas of RG phase, the cone closer to the Fermi level (red) is instead strictly related to the RGC phase (as demonstrated by the inversion of contrast between the bright and dark features) and indicates that the small RGC patches are electronically decoupled from the substrate.

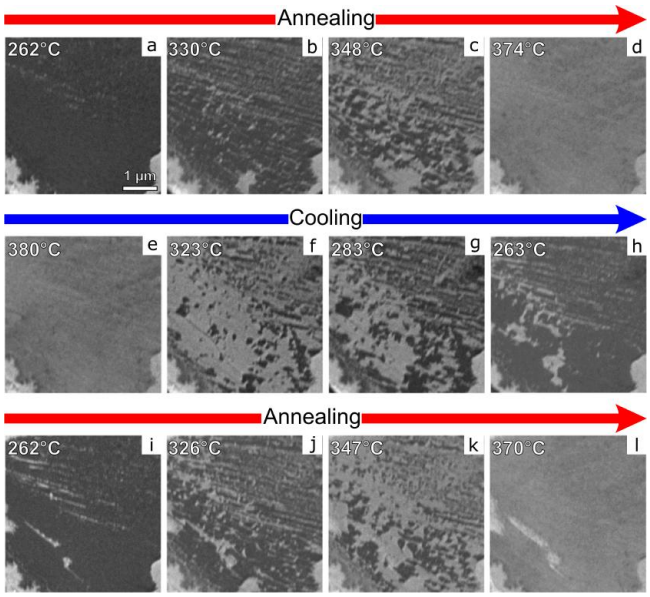

Figure 7.5: Temperature-driven formation/dissolution cycles of Ni_2C underneath graphene. The dissolution of carbide (a to d) as the temperature is increased and its re-formation upon cooling (e to f) are evidenced by the change in brightness (dark = RGC, bright = RG). The epitaxial domains in the bottom corners, which do not change with temperature, are used as markers. A second annealing (i to l) converts RGC in RG again [V_{start} = 9 V].

7.2.2 Tuning graphene/metal interaction

The question now arises whether it is possible to control the population of the RGC phase so to obtain a uniform carbidic buffer and whether this process is reversible. Clearly, such capability would allow a drastic change in the electronic properties of graphene to be obtained and finely controlled. As it will be presented in detail in Chapter 8, the RGC phase is not present during growth, but forms only upon cooling towards RT. More precisely, it nucleates at temperatures between 220 °C and 320 °C (extreme values depending on the concentration of subsurface C). So, we monitored the evolution of a RGC covered region upon thermal cycles by means of BF-LEEM, in order to monitor the formation/dissolution of the carbide layer. A safe identification of the graphene phases

comes from the differences in the I-V curves shown in Figure 7.4. Indeed, they present a sizable change in the electron reflectivity between RG and RGC at $V_{start} \simeq$ 9-12 V. In this way, it has been possible to clearly relate the contrast change with the carbide presence. Figure 7.5a shows a homogeneous RGC region, exhibiting a lateral size of few microns, obtained after keeping the sample at ~260 °C for few hours. The corresponding MDC, shown in Figure 7.6a, presents a single Dirac cone at the Fermi level ($E_D = E_F - E_{Kin} = 0.01 \pm 0.06$ eV). The Dirac energy E_D was determined after calculating the intersection point of lines fitting the two branches of the π band, which was done in an energy interval extending 2 eV below E_F. Such lines were obtained after determining the exact position of each point of the π band branches in the ($k_\parallel$, E_B) space. The error bar on E_D (95% confidence level) results from the statistical errors on the intercept and slope of the lines, not from the limited energy resolution of the SPELEEM.

As shown in Figure 7.5a-d, upon annealing, the carbide dissolves into the bulk and conversion of the initial RGC phase takes progressively place, as revealed by the brightness change in the sequence, until a homogeneous RG is obtained, as confirmed also by the MDC (Figure 7.6b), showing that at ~360 °C the cone is shifted far away from the Fermi level (-2.13 ± 0.08 eV). The process appears to be

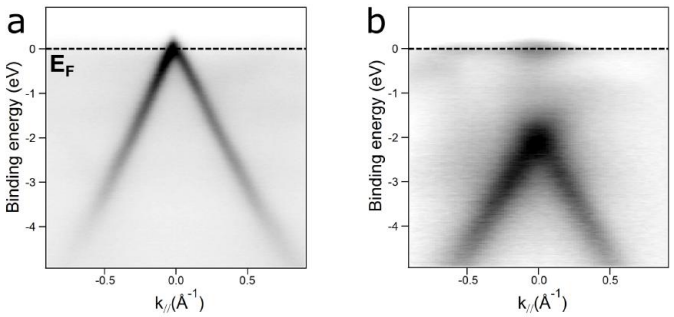

Figure 7.6: Rotated graphene/substrate coupling and decoupling during temperature cycling. (a) MDC acquired at RT from the region imaged in Figure 7.5a (RGC). (b) MDC acquired at 360 °C (RG) [$h\nu$ = 40 eV].

entirely reversible, i.e. the carbide inter-layer forms back when the temperature is lowered (e-h), dissolves once more when it is raised again (i-l), and so on. It is therefore possible to reversibly switch between the decoupled/coupled states by simply changing the temperature. We note that the switch between RGC and RG takes place only in the 220-370 °C temperature range. The carbide coverage remains constant upon further cooling below this range, while annealing in excess may lead to bilayer formation, as occurs for the thin bright stripe in panel l (see Chapter 12). The fact that the conversion is active only in a narrow temperature range implies that rapid cooling of the sample from growth to room temperature yields an almost completely carbide free graphene layer. The temperature

range where the switch is active is in agreement with previous investigations on the kinetics of C segregation on Ni samples. Indeed, in pioneering experiments, Blakely et al. [101] analyzed the temperature dependence of C segregation on the Ni(100) surface, finding it to be maximum at about 357 °C. The micro-

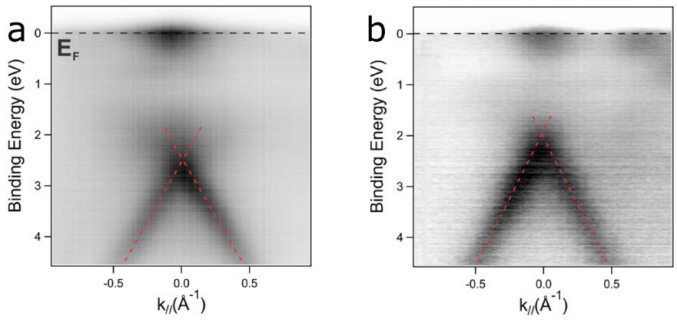

Figure 7.7: μ-ARPES momentum distribution curves acquired at 450 °C on EG and RG domains [$h\nu$ = 40 eV].

probe ARPES MDCs for the homogenous RGC and RG phases, shown in Figure 7.6c-d, unequivocally evidence the effect of the presence of the surface carbide: while direct strong interaction of graphene with Ni induces the formation of hybrid states and a pronounced modification of its electronic structure, carbide formation underneath the graphene sheet decouples microscopic regions of the layer from the substrate,[9] (almost) completely restoring its semi-metal nature. Remarkably, on Ni(111) the same rotated regions exist in two states: either decoupled or coupled to the substrate. Finally, we have measured at high temperature the MDCs of the EG and RG phases (see Figure 7.7), observing only a small shift in the position of the cones with respect to the corresponding phases at lower temperature. This further confirms that the major changes in the electronic structure are indeed due to the presence of interfacial carbide.

7.3 Summary

We investigated the electronic structure of graphene grown on Ni(111) by spectromicroscopy methods. EG and RG have been found to present unexpectedly similar electronic properties, despite the difference in the adsorption geometries, while the formation of surface carbide underneath the RG phase acts as an efficient decoupling spacer, restoring the free-standing graphene dispersion at the K point. Moreover, clear evidence is provided that micro-scale carbide domains can be reversibly formed and dissolved by just changing the temperature and deciding the time spent by the sample in the narrow temperature range where the conversion is active.

Chapter 8

Growth mechanisms

In this Chapter, we discuss the atomic-scale mechanisms governing graphene formation on Ni(111) for hydrocarbon exposures below 600 °C, by means of complementary *in situ* STM and XPS. Based on the results presented in Chapthers 6 and 7, we identify the different graphene phases, revealing the correlation between the CVD parameters, the growth process and the final graphene structures. Most of the content presented in this Chapter has been published in *ACS Nano*.[94]

8.1 State of the art

The high carbon solubility of Ni, combined with the vast parameter space of catalytic CVD and the related importance of growth kinetics,[40] makes graphene growth control, as well as an unambiguous identification of the key growth mechanisms, challenging.[102] Additional complexity arises from the formation of a stable Ni carbide surface phase.[83] Recent literature shows an in-plane coexistence of RG and Ni_2C on Ni(111) and suggests that graphene growth below 460 °C occurs via an conversion mechanism,[8] in contrast to graphene growth via carbon attachment directly on Ni(111).[93,103] This in-plane conversion has been suggested to impose a 3° rotation between the graphene and underlying Ni(111).[8] Graphene flakes exhibiting a rotation respect to the underlying Ni(111) substrate, which are unexpected given the (1 × 1) epitaxial match (see Chapter 6), have also been recently reported to grow at temperatures above 650 °C.[9,39] Notably, most data and literature to date are limited by characterization at a post-growth stage. Hence, despite the atomic structure of graphene on Ni was investigated for decades, there remains limited direct evidence of the atomistic details involved in the growth process.

8.2 Results and discussion

We investigated graphene growth on a Ni(111) surface in the 400-600 °C temperature range and adopt a simple one-step CVD process, whereby the sample is heated and cooled in UHV, and exposed to ethylene (C_2H_4). In order to take into account the exposure history and carbon contamination level in the Ni layers closest to the surface, we differentiate between clean and carbon-contaminated Ni subsurfaces. The Ni(111) substrates we refer to as having a clean subsurface are prepared by multiple cleaning cycles (Ar^+ sputtering at 2 KeV and flash annealing to 600 °C in UHV) after which no carbon signatures are observed during extended UHV annealing (~30 min in $p < 2 \times 10^{-10}$ mbar) at the growth temperature in both STM and photoemission experiments. The substrates referred to as having a carbon contaminated subsurface are samples that even after cleaning show carbon surface signatures (prior to any hydrocarbon exposure) upon heating to the growth temperature. All STM experiments have been repeated several times on different regions of the sample using the same growth conditions to ensure the observed processes are statistically representative. Specifically, the results reported in this Chapter concern about 20 experiments at 410 °C < T < 440 °C, 20 experiments at 500 °C < T < 530 °C, and 5 experiments at 550 °C < T < 600 °C, for both clean and carbon contaminated Ni sub-surfaces. Here we investigated the key growth mechanisms for the given conditions, and showed representative sequences of STM images in each case, acquired with the standard control unit, which presents limitations in terms of frame-rate (~2 images/minute). Then, in Chapter 10, we focus on one of the graphene growth mechanism presented here and, by means of the FAST unit (previously described in 3.2.3), we acquired atom-resolved time-series above video-rate, accessing processes occurring in the ms time-scale.
It is important to note that all the revealed atomic-scale mechanisms occur simultaneously, and that it is their relative balance that changes with conditions.

8.2.1 Clean subsurface (400-500 °C)

Figure 8.1a shows *in situ* STM images of the Ni catalyst surface during C_2H_4 exposure at 420 °C, representative of different stages of graphene formation during the exposure phase. Figure 8.1a shows a step edge on the initially clean Ni(111) surface which appears fuzzy due to the fast dynamics of attaching/detaching metal atoms at elevated temperature. We cannot directly resolve Ni mass transport on the terraces, as it occurs on a time scale too short to be followed with conventional STM scan speed. After a few minutes of C_2H_4 exposure, an almost complete layer of Ni_2C forms at the surface (Figure 8.1b). The structure of surface nickel carbide has been investigated and described in previous literature,[9,83] and shows a peculiar atomic arrangement, which we used as fingerprints to interpret our results. Indeed, our STM images of the intermediate structure that forms before graphene upon hydrocarbon exposure, shown

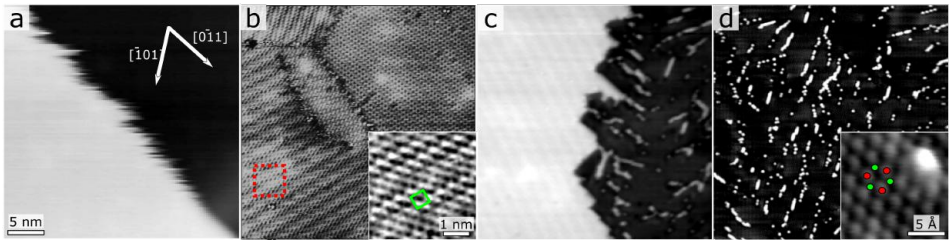

Figure 8.1: STM images acquired at 420 °C at different growth stages upon C_2H_4 exposure of clean Ni(111): (a) clean Ni(111) step edge; (b) nickel carbide (Ni_2C) domains on Ni(111). Inset: atomic resolution image of the area in the dotted square. The almost square 5×5 Å^2 unit cell is marked in green. (c) Domain boundary between Ni_2C (left) and graphene (right), during conversion; (d) defected graphene on Ni(111). Inset: Atomically resolved image of graphene. The inequivalent C atoms of a graphene ring are marked in blue and green. Scanning parameters: (a) V = -2 V, I = 0.5 nA; (b) V = -10 mV, I =1 nA; (c) V = -100 mV, I = 0.1 nA; (d) V = -50 mV, I = 0.7 nA (insets: V = -10 mV, I = 1 nA (b); V = -300 mV, I = 0.5 nA (d)).

in Figure 8.1b, exhibit both stripe periodicity and atomic scale arrangement in perfect agreement with the results reported in literature,[9,83] as well as the same LEED pattern, which confirms our assignment. After several minutes of further continuous exposure, the Ni_2C starts to convert into MLG (Figure 8.1 c), a process which proceeds over a time scale of a few hours at the given conditions, until a complete graphene monolayer is produced (Figure 8.1 d). The atomic scale appearance of this graphene layer does not show any moiré pattern, resembling the EG one, as extensively discussed in Chapter 6. We estimate a defect density of $\sim 1-2\%$, calculated as the fraction of missing C atoms at the bright spots in the STM images, which we suggest are due to the presence of substitutional Ni atoms, as will be confirmed in Chapter 11. We find the Ni_2C conversion to be the principal graphene growth route on clean Ni for the low temperature range probed (400-500 °C). Figure 8.2 is representative of the behavior observed across our experiments, and identifies two different mechanisms by which this conversion proceeds: an in-plane conversion mechanism and a distinct two-layer mechanism. Figure 8.2a shows STM data representative of the in-plane conversion mechanism. The sequence of images shows a fixed area of the surface during C_2H_4 (p = 2×10^{-7} mbar) exposure at 420 °C. According to the detailed height analysis present in Appendix A, it is clearly seen that EG (right hand side, Figure 8.2a) expands at the expense of the initial Ni_2C structure (on the left, Figure 8.2a), whereby the MLG is adsorbed on the same Ni layer supporting the Ni_2C. Figure 8.2b schematically highlights the details of this in-plane conversion mechanism: Ni atoms are ejected from the reconstructed Ni_2C layer and quickly diffuse away due to their high mobility; concurrently the surface carbon coverage increases and the hexagonal graphitic network forms.

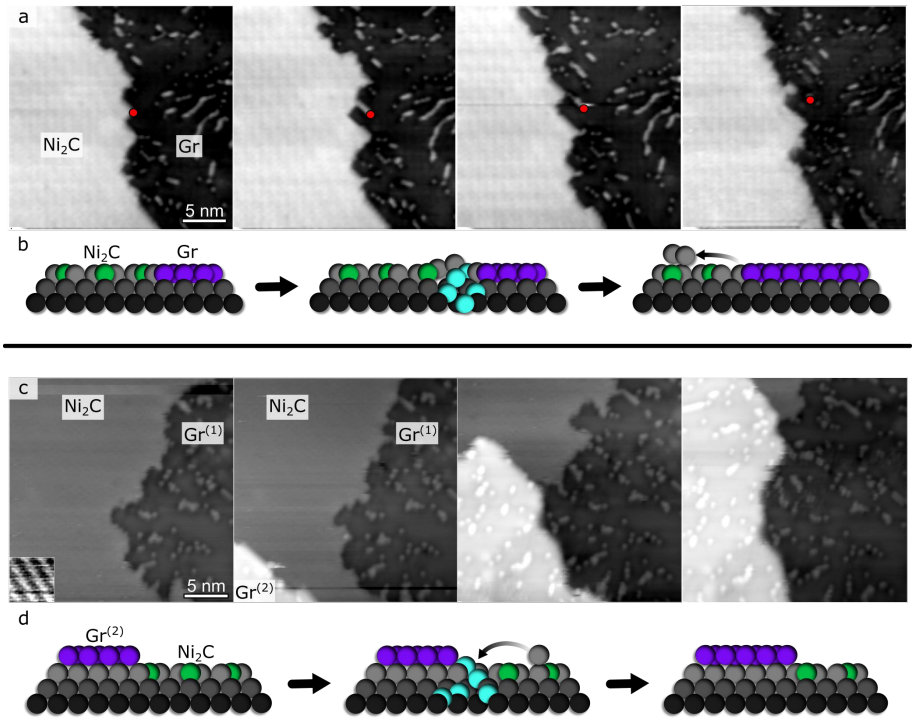

Figure 8.2: STM images and schematic models of Ni carbide to graphene conversion: (a and b) in-plane conversion. In the STM images, the region on the left is covered by Ni_2C, the region on the right by graphene. The red dot marks the position of a fixed defect on the surface. Ni atoms are ejected when additional C atoms reach the surface from the bulk to extend the graphene region. (c-d) Two-layer conversion. In the STM images, while the graphene region labeled $Gr^{(1)}$ grows from Ni_2C via in-plane conversion, the graphene island labeled $Gr^{(2)}$ grows on the same carbide domain by a two-layer conversion mechanism. Here additional C atoms reach the graphene/carbide interface, the Ni layer deconstructs to (1 × 1), and the graphene island expands. In the lower left corner of the first STM image in sequence, Ni_2C stripes are highlighted by a different image contrast. In both (a) and (c): T = 420 °C, p(C_2H_4) = 2×10^{-7} mbar. Time between displayed frames: ~120 s (a) and ~90 s (c). Scanning parameters: (a) V = -100 mV, I = 0.1 nA; (c) V = -250 mV, I = 0.5 nA. In the schematic models, gray/light-blue/green/ purple balls represent Ni/dissolved C/carbidic C/graphenic C atoms.

As discussed in the following, based on previous literature and supported by our findings on contaminated substrates (see below), we propose that the additional carbon atoms, in this case, reach the carbide/graphene interface from below the surface and thereby displace and eject Ni surface atoms. EG growth occurs during exposure at fixed temperature, i.e. the widely held assumption

that graphene growth on Ni is solely based on carbon precipitation upon cooling is incorrect.[41,104] During exposure, hydrocarbon molecules adsorb on the Ni surface, dissociate, and C atoms dissolve into the Ni. Ni_2C nucleation and conversion requires the build-up of a sufficient carbon concentration at the Ni surface, which relates to the observed incubation times. Previously, Weatherup et al.[40] established a kinetic model whereby graphene growth proceeds by the build-up of a local carbon supersaturation at the Ni surface, which depends on the flux balance between carbon reaching and leaving the catalyst surface. Carbon can arrive via the gas phase (on the clean portion of the surface or through defects on already carbon-covered areas) or via segregation from the catalyst bulk, whilst it can leave via diffusion into the catalyst bulk. This general kinetic model is applicable to every kind of substrate, both for the Ni_2C formation and conversion, as well as for graphene formation directly on Ni. It is interesting to note that in model systems the Ni_2C layer has been reported to passivate the Ni catalyst surface (at least at step edges).[105] This can impede carbon precursor dissociation in an analogous manner to graphene coverage.[40] The more complete this passivation, the more the carbon flux to the Ni surface/interface will be dominated by isothermal segregation from the Ni bulk. This may account for the notable delay we observe in graphene nucleation following Ni_2C formation. The general scenario of carbon dissolution and re-segregation to the surface to form graphene by the observed in-plane Ni_2C conversion mechanism is similar to what has been proposed by Lahiri et al.,[8] and is also consistent with their DFT results, showing that the process in which Ni atoms at the carbide/graphene interface are removed from Ni_2C and replaced by carbon atoms from the bulk, is exothermic. This previous post-growth data, however, showed a 3° rotation between the graphene and underlying Ni(111) which was suggested to be due to the preference of the growing graphene to form a coincidence structure with the surface carbide at their 1D interface.[8] Our *in situ* data clearly shows that in all cases Ni_2C conversion leads to only EG formation and we further show that inconsistencies in literature regarding the formation of rotated domains due to Ni_2C are likely to arise from ambiguity in the interpretation of post-growth data,[8,9] as discussed in detail below. Figure 8.2c shows STM data representative of a different two-layer Ni_2C conversion mechanism. As shown in Appendix A, while the graphene island labeled $Gr^{(1)}$ grows via the in-plane conversion mechanism described above at the edges of the Ni_2C region, the MLG domain labeled $Gr^{(2)}$ appears to expand on (and exclusively on) the same Ni_2C region. The height analysis also shows that $Gr^{(2)}$ grows on a metal atomic layer, probably formed from Ni atoms which were initially part of the Ni_2C along with additional Ni atoms fast diffusing on the surface, rather than as an overlayer on the Ni_2C as previously suggested,[9] or as a bilayer graphene region. The proposed conversion process leading to the formation of the $Gr^{(2)}$ graphene domain is schematically outlined in Figure 8.2d: carbon atoms in the Ni_2C layer are promoted one layer higher, whilst the Ni surface deconstructs back to (1×1), requiring mass transport to supply the additional Ni. Further car-

bon atoms arrive, and a graphene island forms. The reaction/conversion front of this two-layer mechanism proceeds at ~ 0.8 Å/s, much faster than the reaction front of the in-plane conversion (~ 0.15 Å/s). For the in-plane conversion, the topmost Ni atoms corresponding to 87% of a Ni(111) layer have to be locally removed whilst for the two-layer conversion, additional Ni atoms corresponding to only 13% of a Ni(111) layer are required to reconstruct the top-most metal layer. We note that the difference in graphene growth rate between the mechanisms may relate to this difference in the required Ni mass transport. In the temperature range considered here, however, we always find the most common growth process to be the in-plane conversion mechanism, indicating a kinetic selection dominated by a lower nucleation barrier for this process.It is important to note, that none of our post-growth measurements reveal the formation of further carbon structures underneath the EG on Ni(111) following cooling.
Figure 8.3 shows the time-resolved chemical evolution of the C 1s spectra for the Ni(111) surface during graphene growth, measured by means of synchrotron radiation *in situ* XPS at the ISISS beamline (BESSY II, Berlin). The experimental setup consists mainly of a reaction cell (base pressure ~ 10^{-7} mbar) attached to a set of differentially pumped electrostatic lenses and a differential-pumped analyzer (Phoibos 150, SPECS GmbH).[106] Samples were pre-treated by oxidation (p(O_2) = 1×10^{-4} mbar, 30 s) and reduction (p(H_2) = 1×10^{-4} mbar, 3') at ~600 °C to leave a clean Ni surface with no detectable C species in the C 1s spectra, prior to hydrocarbon exposures. Upon C_2H_4 exposure (p = 6×10^{-7} mbar), we observe the appearance of four principal components, previously described in Chapter 7: C_A (green component, 283.2 eV) - surface nickel carbide; C_{Dis} (light blue component, 283.8 eV) - interstitial carbon dissolved into the near surface Ni layers; C_{Gr} (blue component, 284.4 eV) - weakly interacting graphene; and C_B (purple, 284.8 eV) - strongly interacting graphene. Upon C_2H_4 exposure, a dominant C_A component appears, followed by the emergence of C_B. The intensities of C_{Dis} and C_{Gr} components are inside the deconvolution procedure error. C_B grows with continuing hydrocarbon exposure becoming the dominant species, accompanied by a strong reduction in the C_A peak intensity, until the C_B peak intensity almost saturates (the exposure was stopped before reaching complete monolayer coverage). This peak evolution allows us to generalize our findings for a wider range of vacuum conditions (both base and exposure pressures): as soon as the hydrocarbon exposure starts, carbon dissociates on the bare Ni(111) surface, dissolves in to the Ni leading to an increase in the level of dissolved carbon in the subsurface, and the Ni_2C phase forms across the surface. In this case the induction time is shorter than for STM experiments (~1' vs. ~10'), as expected due to the higher C_2H_4 pressure (~3 times).[40] With continuing hydrocarbon exposure, the Ni_2C gradually transforms into epitaxial graphene until almost complete coverage with an EG is achieved.

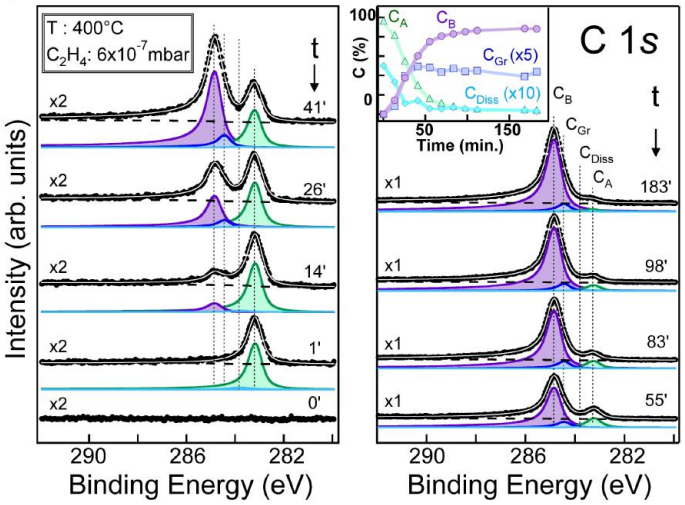

Figure 8.3: Time-resolved *in situ* high resolution XPS C 1s core level spectra during low pressure CVD on a clean subsurface Ni(111) single crystal [$p_{bg} \sim 10^{-7}$ mbar, T = 400 °C, p(C_2H_4) = 6×10^{-7} mbar]. Time = 0 is relative to when the C_2H_4 valve is opened and spectral acquisition begins, however exposure pressure is not instantaneously reached. All spectra are collected in normal emission geometry at photon energies of 435 eV (surface sensitive; $\lambda_{escape} \sim 7$ Å) with a spectral resolution of ~0.3 eV. Superimposed to the C 1s experimental data (dots) are the fitting results (light gray) together with the Shirley background (dotted line) and the four Doniach-Sunjić C_A (green), C_B (purple), C_{Gr} (blue) and C_{Dis} (light-blue) components). The inset shows the percentage of the different carbon species (C_A (green triangles), C_B (purple dots), C_{Gr} (blue squares) and C_{Dis} (light-blue diamonds), as determined by the area under the corresponding peaks.

8.2.2 Clean subsurface (500-600 °C)

Figure 8.4 shows representative STM images of graphene growth on clean Ni(111) above 500 °C. Ni_2C formation during the first growth stages is progressively reduced, although not completely suppressed, as the exposure temperature is increased above 500 °C, and a different dominant graphene growth route sets in, as revealed by the STM images, whereby graphene grows directly on Ni(111) via Ni replacement mechanisms. After nucleation, graphene islands grow embedded into the Ni surface, preferentially elongated in a close-packed Ni(111) direction (see dark stripe in Figure 8.4a). The final complete monolayer includes not only epitaxial regions, but also moiré domains, as shown in Figure 8.4b. As shown in Chapter 7, the moiré patterns are due to a rotation of the graphene layer with respect to the underlying Ni(111) surface. The balance between EG and RG domains in the final surface shows a strong dependence on the growth temperature: at higher temperatures, rotated domains are increasingly present in STM images and at the same time, arches of extra spots appear in the LEED pattern,

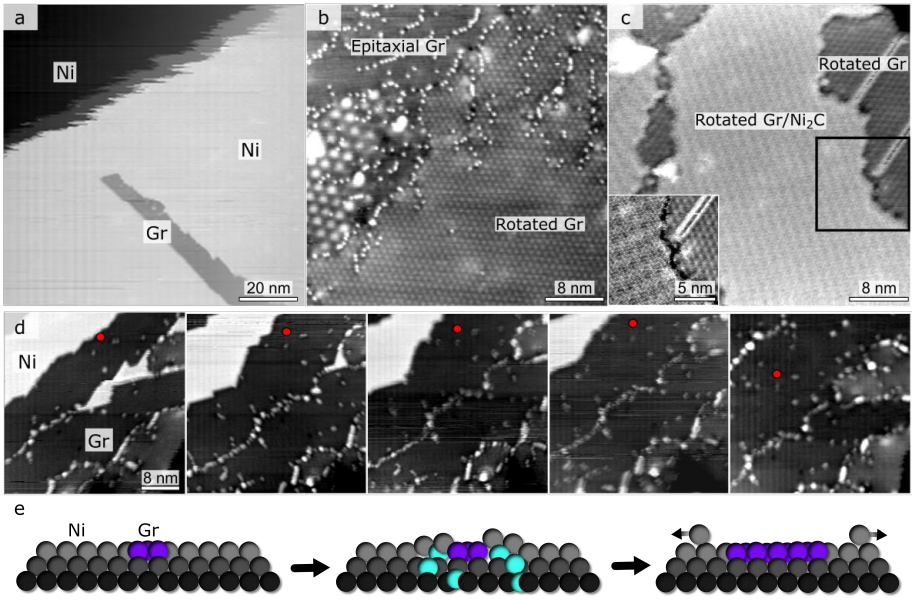

Figure 8.4: STM images and schematic models of graphene growth on clean Ni(111)above 500 °C. All images acquired at 520 °C unless specified. (a) Embedded graphene island (dark stripe) in the middle of a clean Ni(111) terrace. (b) Final MLG layer after growth, showing regions of rotated (right) and of epitaxial (top-left) graphene [V = -600 mV, I = 1 nA]. (c) STM image at RT showing a graphene covered region grown at 520 °C after cooling at room temperature: Ni_2C islands form below rotated graphene regions [V = -200 mV, I = 2 nA]. Inset: magnification of the boundary between rotated graphene (right) and graphene on Ni_2C (left) [V = -100 mV, I = 2 nA]. (d-e) Growth mechanism. Graphene islands embedded into the Ni substrate expand by segregation of additional C atoms and ejection of additional Ni atoms. The red dot marks the position of a fixed defect on the surface. In the schematic models, gray/light-blue/green/blue balls represent Ni/dissolved C/carbidic C/graphenic C atoms. p(C_2H_4)=2×10^{-7} mbar, consecutive images with acquisition time ~30 s/frame [V = -2 V, I = 0.5 nA].

centered at ~ 17°, as previously described in Chapter 7. Growth of RG directly on Ni(111) is consistent with a previous LEED/LEEM study,[93] albeit therein a critical growth temperature of 650 °C was assumed. We therefore attribute the increasing coverage of RG for increasing temperature to kinetic effects. We have not captured here the very first nucleation stages, but the sequence of STM images in Figure 8.4 d illustrates how embedded graphene regions grow. Elongated MLG islands expand on the same terrace, one towards the other, at ~1 Å/s, progressively reducing the width of the bare Ni surface in between, until only a line of point defects remains. This growth mechanism can be rationalized as schematically outlined in Figure 8.4 e: when a first graphene nucleus is present,

additional C atoms segregate to the surface at its borders, facilitating the ejection of Ni atoms, and attach to the graphene island edges, thus replacing surface Ni atoms. In this way, the anchoring points are shifted and the MLG island expands. A similar growth by the removal of metal atoms at graphene edges has also been observed on Rh(111) [107] and Ru(0001), [108,109] albeit as a more minor growth mechanism. For the latter surfaces, the main growth mechanism is typically suggested to be carbon attachment to the edges of graphene islands atop the metal. The difference with the growth on Ni can be explained in view of the significantly higher carbon solubility in Ni than in Rh and Ru. [110] It is noteworthy that we have also observed a mechanism here by which MLG islands expand directly on Ni(111), i.e. where the graphene is not embedded. However, as outlined below, we find this mechanism to be dominant only in the case of a carbon contaminated subsurface.
Upon cooling of the RG covered surface to RT, a different STM contrast appears in some regions (Figure 8.4c). As shown in Chapter 6, this different contrast was previously observed and attributed to the presence of Ni_2C islands underneath RG. [9] Our *in situ* data here clearly shows that this structure results from the precipitation of carbon upon cooling, according to the data presented in Chapter 7.

8.2.3 Carbon-contaminated subsurface

The mechanisms established above all refer to conventional CVD parameters such as temperature and pressure, which can be carefully controlled. Figures 8.5 and 8.6, however, show that the dominant graphene growth mechanism critically depends also on the near-surface carbon concentration which is much more difficult to control as it is intimately linked to the full history of the catalyst and all possible sources of contamination. It has been previously highlighted how minor, routinely present levels of carbon contamination can significantly influence CNT growth kinetics. [111] Here we show that the graphene growth scenario can change completely if the Ni(111) substrate does not undergo a complete cleaning procedure and some residual carbon contamination is present in the subsurface, a case which we refer to as carbon-contaminated subsurface. For this case, even though the Ni surface appears clean at RT in XPS and LEED, with only carbide islands present in STM images, as soon as the temperature is increased to the growth temperature, prior to exposure, we observe the formation of graphene seeds at the Ni surface, both at Ni steps (Figures 8.5a), and as small islands on top of metal terraces (Figures 8.5b). Once at the growth temperature, in UHV conditions, the seeds expand even without gas exposure, fed by C atoms from the subsurface reservoir, leading to a complete, mainly EG coverage over the whole temperature range investigated (Figures 8.5 c), without any intermediate carbide phase. This picture is confirmed by all our XPS (Figures 8.6), STM and LEED (not shown) experiments. The expansion of the graphene seeds thereby occurs on top of the Ni substrate, by C atom addition to graphene

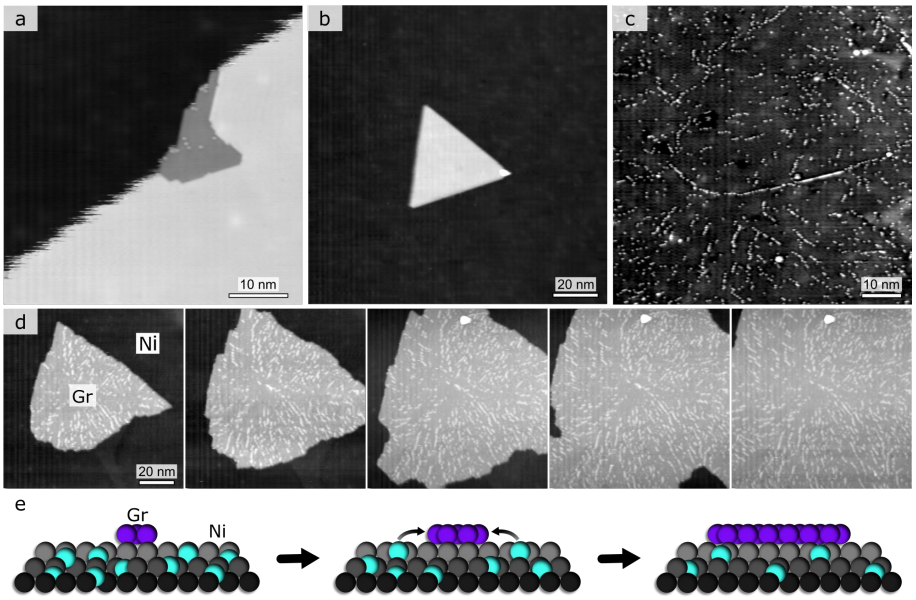

Figure 8.5: Graphene growth on Ni in case of C-contaminated subsurface. STM images during annealing at 520 °C (a-c). Graphene seeds are already present as soon as the temperature is reached, both at step edge (a) [V = -600 mV, I = 0.5 nA] and on a terrace (b) [V = -300 mV, I = 0.8 nA]; (c) the complete epitaxial MLG after ~60' [V = -400 mV, I = 0.7 nA]. (d) STM images of a graphene seed growth on a Ni terrace at 410 °C without hydrocarbon exposure ($p_{bg} = 2 \times 10^{-10}$ mbar). The expansion occurs by C attachment to the edges. Time between displayed frames: ~10 min [V = -600 mV, I = 0.4 nA]. (e) Schematic model of the growth mechanism imaged in (d), gray/light-blue/purple balls represent Ni/dissolved C/graphenic C atoms.

edges, as shown by the selected frames in Figure 8.5d and schematically outlined in Figures 8.5e. Such graphene growth in UHV without hydrocarbon exposure is clear evidence of the capability of subsurface C to diffuse to the surface and form graphene. A detailed investigations of the seeded graphene growth mechanism is present in Chapter 10.

8.3 Summary

We have directly revealed and characterized a number of competing atomistic mechanisms of graphene formation on Ni for technologically relevant low temperature CVD via complementary STM and XPS, both performed *in situ* under *in operando* conditions. For clean Ni(111), below 500 °C the formation of an intermediate, structural surface carbide (Ni_2C) is favored, which converts into EG. Above 500 °C, graphene predominantly grows directly on Ni(111) via replace-

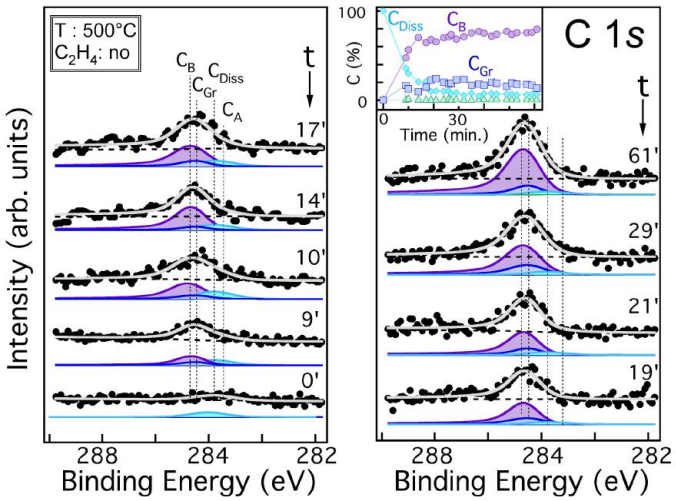

Figure 8.6: Time-resolved *in situ* low resolution XPS C 1s core level spectra during annealing at 500 °C the carbon contaminated subsurface Ni(111) single crystal ($p_{bg} = 1 \times 10^{-10}$ mbar). Time = 0 is relative to when the spectral acquisition begins. All spectra are collected in normal emission geometry at photon energies of 1253.6 eV (surface sensitive; $\lambda_{escape} \sim 15$ Å) with a spectral resolution of ~0.8 eV. Superimposed to the C 1s experimental data (dots) are the fitting results (light gray) together with the Shirley background (dotted line) and the four Doniach-Sunjić C_A (green), C_B (purple), C_{Gr} (blue) and C_{Dis} (light-blue) components). The inset shows the percentage of the different carbon species [C_A (green triangles), C_B (purple dots), C_{Gr} (blue squares) and C_{Dis} (light-blue diamonds)], as determined by the area under the corresponding peaks.

ment mechanisms leading to embedded EG and RG domains. Surface carbide formation is thereby not the source of graphene grain rotation, rather RG domains nucleate directly on Ni(111) at sufficiently high temperatures and their increased relative abundance (compared to EG) with increasing temperature is kinetically determined. We showed that the dominant graphene growth mechanism critically depends not only on conventional CVD parameters but also on the near-surface carbon concentration which is much more difficult to control, as it is intimately linked to the full history of the catalyst and all possible sources of contamination. Given a carbon-contaminated surface prior to hydrocarbon exposure, for instance, EG growth directly on Ni via the expansion of such seeds by C addition at their edges predominates across the whole temperature range probed.

Chapter 9

Edges structures and passivation

In this Chapter, we presented the atomic structure of CVD graphene edges on Ni(111) both during growth at 470 °C and after cooling down to RT, investigated by STM in combination with DFT. In this way, we reveal that the edge passivation depends on the sample temperature: while during the growth the flake edges are bent toward the substrate, at RT hydrogen atoms saturate the carbon dangling bonds, detaching the edges from the metal. Most of the results presented here have been published in *Nano Letters*.[112]

9.1 State of the art

The electronic, magnetic, and chemical properties of graphene and graphitic nanostructures are strongly influenced by the presence and the structure of their edges.[10,113–120] In free-standing graphene, two main types of edge structures are possible, oriented at 90° from each other: zigzag (z) and armchair (AC).[121–125] Along the zigzag direction, a subset of further reconstructions has been evidenced, both theoretically and experimentally, including: (i) the so-called $5-7$ reconstruction, with pentagons/heptagons arranged in a double periodicity;[123–127] (ii) the Klein edge (k), a zigzag edge with an additional carbon bonded to each terminal zigzag C atom;[128,129] (iii) the reconstructed Klein (rk) edge, where the additional C atoms in the k edge bind in couples forming ending pentagons.[130] When growing graphene by CVD, as usually done for large-scale production, the edge morphology, as well as its properties, are strongly influenced by the interaction with the substrate.[131–137] Furthermore, the edge-substrate interaction also plays a major role in the dynamics of graphene formation, steering the growth process[138–141] and the flake orientation.[82] These effects are particularly relevant in case of graphene epitaxial growth on substrates with a small lattice mismatch, as Ni(111) and Co(0001), where the metal surface breaks the symmetry of the hexagonal lattice, thus necessarily yielding two inequivalent structures on adjacent edges of hexagonal islands.[142,143] Recently, Prezzi et al.[143] demonstrated the presence of zigzag and Klein structures on inequivalent edges

on graphene islands on Co(0001). The final C atoms are always placed over surface hollow sites and passivated by the substrate. Inequivalent edges were also experimentally imaged on Ni(111) by Garcia-Lekue et al. [135] and tentatively assigned to zigzag and 5-7 structures.
It has to be noted, that experimental investigations, as well as theoretical calculations, were performed at cryogenic temperatures, i.e. far away both from the conditions relevant for growth and from those relevant for the operation of graphene-based devices.

9.2 Results and discussion

The high-resolution STM image in Figure 9.1a reveals the structure of the two inequivalent adjacent edges of graphene islands over Ni(111) at RT, i.e. in post-growth conditions. Since atomic resolution is achieved here on both the graph-

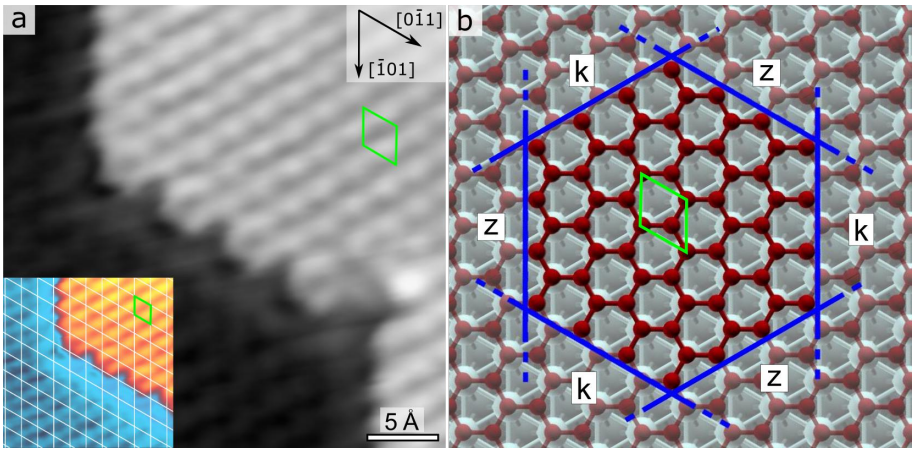

Figure 9.1: Graphene edges on Ni(111). (a) STM image acquired at RT and showing a graphene island (right) grown on top of a Ni terrace (left) [V = -10 mV, I = 20 nA]. Inset: a grid intersecting on top of the Ni atoms is drawn on a zoom in (a). A two-color scale is used to better highlight the Ni atoms. (b) Stick-and-ball model of a graphene layer on Ni(111). Blue lines indicate cuts passing at hollow C atoms and oriented along the six high-symmetry directions. The expected inequivalent edges of the resulting graphene island are marked as z (zigzag) and k (Klein). A unit cell is highlighted.

ene island and the surrounding clean Ni(111), we can place a grid intersecting on top of the metal substrate atoms, as shown in the inset. In this way, knowing the Ni crystal orientation and stacking (see Chapter 6), we can safely identify the structure of the island as top-fcc, where the bright features in the lower part of the rhombic cells of the grid correspond to C atoms in hollow fcc sites. As showed in Chapter 6, this is statistically the most abundant configuration on this surface. [65] Since sample crystallographic orientation is known, looking at

the grid, it is evident that all edges are aligned along the substrate lattice $< 0\bar{1}1 >$ and $< \bar{1}01 >$ directions, and terminate with C atoms in hollow (or near-hollow) sites, as for graphene/Co(0001).[143] Such preference, along with the threefold symmetry of the substrate, impedes the formation of only zigzag edges, as explained also by Artyukhov et al.[142] This is visualized in the schematic model in Figure 9.1b: only along three of the six high-symmetry directions of the substrate, a graphene flake can be cut in such a way that its edge is made of terminal C atoms sitting in hollow sites and forming a zigzag with the second line C atoms. In the other three directions, i.e. at the adjacent or opposite sides, the edge with C in hollow results in a Klein geometry. In addition, in the experimental images the Klein geometry seems further reconstructed into a double periodicity configuration, which in principle can be related to both rk and 5-7 edges.

9.2.1 Substrate passivation

Once clarified the effect of the substrate symmetry on the edge structure, we focus on the detailed analysis of the edge morphology at the atomic level. We first investigate a graphene flake during growth. As we discussed in Chapter 8, different routes are possible for CVD graphene formation on Ni(111): carbide conversion, embedded growth on clean Ni, seeded growth on top of carbon contaminated subsurface. It is possible to selectively discriminate between the three routes by a careful control on the CVD parameters (in particular growth temperature and initial substrate contamination). We choose here to follow a seeded growth at 470 °C without hydrocarbon exposure, which gives graphene flakes directly growing above the clean Ni substrate, without any intermediate carbide phase, with an average front velocity estimated to be higher than 0.2 nm/s. Due to this high growth speed, a direct imaging of the growing edges with conventional STM scan rates typically achievable by commercial microscopes is impossible. Conversely, our innovative FAST scan system[45] allows us to observe rapidly evolving structures with atomic resolution (see paragraph 3.2.3). In the experiments discussed here, image time-series were acquired in quasi-constant height mode with a frame rate of 4 Hz (fast scanning frequency of 800 Hz). This rate allowed us to acquire static images of the graphene edges at 470 °C with atomic resolution. In the left column of Figure 9.2a-c, frames acquired on two inequivalent edges are shown. The appearance of the images already suggests that they correspond to z and k edges, respectively. Notably, at variance with the edges imaged at RT (see Figure 9.1), at 470 °C we never see a double periodicity in any edge orientation, which rules out 5-7 and rk reconstructions. The identification of the edge structures as z and k is confirmed by our DFT calculations, which give simulated images in excellent agreement with the experimental ones (central column in Figure 9.2a-c). The exclusion of different configurations is further corroborated by the comparison between experimental and simulated STM images, and by energetics (not shown). DFT predicts that z and k edges are

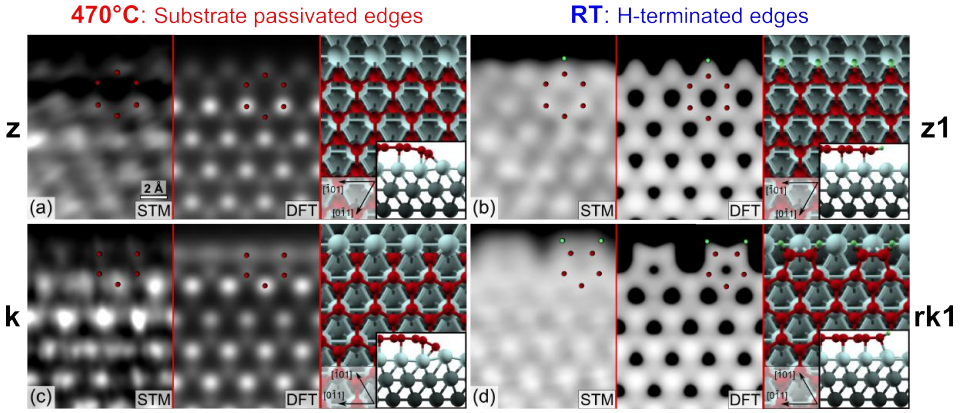

Figure 9.2: Atomic structure of graphene edges on Ni(111) along the 2 inequivalent directions, imaged at different temperatures. Notice that images and models in (c) and (d) are rotated with respect to images and models in (a) and (b). (a,c) FAST STM images acquired in 250 ms during growth at 470 °C in quasi-constant height mode (left), constant height DFT-simulated images (center) and stick-and-ball models of the calculated geometries (right). (b,d) Post-growth STM images acquired at RT in constant current mode (left), constant current DFT-simulated images (center) and stick-and-ball models of the calculated geometries (right). Scanning parameters: (a,c) experimental parameters: V = 9 mV, I = 1.3 nA; distance of 0.5 Å from graphene for DFT images; (b,d) experimental parameters: V = 200 mV, I = 20 nA; integrated density of states isovalue of 7×10^{-5} | e | / a_0^3. for DFT images. In all stick-and-ball models red (grey) balls are C (Ni) atoms, while small green balls are H atoms. On all images red (green) dots are drawn at the position of C (H) atoms.

well stabilized by a strong binding with the substrate of the terminal C atoms in hollow-fcc sites, which bend towards the metal, as clearly visible in the optimized structure of the corresponding stick-and-ball models in Figure 9.2a-c. The edge-metal bond has a covalent nature, as confirmed not only by the optimized DFT structure, but also by the plot of the calculated electronic charge density shown in Figure 9.3. A similar effect (i.e. bending induced by the covalent graphene-edge/substrate binding) was observed also on Ir(111),[138] to our knowledge the only previous experimental work probing the edge-metal interaction during growth. The bending at the edges results in a reduced brightness of the last row of C atoms in both simulated and experimental STM images of the edges, regardless of their z or k structure, as for graphene edges on Co(0001) imaged at 4.9 K.[143]

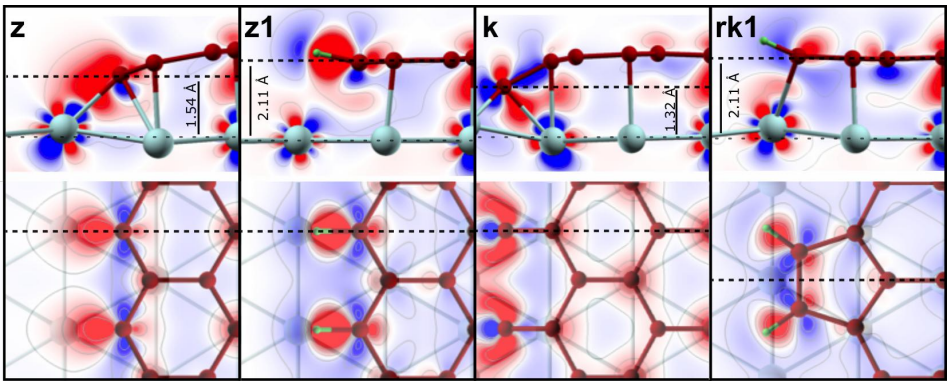

Figure 9.3: Charge distributions of z, z1, k and rk1 graphene edges on Ni(111). Electron density difference plots are obtained subtracting the electron density distribution of the graphene and of the substrate calculated separately from that of the total system. For each configuration, side (top panels) and top (bottom panels) views are shown, with the essential parts of the corresponding stick-and-ball models superimposed for reference; dashed lines indicate the planes chosen for the electron density plots; blue/red colors correspond to electron depletion/accumulation ranging from -15 to +15 $\times 10^{-3}$ | e | $/a_0^3$. In the upper panels, the height of the terminal C atoms with respect to the Ni substrate is also indicated.

9.2.2 Hydrogen termination

If the growth is quenched by cooling the sample to RT before completion of the monolayer, supported graphene flakes as the one in Figure 9.1a result. Experimental high-resolution STM images acquired in constant current mode at RT (see left column in Figure 9.2b-d) reveal the atomic structure of the two inequivalent edges along the directions exhibiting z and k geometry, respectively, at the growth temperature. These images clearly show important differences with respect to the corresponding ones acquired at growth temperature. Strikingly, this time no reduction of the brightness for the last row of C atoms, but rather a sharp step is observed for both the z and the k edges. Furthermore, along the direction corresponding to k geometry (Figure 9.2d), the protruding hollow C atoms are apparently joined into couples, giving rise to pentagons, suggesting a 5-7 or a rk reconstruction. In Figure 9.4, the STM image is shown with superimposed models of the two geometries. This comparison reveals a much better match of the experimental image with the rk model (Figure 9.4a), allowing us to exclude the 5-7 reconstruction (Figure 9.4b), recently proposed by Garcia-Lekue et al. [144] Still, the observed experimental images are not compatible with our simulated images of any kind of clean graphene edges passivated by the Ni(111) substrate. Thus, in order to retrieve the experimental brightness we have to passivate the edges in a different way. Considering that H_2 is the most abundant

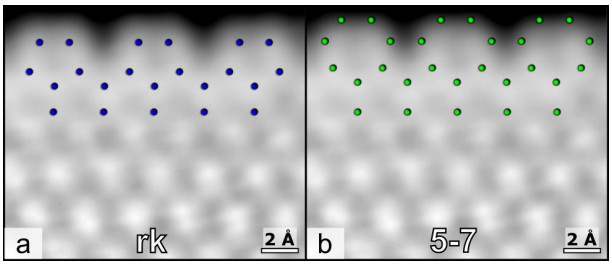

Figure 9.4: Comparison between (a) rk and (b) 5-7 edge geometries. Models are superimposed to the constant current STM image acquired at RT [V = 200 mV, I = 20 nA].

contaminant in any UHV system and that graphene edges can be hydrogenated, certainly in free-standing flakes [124,125] but even on metal substrates if exposed to atomic H, [145] we examine in details the interaction of the graphene edges with an H_2 molecule. Firstly we consider the possibility that the H_2 molecule is directly trapped and dissociated by the ending C atoms. Our simulations show that indeed dissociation would take readily place if the impinging molecule gets close enough to the edge, but indicate also that the molecule can experience a significant barrier when approaching from the gas phase. On the other side, it is well known that the H_2 molecule easily dissociates on the clean Ni(111) surface, [146] with a DFT estimated activation barrier ranging from few meV [147,148] to a maximum of 0.10 eV. [149] Our DFT calculations show that atomic hydrogen can indeed easily access and hydrogenate the graphene edges, thus yielding a stable structure with one H atom bound to each terminal C atom. Once hydrogenated, the edge is no longer bent towards the substrate, due to the breaking of the covalent bonds with the metal. This is clearly visible in the optimized structures shown by the stick-and-ball models in Figure 9.2b-d, in the corresponding calculated charge density plots and atomic projected density of states in Figure 9.3. The central column in Figure 9.2b shows a simulated image of a hydrogenated z edge (hereafter named z1, with reference to the number of H atoms bound to each terminal C atom). The resemblance with the experimental image is now evident. Even more striking is the effect of the hydrogenation on the k edge. Here the presence of the H atoms not only breaks the bonds with the metal, but also forces the protruding C atoms to bend towards each other into couples forming closed pentagons, thus turning the clean k into a hydrogenated rk (hereafter rk1) edge. Again, the simulated STM image of such structure is in remarkable agreement with the experimental one (compare central and left column in Figure 9.2d). To further support our identification of hydrogenated edges at RT, we want to highlight that combining the available information about H_2 dissociative adsorption on Ni(111) with the results of our simulations for the edge hydrogenation by means of the resulting adsorbed H atoms, we deduce that the overall hydrogenation process of the graphene/Ni(111) edge is exothermic and

practically barrierless: an energy gain of more than 1 eV/terminal C atom with respect to the molecule impinging from the gas phase is found, more precisely 1.17 (1.09) eV/terminal C atom for z (k) edges (see Figure 9.5). It is worth to point out that the hydrogenation process of the edges is favored despite the breaking of the covalent bonds with the substrate acts in the opposite direction, requiring an energy cost. For comparison, the hydrogenation of the z and rk edges in free-standing graphene (where k is not stable) would give a DFT energy gain more than twice as large as in case of adsorption on Ni(111): precisely, 2.65 (2.67) eV/terminal C atom for z (rk) edges, respectively.
In Figure 9.3 we also show the density of states projected onto the atoms relevant to the edge, i.e., onto the terminal edge C atoms (named edge C in figure) and the closest surface Ni atoms (edge Ni). For comparison, the projections onto the C atoms in fcc-hollow site (C fcc-h) and the surface Ni atoms far from the edge (Ni) are also shown, corresponding to the infinite graphene layer. While in the hydrogen passivated edge (z1 and rk1) only small differences are visible for the terminal C atoms with respect to the infinite layer case, a large variation can be observed in the z and k edges, due to the substrate passivation and in particular to the stronger hybridization with the Ni electronic d-states. DFT predicts also other stable hydrogenated configurations with a different number of H atoms, whose presence is however excluded when comparing their simulated STM images with experimental ones.
Since H_2 is always present, typically as the most abundant component of the residual atmosphere in all growth chambers, this hydrogenation process is highly probable. Furthermore, the possible existence of hydrogenated graphene edges for CVD graphene in UHV conditions was previously suggested also on the Ir(111) surface.[131] H is strongly bound to the edge C atoms: we imaged the islands at different temperatures in the 25-300 °C range after hydrogenation, and they never changed their appearance, always exhibiting a sharp profile and a clear z1 and rk1 geometry. This is in good agreement with the stability of the CH groups at the edges of graphene islands on metal substrates[145] and with the barrier of at least 1 eV predicted by DFT for the dehydrogenation process (right to left in Figure 9.5). Upon heating to T>300 °C, experiments indicate that the growth process is restored and a complete graphene layer forms. At such temperature, the dehydrogenation barriers predicted by DFT can be overcome: the C-H bonds break and H_2 molecules form and desorb. Therefore, although the energetics would be unfavorable in presence of hydrogen, upon heating hydrogen is removed and the edge passivation occurs again through the substrate. Finally, we underline that we investigated the edge structure also during and after growth under hydrocarbon exposure, finding results similar to those presented above, as expected on the basis of our calculations of the ground-state structures with and without hydrogen at the edges.

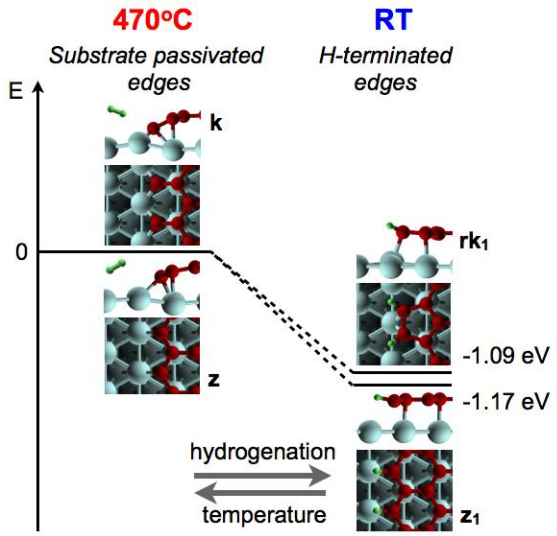

Figure 9.5: DFT energy diagram of the most favored configurations of graphene edges on Ni(111) upon hydrogenation and dehydrogenation. The dashed lines do not indicate the details of possible hydrogenation/dehydrogenation paths but are just a guide to join z with z1 and k with rk1. Zero energy corresponds to the substrate passivated configurations and H_2 molecules in gas phase; precisely, one molecule for each pair of terminal C atoms of the edge is considered in order to keep the same stoichiometry of the corresponding single-hydrogen passivated configuration; the energy values are reported here per terminal C atom.

9.3 Summary

In conclusion, we demonstrated that temperature acts as a control parameter driving the structure of graphene/Ni(111) edges by changing their passivation. When graphene forms above a Ni(111) substrate (i.e. at T > 300 °C), during the growth process its edges are clean and anchored to the metal substrate, as predicted by Zhang et al.[141] Growing graphene flakes are thus sealed, most probably thereby hindering the penetration of ad-species below the flake. Upon cooling to RT, the growth is stopped and supported graphene flakes result. The edges of the flakes are now hydrogenated via dissociation of H_2 molecules from the residual background gas pressure. If the growth is carried out under C_2H_4 exposure, residual hydrogen or radicals from hydrocarbon dissociation could also contribute to this process. At RT the flake edges are detached from the substrate, thus potentially favoring the intercalation of other species below graphene. The hydrogenated structure is highly stable upon heating, until the growth process is restored at T > 300 °C; hydrogen effects have therefore to be taken into account when considering possible applications of graphene flakes on Ni substrates. This mechanism to trap and release hydrogen can in part be respons-

ible for the enhanced hydrogen storage capability in carbon-based nanocomposites, [149,150] making sp^2-type edges in direct contact with metals an active site for hydrogen storage at low pressure.

Chapter 10

Edge growth mechanisms

After having clarified the atomic structure of graphene edges (see Chapter 9), in this Chapter, we move one step further, studying in more detail one of the growth mechanisms presented in Chapter 8. To this purpose we take advantage of the high-speed STM capability provided by the FAST module (described in Chapter 3). These measurements allow us to identify the active sites for C attachment during growth, revealing the role of Ni adatoms.

10.1 State of the art

During the CVD process, the role of the catalyst is not limited just to hydrocarbon dissociation. In particular, the presence of the metal surface improves also the graphene quality, opening new growth and defect healing pathways.[151] A possible important role of adatoms coming from the substrate was recently suggested by DFT calculations.[140] This kind of under-coordinated atoms, as well as those located at the edges and corners of nanoparticles, typically show an enhancement in their chemical activity, due to a characteristic upshift of the d-band center.[152] Indeed, it is well known that metal adatoms are involved in several processes occurring on surfaces and at the solid-liquid interfaces, such as catalytic reactions,[153,154] surface reconstructions,[155] and self assembly of organic molecules.[156–158] Single atoms have been recently shown to facilitate addition and removal of C atoms from the edges of a suspended graphene flake by means of high-resolution transmission electron microscope (HRTEM) measurements.[159,160]

Nevertheless, the presence of a metal substrate has been shown also to peculiarly dictate the structure of graphene edges,[112,131,143] which play an important role in the growth processes, providing the active sites for the attachment of new atoms. Although experimental results have been achieved in the understanding of graphene growth mechanisms at the nano- and micro-scale,[94,96,108,109] little is known on the elementary steps involved in the pathway of C addition, mainly due to technical limitations in observing supported growing edges with suffi-

cient spatial and temporal resolution.

10.2 Results and discussion

10.2.1 Growth mechanisms

EG has been synthetized on Ni(111) by C segregation in a temperature range between 430 and 470 °C, in order to obtain islands on a clean Ni surface,[94] with an average growing velocity of about 0.1 nm/s. Under these conditions, by standard STM imaging, the graphene edges appear blurred, since the image acquisition time (~30-40 s/frame) is too high to resolve the rapidly evolving atomic structure. To overcome this problem, we used the FAST module[45] (described in Chapter 3), which allows acquiring STM time series up to 100 frames/s. Indeed, as shown in Chapter 9, an image acquisition rate of 4 Hz is enough to clearly distinguish the atomic structure of growing graphene edges. Here we studied the edge growth processes, using the FAST module operating around video-rate, further improving the time resolution, in the attempt to resolve details of the C addition process.
The model in Figure 10.1 shows some possible edge structures of a free-standing graphene flake: zigzag (z), Klein (k) and armchair (AC). In particular, z and k have been identified as the edge terminations of EG islands on Ni(111) at temperatures higher than ~300 °C (see Chapter 9).[112] In Figure 10.1, along the z and k

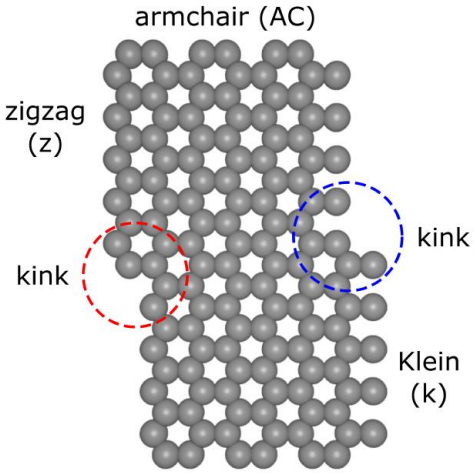

Figure 10.1: Edge and kink structures of a graphene flake.

edges, the last two C rows are removed for half of their length, leading to the formation of kink sites, which have been predicted to play an important role in graphene edge expansion.[139,140]
Figure 10.2 shows consecutive frames acquired along (a) z and (b) k edges, with a frame rate of 36.5 and 60 Hz, respectively. These prototypical time-series have

been chosen for their high both spatial and temporal resolution. In particular, they are long enough for a statistically relevant analysis. Other sequences acquired at lower frame rate (10 Hz) have been obtained on both the edge configurations, without showing any qualitative differences, suggesting a negligible effect of the fast scanning tip on the observed processes. This effect could be ascribed to the small tip-surface interaction time ($\simeq 1.5-2.5\ \mu s$/pixel).
Based on the results shown in Chapter 9, the edge structure in Figure 10.2a is identified as z and presents a kink site in the middle. Looking at the sequence, the first evidence is that the growth proceeds in an ordered way at the kink only, causing it to propagate along the straight edge. This is in agreement with previous DFT calculations, showing that a kink structure along the z edge leads to the formation of an AC-like site, which has a lower energy barriers for C addition. [140] During the z edge growth, the kink structure appearance is equivalent to the initial one, likely due to the preference of hollow-site edge termination, as confirmed by DFT calculations. [112]
Figure 10.2b shows a STM time-series acquired on a k edge with an acquisition time of ≃17 ms/frame. Along this edge, the growth mechanism appears to be very similar to the one described for the z edge, proceeding at the kink site. The main difference is the presence of a C atom in top position at the kink (see the first stick-and-ball model in Figure 10.2b). Despite the general preference for hollow termination, [112] preliminary DFT calculations show that this configuration is a stable minimum, with an energy gain of 0.54 eV, compared to the situation where the C atom is far from the edge.
A closer look at the time-series in Figure 10.2 reveals on both edges the presence of bright objects that appear and disappear at the kink site. Indeed, a bright feature is present in some frames (frames at 27 and 82 ms in Figure 10.2a, and frames at 17 and 50 ms in Figure 10.2b), while it is absent in others (see the frames at 0 and 55 ms in Figure 10.2a, and frames at 0 and 33 ms in Figure 10.2b). These objects are imaged nearby the kink sites typically for few scan lines, indicating a short residence time (∼1-2 ms, see below). More interestingly, their presence seems to be correlated to C attachment events, suggesting a possible catalytic behavior. Indeed, the appearance of the bright feature is usually followed (or accompanied) by C dimers attachment at the kink site (see frame at 55 ms in Figure 10.2a, and frames at 17, 33 and 50 ms in Figure 10.2b).
Concerning the nature of these objects, in Chapter 8, we have shown that under low temperature CVD conditions on Ni(111) (T = 400-500 °C), graphene presents a considerable number of point-like defects, that have been identified as substitutional Ni atoms, trapped into the graphene network during the growth process, as will be further confirmed in Chapter 11. Comparing the apparent height of these defective sites, with the one of the bright features observed at the kink site, we can conclude that the latter are likely mobile Ni adatoms. This assumption is also supported by the well-known presence of diffusing adatoms on metal surfaces above RT. [161–164] Other dashed features are evident in some frames, but due to their low apparent height (comparable or lower than the graphene one),

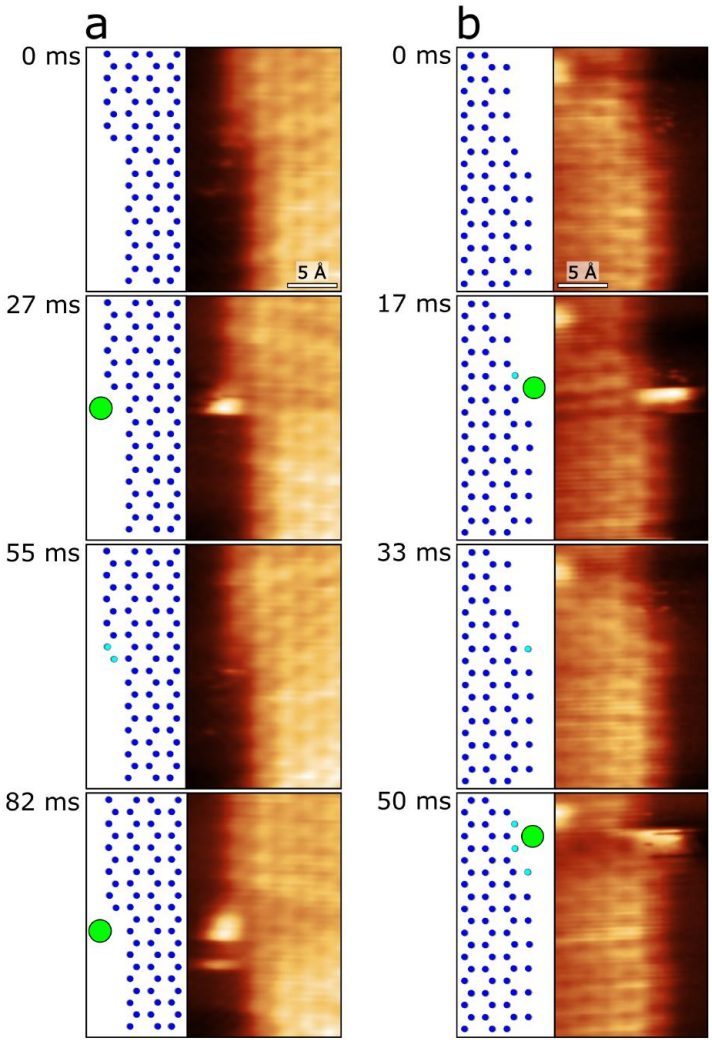

Figure 10.2: Growth mechanisms along z and k edges. FAST sequences acquired at 440 °C: (a) z edge [V = 20 mV; I = 4 nA; 36.5 Hz], (b) k edge [V = 20 mV; I = 3.5 nA; 60 Hz]. In the schematic models, blue, light-blue and green balls represent C in graphene, C in graphene attached during the last growth step and the Ni adatom, respectively.

it is hard to discriminate between Ni imaged by the tip in an off-center position,[49] and C atoms. In order to avoid identification mistakes, in this work we considered as Ni adatoms only the feature higher than the graphene layer.
From the time-series acquired in Figure 10.2, it is possible to note that the Ni adatom attaching/detaching events occur mainly at the kink sites, indeed, almost no bright dashes are visible on the straight part of the edge. This observation suggests that the adsorption of Ni adatom on a kink site is an energy minimum,

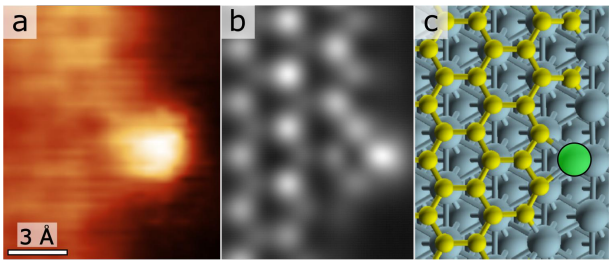

Figure 10.3: Ni adatom adsorption geometry at the k edge kink. (a) STM image [V = 20 mV; I = 3.5 nA], (b) constant height simulated image, and (c) stick-and-ball model of the calculated geometry. In (c), the Ni adatom is highlighted in green.

as also confirmed by our DFT calculations, but the short residence time evidences that the bond can be easily broken at this temperatures, avoiding the poisoning of the active kink site. Indeed, no Ni trapping event has been observed in our movies, ruling out the defect formation pathway suggested by Wang et al. [165] Nevertheless, the formation of defects, where the Ni adatom is trapped, has been observed in the case of two counter-propagating kink along the same edge.
Concerning the atomic configuration of the Ni adatom at the kink, Figure 10.3a shows a STM image where the structure has been fully resolved along the k edge. DFT calculations reveal that the attachment of a second C atom in top position is required in order to stabilize the adatom in such position. This configuration appears to be stable, with a system energy gain of about 2 eV upon Ni attachment. The corresponding constant-height simulated image and the stick-and-ball model are shown in Figure 10.3b-c. Nevertheless, further DFT calculations are on-going in order to clarify the experimental evidences reported here.
It is important to mention that not every time a Ni adatom appears at a kink site, C atoms attach (not shown), suggesting that, at least under our experimental conditions, the availability of C could be a further limiting step for the edge growth. This is not surprising, since a low C flux was chosen in those experiments, in order to reduce the growth velocity, promoting the formation of extended z and k edges.

10.2.2 Adatom residence times

Although the time resolution in Figure 10.2 is not high enough to fully resolve all the steps involved in the growth, it is still possible to get important insight on processes occurring on a very short time-scale. In particular, we can access the residence time of Ni adatoms at the kinks. Indeed, since the scanning frequency along the horizontal direction (ν_{FAST}) is very high (6.04 kHz for the sequence shown in Figure 10.2b), it is possible to track residence times down to $\simeq$150 μs (= $1/\nu_{FAST}$), which corresponds to the time required for the tip to com-

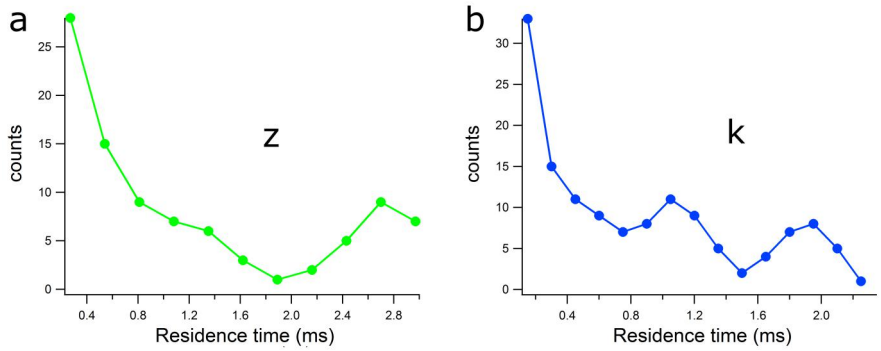

Figure 10.4: (a-b) Histograms of Ni adatoms residence time for z and k respectively. The x-scale has been obtained multiplying the number of line-scans by $1/\nu_{FAST}$.

plete a line-scan (forward or backward). Counting the number of line-scans for which the adatom is present in a frame, we obtained the graphs shown in Figure 10.4, for both z and k edges. They both present similar features: initially there is an exponential-like decay, then two distinct peaks, suggesting the presence of bound states. The second peak in Figure 10.4a has a residence time of 2.7 ms, corresponding to about 10 line-scans, that are enough to clearly identify the adsorption geometry. Unfortunately it is not possible to clearly resolve the atomic structure of the first peak, but it is likely to be another transition state of the growth mechanism with a residence time of 1.3 ms. Instead, the initial exponential decay, that has a short characteristic time ($\simeq$430 μs), can be ascribed to a weak interaction between the adatom and the kink site. For the k edge, while the initial exponential decay has a characteristic time of $\simeq$530 μs, both peaks indicate residence times shorter than the ones along z, corresponding to 1.1 and 1.9 ms respectively. The latter corresponds to the structure shown in Figure 10.3.
At this point, questions may arise on the Ni adatom detachment mechanism from the kink, since the DFT calculated adsorption energy is quite high (~2 eV). However, the histogram in Figure 10.4b shows that the configuration observed in Figure 10.3, is not the only one involved in the C addition process, as confirmed by the peak at 1.1 ms in Figure10.4b. Even if it is not possible to recognize the corresponding atomic structure, the shorter life-time ($\simeq$1 ms) suggests a lower energy barrier for the detachment.

10.2.3 Edge dependent growth velocity

From our time-series, it is also possible to extract the values of the growth velocity along the edge, for both z and k edges. Counting the number of C dimers attaching to the kink in the time between two consecutive frames (n), we obtained

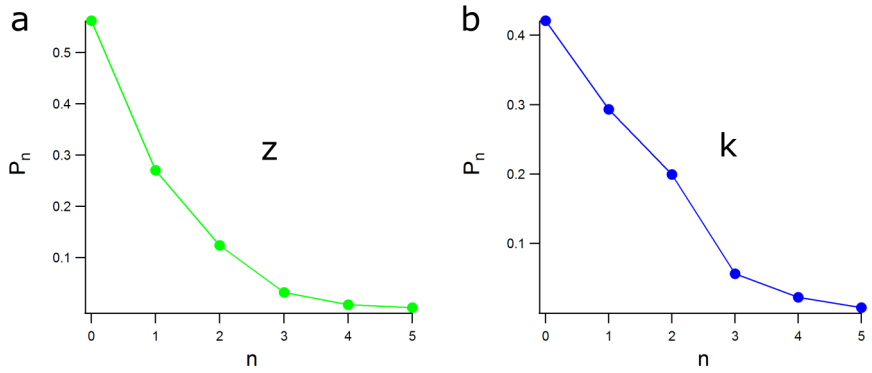

Figure 10.5: Normalized probability (P_n) of growth events involving the attachment of a number n of C dimers between consecutive frames. (a) P_n for a z edge (T = 440 °C; time between frames ≃ 54 ms). (b) P_n for a k edge (T = 440 °C; time between frames ≃ 34 ms).

the graphs in Figure 10.5, where the probability (P_n) has been normalized as:

$$\sum_{n=0}^{\infty} P_n = \sum_{n=0}^{5} P_n = 1, \tag{10.1}$$

since we never observed more that 5 dimers attaching to the edges between two images. The expectation value of n is:

$$\langle N \rangle = \sum_{n=1}^{5} n \cdot P_n \tag{10.2}$$

In order to determine the influence of the edge structures on the kink propagation speed, we can evaluate the average kink growth velocity:

$$v_{edge} = 0.5 \cdot \nu_{acq} \cdot l_{dimer} \cdot \sum_{n=1}^{5} n \cdot P_n \tag{10.3}$$

where, ν_{acq} is the FAST acquisition frame rate, l_{dimer} the distance between C dimers along the edge direction (0.249 nm). The factor 0.5 is introduced because up and down time-series have been considered separately, in order to keep the time delay between the acquisition of each considered pixel constant for all the frames. In this way, it is possible to estimate an average growth velocity along the edge of 3 nm/s for z and 7.4 nm/s for k at 440 °C. The observed dependence of the velocity on the edge atomic structure suggests different overall energy barriers for C attachment for the z and k edges.

10.2.4 Kink nucleation mechanism

The nucleation of a new row along the z edge is shown in Figure 10.6. In the first frame, it is possible to observe few dashes around the middle of the straight z

edge, suggesting the presence of a weakly bound adatom (not clearly identifiable as a Ni adatom). After 27 ms, 5 C atoms are found to be attached to the straight

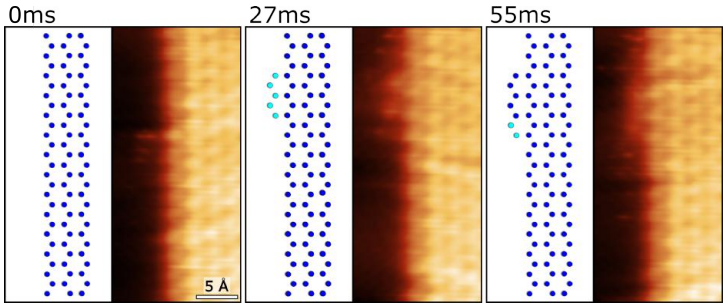

Figure 10.6: Kink nucleation along a z edge. FAST sequences acquired at 440 °C on z [V = 20 mV; I = 4 nA; 36.5 Hz]. In the schematic models, blue and light-blue balls represent C in graphene and C in graphene attached during the last growth step, respectively.

z edge, forming two new graphene rings. Then the growth proceeds as already shown in Figure 10.2 a by C attachment at the kink site. While the dynamics of C addition at the kink site is fast, the formation of the new kink is a rare event, representing the limiting step of the growth process. [140] This is in agreement with the observation of a higher growth velocity for RG islands, [39] where the active sites density is higher, due to the graphene-substrate lattice mismatch. [166]

10.3 Summary

In conclusion, we investigated for the first time the graphene edge growth mechanisms in *real time*, by means of video-rate STM measurements. During the growth process, both z and k edges present kink structures, that have been identified as the active sites for C addition. Moreover, we revealed the presence of Ni adatoms at the kink site, unraveling their role as single atom catalysts in driving the C addition. From the extended movies, it has been also possible to extract the average kink propagation velocity along the edge, for both z and k.

Chapter 11

Structural defects

This Chapter presents a study of the intrinsic defective structures of epitaxial graphene on Ni(111), carried out by means of STM measurements in combination with DFT calculations. We identify point-like defects mainly as embedded Ni atoms, revealing their atomic configurations. Then, we reveal how the transition between different graphene adsorption geometries can lead to the formation of grain boundaries and lattice distortions. Some of the results presented here have been published in the *Journal of Physical Chemistry Letters*.[65]

11.1 State of the art

Defective structures in graphene can affect the performances of electronic devices. However, this drawback can be exploited in order to tailor the local properties of graphene, adding new functionalities. Defects in 2D materials can be classified as point-like (0D), grain boundaries (1D), extended in-plane lattice distortion (2D) and out-of plane relaxations (3D).
Atomic point defects (0D) in graphene have been revealed to strongly influence transport properties.[167,168] In particular, C vacancies have been shown to induce local magnetic moments in graphite, leading to a reduction of the charge carriers' mobility.[169] However, the presence of a metallic substrate in direct contact with the graphene layer leads to the quenching of magnetic moments,[170] hindering possible applications.
Graphene doping by foreign atoms is a possible alternative in order to tailor 2D materials properties at the nanoscale. Single nitrogen atoms can be incorporated as dopants into graphene, strongly modifying its electronic structure.[171] This can be achieved adding NH_3 during the CVD process,[172] or by means of low-energy N_2 ion implantation in pristine graphene.[173,174] Moreover, metal dopants have predicted to induce a magnetic moment,[175] and to add also chemical functionalities.[176,177]
On the other hand, the in-plane transition between domains with different configurations induces the formation of different defective structures: grain bound-

aries (1D) and distortions (2D) of the C network.[178] Sharp domain boundaries lead to topological defects, characterized by non-hexagonal carbon rings, that largely affect graphene properties,[179] enhancing electron scattering.[180] Actually, when a variety of different graphene rotational domains are present, as typically occurs for CVD growth on most transition metal surfaces, the domain boundaries are complex 2D structures.[179,181] Conversely, on substrates where graphene can grow epitaxially, with only translational domains, extended 1D defects can form. Indeed, 1D extended defects have already been observed by Lahiri et al.[74] in EG on Ni(111), at sharp boundaries between top-fcc and top-hcp domains, and can be considered metallic nanowires. Topological defects of this kind deserve particular interest also in freestanding graphene for their exceptional electronic properties.[182–186]

11.2 Results and discussion

A typical STM image of EG grown on Ni(111) at 400 °C is shown in Figure 11.1. It is possible to observe a large number of point-like bright defects, present both isolated and as short chain structures, and also few dark depressions, ascribable to C vacancies, as well as extended topological defects (see below).

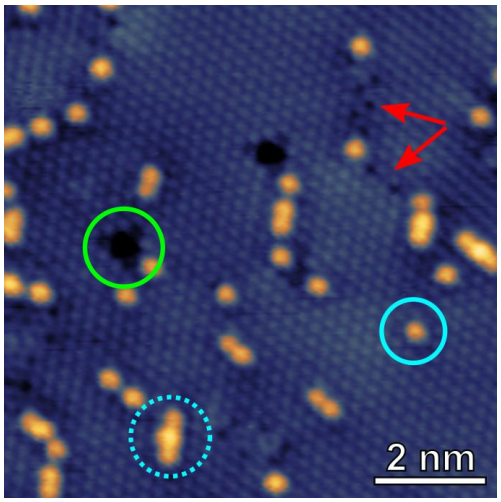

Figure 11.1: Defective epitaxial graphene on Ni(111). Representative defects are highlighted: substitutional Ni (light blue circles), C-vacancies (green circle), topological defects (red arrows) [V = -50 mV, I = 0.7 nA].

11.2.1 Point defects (0D)

In this section, we focus on the bright point-like features. Although in the STM image in Figure 11.1, showing a region of EG, the defects of this kind do not differ

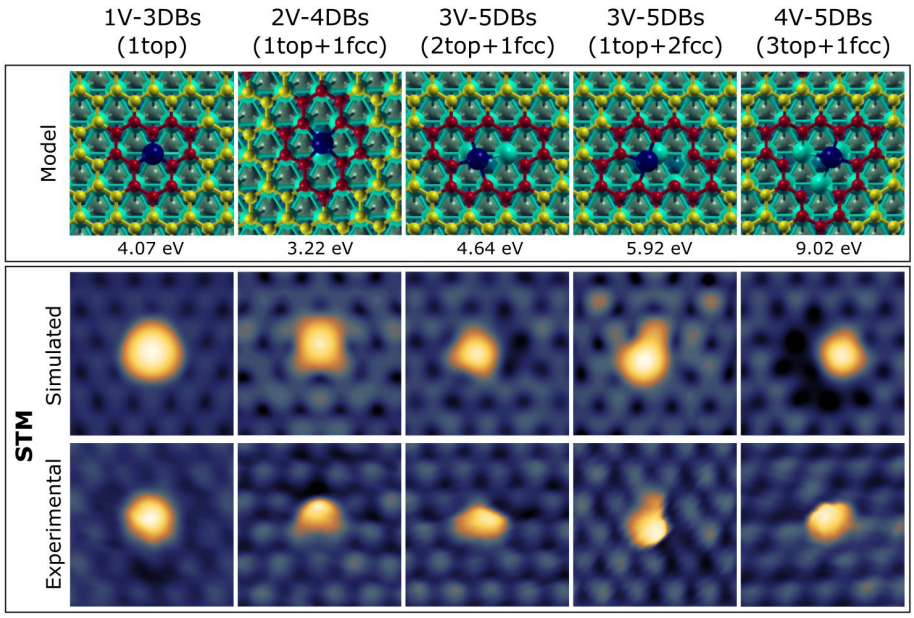

Figure 11.2: Point-defects in graphene/Ni(111). Top panel: stick-and-ball model of relaxed structures. Formation energies are indicated below each structure. Bottom panels: simulated and experimental STM images. Images size: 1.2×1.2 nm^2. The different structures are classified depending on the number of C vacancies (V), dangling bonds (DBs) and position of the missing carbons.

significantly, high-resolution STM measurements allowed recognizing different types of bright features (bottom panel, Figure 11.2), characterized by different shape and in-plane position with respect to the graphene lattice. DFT calculations reveals that these features are nicely reproduced by embedding a substitutional Ni adatoms inside the graphene lattice, finding five different configurations. The latter have been classified depending on the number and position of the C vacancies. In all the cases considered here the presence of the Ni atom induces a localized bright feature in the simulated STM image. The simulated images are shown in Figure 11.2 (middle panel), in comparison with the corresponding experimental ones (bottom panel). Simulated images (middle panel, Figure 11.2) for single (1V) and double (2V) C vacancies are in good agreement with the experimental ones. Instead, for the case of 3V and 4V, the resemblance worsens. The main difference is the appearance of the C atoms in hollow-fcc position with one dangling bond, present in the case of 3V (2 top and 1 fcc) and 4V. Indeed, while these sites appear bright in STM, in the simulations they appear dark, due to a bending toward the substrate. Attempts to improve the image matching are on-going, considering the interaction of the Ni adatom with H and the possible presence of sub-surface C atoms.

11.2.2 Grain boundaries (1D) and lattice distortions (2D)

Figure 11.3 demonstrates that the connection of top-fcc and top-hcp domains can actually occur in-plane via both the formation of 1D defects and a gradual distortion of the C network. Indeed, the defect line crossing almost vertically

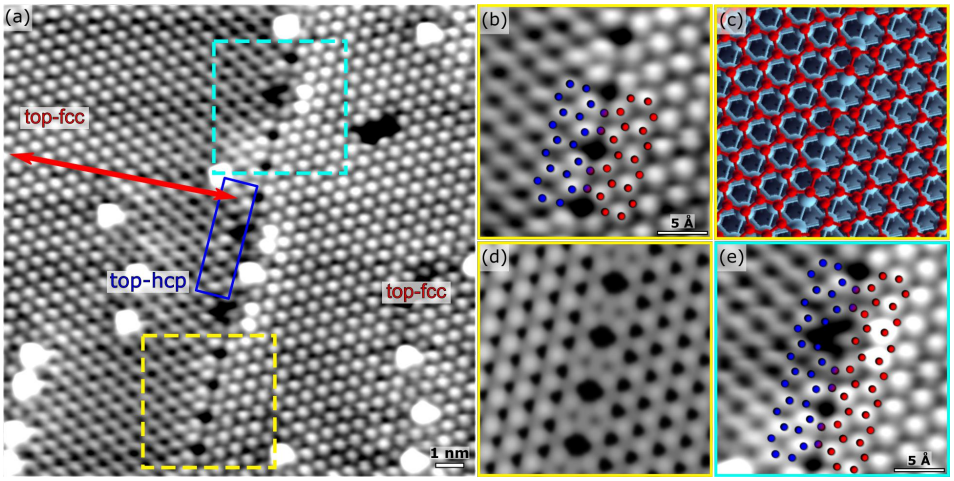

Figure 11.3: Transitions between top-fcc and top-hcp domains. (a) STM image showing both a sharp domain boundary and a smooth distortion. On the left of the sharp boundary, a thin top-hcp region (highlighted by the dark blue rectangle) extends for 2-3 nm and then stretches into top-fcc via distortion of the C-rings. On the right of the boundary, an undistorted top-fcc domain is imaged. [V = -100 mV, I = 30 nA] (b) Zoom on the yellow square in (a). The positions of C atoms in the top-hcp (blue dots) and top-fcc (red dots) domains close to the boundary are highlighted. (c) Stick-and-ball model of the relaxed boundary. (d) Simulated constant current STM image. (e) Zoom on the light blue square in (a), highlighting the position of a C vacancy at the boundary in the top-hcp domain.

in the middle the image in Figure 11.3a is a sharp boundary: on the right we recognize top-fcc graphene; proceeding towards left, immediately passed the boundary, top-hcp in a very thin stripe (its STM contrast has been shown in Chapter 6), then a region of distorted graphene, where complete carbon rings are visible, and finally another top-fcc domain are imaged. The sharp boundary appears as an extended defect with a quite regular structure. The zoom in Figure 11.3b shows the boundary at the atomic scale. The resemblance with the structure already observed by Lahiri et al.[74] is remarkable. We studied the atomic scale structure of the sharp boundary by DFT. The model for top-hcp/top-fcc is shown in Figure 11.3c. The position of carbon atoms has been obtained by relaxing the structure, starting from that derived from the experimental image in Figure 11.3b. Although in our calculations the description of the two different domains is limited by the small size of the simulation cell (which causes a small fictitious distortion of the graphene layer), the simulated image in Fig-

ure 11.3d shows a remarkable resemblance with the experimental one, strongly supporting the validity of the structural model. The few dark features interrupting the domain boundary in the experimental image (Figure11.3e) are C vacancies in hcp position on the top-hcp side, located where the pentagons-octagon regular arrangement along the extended defect gets out of phase (see Figure 11.3e). On the left side of the boundary, the top-hcp structure after two-three unit cells starts compressing along the direction of two parallel C-C bonds of the graphenic hexagon, as indicated by the arrow in Figure 11.3a, and in ~4 nm (corresponding to 8 graphene rings), with an average normal strain of ~3.5%, transforms into top-fcc geometry. This relaxation is profoundly different from the alternative transition behavior observed by Lahiri et al.[74], interpreted as a local detaching of graphene from the Ni(111) substrate.
Figure 11.4 shows three co-exisisting domains. In Figure 11.4a (top and bottom left corner), the triangular arrangement of protrusions suggests the presence of either top-fcc or top-hcp. Unfortunately, in this case a slight asymmetry in the scanning tip prevents us from imaging dark shadows between bright spots and thus to unambiguously discriminate between the two at a first glance, while the third domain (bottom-right) has clearly the appearance of the top-bridge configuration. The coexistence of different configurations in the same image, however, helps us to identify the adsorption geometries. Indeed, on the basis of the known position of C atoms in the top-bridge domain, in Figure 11.4b, we can draw a grid joining the Ni atoms. As shown in Chapter 6, the position of the bright protrusion with respect to neighboring Ni atoms allows for a safe identification of the different graphene configurations, as top-fcc (top of the image) and top-hcp (bottom left corner). Again, the transition between different domains follows two distinct routes: while between top-bridge and top-hcp there is a sharp boundary, the transition between top-bridge and top-fcc occurs smoothly via a distortion of the carbon network. The zoom in Figure 11.4c allows us to propose a tentative structure for the sharp boundary. We marked the position of the carbon atoms starting from the known atomic arrangement and extended the structure up to the boundary to have a guess of the atomic positions. The boundary seems to be formed by eptagon-pentagon pairs with alternate orientation, forming a chain of Stone-Wales defects. The model for the corresponding DFT investigation of the top-hcp/top-bridge boundary is described in Figure 11.4d. Analogously with the model for the top-hcp/top-fcc boundary, the carbon atoms have been initially positioned as suggested by the experimental image of Figure 11.4c and then relaxed. The simulated STM image reported in Figure 11.4e shows the main features of the experimental one, although the agreement is not perfect. Discrepancies may be related to the asymmetric tip shape (see above) or to the limited size of our model, which cannot completely catch the progressive distortion of the top-bridge domain approaching the boundary. From the top-bridge domain, the C network converts within a narrow transition region to the top-fcc configuration without the formation of any topological defect. The smooth transition occurs via distortion of the graph-

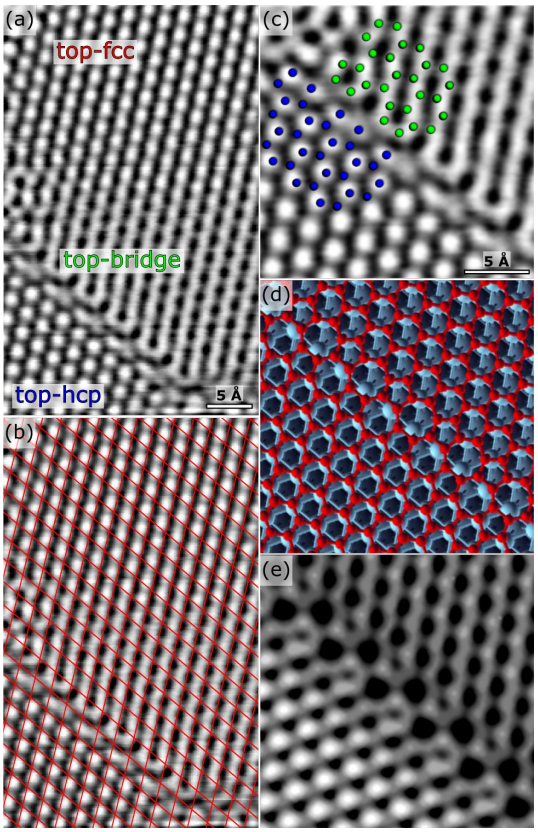

Figure 11.4: Transition between top-hcp and top-bridge and between top-bridge and top-fcc domains. (a) STM image showing three co-exisisting domains: top-fcc (top), top-bridge (center/ bottom-right) and top-hcp (bottom-left). A sharp domain boundary joins the top-hcp and top-bridge regions, while the latter converts into a top-fcc flake towards the top of the image, with a distortion of the C network. (b) A grid intersecting the Ni on top positions is drawn on (a). (c) Zoom on the sharp domain boundary between top-hcp and top-bridge regions. Green and blue dots indicate the positions of C atoms [V=-10 mV, I=25 nA]. (d) Stick-and-ball model of the relaxed boundary and (e) corresponding simulated STM image at constant current.

ene rings in a region ~2 nm wide, due to a shear strain in the C-network of about 1°.

11.3 Summary

In conclusion, defective structures in EG grown by CVD on Ni(111) have been studied by means of high-resolution STM in combination with DFT calculations. We showed the possibility to incorporate metal atoms into graphene during the

CVD process. In this way, different structures have been found, depending on the number of C vacancies and trapped Ni atoms. Finally, we evidenced that the transition between the different structures can occur both sharply, via 1D domain boundaries, and smoothly, via a gradual in-plane compression or distortion of the graphene rings (2D).

Chapter 12

Bilayer growth and properties

In Chapter 7, we have shown how to obtain different graphene configurations, revealing the possibility to tune the graphene electronic properties by decoupling from the Ni substrate through the controlled formation/dissolution of a carbide layer. Here we monitor the bi-layer formation by means of cathode lens spectro-microscopy, revealing how the growth is limited to the RG regions only. μ-ARPES measurements sheds light on the electronic properties of the BLG top layer.

12.1 State of the art

Despite the unique properties of single layer graphene, its exploitation in the field of nano-electronics is hindered by the lack of a proper band-gap. Indeed, since the Dirac cones touch at the Fermi level, free-standing graphene behaves like a metal, whereas for the fabrication of transistors and logic units, an electronic band gap is required in order to obtain high values of on/off ratio.[187] Different strategies have been recently proposed to open band-gaps in graphene-based materials, such as chemical functionalization,[188] and nano-scale patterning.[27] Alternatively, the usage of BLG allows the realization of a widely tunable electronic bandgap in electrically gated devices.[189] Moreover, in BLG the band-gap depends on the twist angle between the layers.[190] Even if initially BLG samples have been grown on SiC,[191] recently their synthesis have been successfully reported also by CVD on metal surfaces,[39,40,192,193] opening a low-cost possibility for large-scale production. Despite these progresses, at the moment a precise control on the number of layers and on their stacking still remains challenging, leading to scarce sample uniformity and multi-layer formation.[194,195]

12.2 Results and discussion

Figure 12.1a shows a BF-LEEM image of a graphene layer composed of the three different phases presented in Chapter 7. The surface has been synthetized on

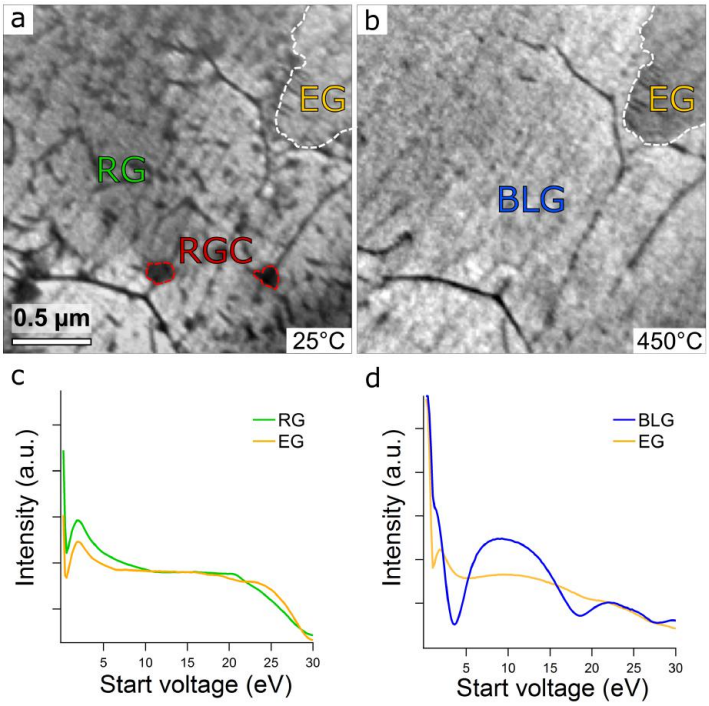

Figure 12.1: BLG growth and identification: (a) BF-LEEM image showing co-existing graphene phases acquired at RT (a) and at 450 °C (b) [V_{start} = 10 V]. LEEM I-V acquired on the region initially covered by RG, before (c) and after annealing (d) the surface at 450 °C.

clean Ni(111) by exposing the sample to C_2H_4 (p = 3×10^{-6} mbar) at 550 °C and then cooling down to RT. The presence of small patches of RGC has been ascribed to C precipitation effects,[94] leading to Ni_2C formation when cooling from growth temperature underneath RG only, due to the different interaction with the underlying substrate, with respect to EG. While annealing to ~350 °C results in the complete dissolution of the carbide layer, leaving RG in direct contact with the Ni substrate,[66] heating to higher temperatures leads to further important changes in the morphology of rotated flakes. Figure 12.1b shows the same region of the surface at ~450 °C: whereas RGC disappeared, the RG region exhibits an higher reflectivity (at V_{start} = 10 V), compared to the EG. In order to understand the origin of this reflectivity change, we compared LEEM I-V measurements acquired before and during the annealing (see Figure 12.1c-d). While the EG region presents a similar I-V curve in both cases (compatible with the one shown in Chapter 7), the one acquired at 450 °C on the RG-covered region exhibits two dips at ~4 and 18 V and a higher reflectivity in between. These peculiar features have been shown to be a benchmark of the formation of a second graphene layer.[39,196] Moreover, the formation of BLG on thin Ni(111) films, upon cooling to RT, has been previously reported in literature.[39]

The electronic properties have been probed by means of μ-XPS measurements.

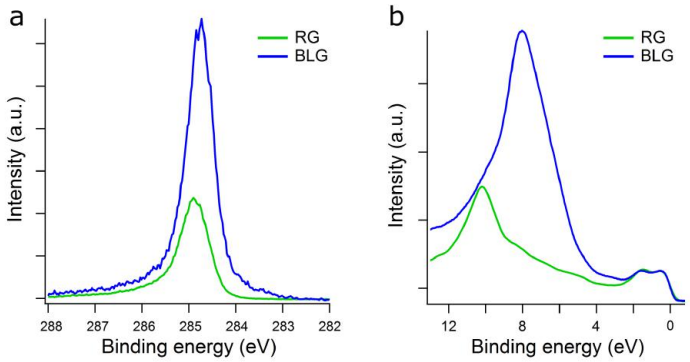

Figure 12.2: (a) μ-XPS spectra of RG (green) and BLG (blue) [$h\nu$ = 400 eV]. (b) μ-UPS spectra of RG (green, RT) and BLG (blue, 450 °C) [$h\nu$ = 40 eV]. In (a) the spectra are normalized to the Ni 3p peak intensities.

Figure 12.2a shows the C 1s spectra acquired on RG (green) and BLG (blue). The latter is slightly shifted (~0.15 eV) towards lower binding energies, suggesting a weaker interaction with the substrate. Moreover, the intensity ratio clearly indicates the presence of an additional graphene layer. Further valuable information come from the μ-UPS (Figure 12.2b), since the position of the π band strongly depends on the the orbital hybridization of graphene with its support. From the comparison shown in Figure 12.2b, a large difference in the binding energy of RG and BLG peaks is evident: while the first has a main component at ~10 eV, the latter presents a pronunced feature at ~8 eV, indicating a weak interaction between the graphene layers.[197] Furthermore, the graphene π band/Ni 3d intensity ratio is higher on BLG (9.2 vs. 3.8), compatible with the presence of an additional graphene layer.
An important point that needs to be clarified is the relative orientation between the graphene layers. A previous study revealed the formation of BLG underneath RG flakes on Ni(111), without giving direct proofs of the stacking relation.[39] Recently, Iwasaki et al.[198] proposed a BLG two-step growth process, where the first layer grows epitaxially at high temperatures and the second nucleates underneath during cooling, being rotated with respect to the substrate, due to a reduced C mobility. Our *in situ* measurements rule out this mechanism, clearly showing that the segregation of further C structures underneath graphene is hindered on the EG flakes (see Figure 12.1), revealing BLG formation only in the region previously covered by RG. Figure 12.3a-b shows μ-LEED patterns acquired on μm-sized RG and BLG regions. Since graphene and Ni(111) have almost the same lattice parameter, it is not straightforward to assign the origin of the hexagonal superlattice pattern to a twist between the layers or to a rotation of both the graphene layers with respect to the substrate. Nevertheless, Nie et al.[192] proposed a method to unveil the stacking relation of graphene lay-

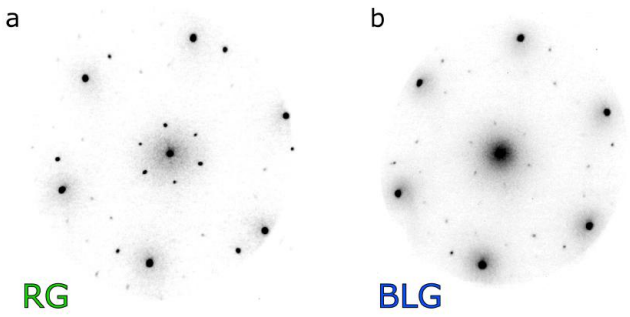

Figure 12.3: μ-LEED patterns of (a) RG [V_{start} = 55 V] and (b) BLG [V_{start} = 46 V].

ers of BLG on Ir(111), by means of LEED analysis. Indeed, while high energy electrons (~200 eV) probe several atomic layers, lowering electron energy can strongly enhance the surface sensitivity. In particular LEED patterns acquired with electron energies of ~40-50 eV are sensitive exclusively to the two top-most atomic layers, i.e., for the case of BLG, only to the two graphene layers. Following this approach, the pattern visible in Figure 12.3b suggests the presence a twisted BLG. However, for a clear assignment, further measurements are required, in order to directly prove the stacking of BLG layers.
Figure 12.4a shows the momentum distribution curve (MDC) through one of the K points along a plane normal to Γ-K, acquired on an extended BLG region, by means of microprobe angle-resolved photoelectron spectroscopy (μ-ARPES). The graphene π-band shows a linear dispersion and crosses around E_F, indicat-

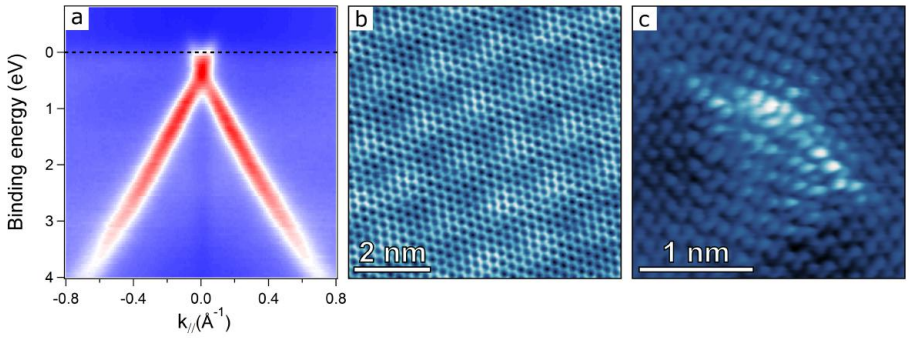

Figure 12.4: (a) μ-ARPES momentum distribution curves acquired at 450 °C [$h\nu$ = 40 eV]. (b-c) High-resolution STM images acquired at RT, showing (b) the superlattice periodicity [V= 500 mV, I = 0.3 nA] and (c) a point defect [V = -10 mV, I = 15 nA].

ing that the graphene bottom-layer efficently screens the effect of the Ni substrate, as reported for BLG/Ru(0001).[87] At the same time, the observed band

structure slightly deviates from the free-standing graphene one. Indeed, the lower cone appears to be down-shifted in energy of about 0.4 eV, and, close to E_F, it is possible to distinguish features arising from the upper cone. Surprisingly, no replicas of the π-bands are present in the MDC of Figure 12.4a. These features have been observed for graphene on SiC(0001), due to final state diffraction by a $(6\sqrt{3}\times 6\sqrt{3})$ R30° reconstructed interfacial layer.[25,199] This discrepancy calls for a deeper investigation of the electronic dispersion of BLG on Ni(111).
While the overall band down-shift can be ascribed to a doping of the graphene top-layer, questions arise on a possible small band-gap opening (<150 meV). Indeed, the periodic potential modulation, evident from the high-resolution STM image in Figure 12.4b, has been predicted to open a band-gap in single-layer graphene.[188,200] Despite this interesting possibility, the limited energy resolution of our measurements hinders from giving a clear evidence of a band-gap presence.
A point defect in the top BLG layer is shown in Figure 12.4c, revealing a broad protrusion and a complex pattern on the surrounding graphene region, due to the backscattering of electron wave functions at individual point defects, as reported for ion-irradiared HOPG.[201] This evidence further proofs the free-standing character of the BLG top layer.

12.3 Summary

In summary, we investigated the formation of BLG on Ni(111) combining scanning probe microscopy and spectro-microscopy techniques. We revealed the possibility to exploit the lattice match between graphene and Ni(111) to steer the formation of an additional Gr layer underneath the RG regions only. This approach allows decoupling the graphene top layer from the substrate, providing an interesting platform to study fundamental properties of graphene-based systems.

Chapter 13

Conclusions and outlook

In this thesis, we provided a complete characterization of the graphene/Ni(111) system, investigating morphologies and electronic properties, from the nano to the meso-scale, and following the growth process, with a time resolution down to few ms. This has been possible through an *in situ* and *in operando* approach, combining STM, XPS and cathode-lens spectro-microscopy, with *ab-initio* calculations.

In Chapter 6, we investigated the different possible graphene adsorption structures. First, the coexistence of three chemisorbed EG geometries (top-fcc, top-hcp and top-bridge) was revealed by means of high-resolution STM measurements and DFT calculations, finding top-fcc as the statistically most abundant configuration. Then, also rotated graphene domains were described. A statistical analysis of the related LEED patterns unveiled preferential orientations of the graphene flakes with respect to the underlying substrate. We reported also the formation of Ni carbide patches upon cooling to RT underneath RG regions only, ascribing this phenomenon to a different interaction with the substrate.
Once described the morphology of all the observed graphene phases, we presented in Chapter 7 their detailed spectroscopic characterization. This approach revealed similar electronic structures for EG and RG, despite the different match with the Ni substrate. Conversely, the presence of the carbide layer underneath RG, acting as a buffer layer, efficiently restores graphene semi-metal nature. Controlling the formation/dissolution of the carbide layer under RG domains, by changing the sample temperature, we devised a strategy to tune the graphene-metal coupling.
Based on these findings, which provided specific fingerprints for the identification of each graphene structure, in Chapter 8 we applied *in situ* STM and XPS for the investigation of the CVD graphene growth mechanisms. In a temperature range between 400 and 500 °C and upon ethylene exposure, we initially observed the formation of a Ni_2C surface layer, which is gradually converted into epitaxial graphene, via two different mechanisms. Conversely, above 500

°C the surface carbide coverage is strongly reduced, with graphene growing directly on Ni terraces by a replacement mechanism, which yields both epitaxial and rotated graphene domains. Furthermore, we observed that the dominant graphene growth mechanism critically depends also on the near-surface carbon concentration. Indeed, for a C contaminated subsurface, as soon as the temperature is increased, before hydrocarbon exposure, graphene seeds nucleate on the Ni surface and expand, fed by C atoms from the subsurface reservoir, leading to the formation of a complete, mainly epitaxial monolayer over the whole temperature range.
In order to unveil the details of the latter growth process, in Chapter 9, we investigated the edge structure of EG islands, both during growth and after cooling down to RT. First, we clarified how the presence of the Ni(111) substrate breaks the symmetry of the graphene edges. Then, by means of high-speed STM, we investigated the edge structure during growth, identifying z and k configurations. Atom-resolved images acquired after cooling to RT, revealed major changes in the edges appearance. This fact has been interpreted as the result of different edge passivations: while during growth the edges are passivated by the substrate, as revealed by the structural bending, upon cooling to RT the terminal C atoms are hydrogenated. The presence of hydrogen not only breaks the bond of C atoms with the substrate, but also induces a reconstruction along the k edge.
Then, after having identified the edge terminations during the growth process, in Chapter 10 we moved one step further, exploiting the video-rate STM capability of the FAST module to investigate the mechanisms of C attachment. The most striking feature is that the growth proceeds via the propagation of well-defined kink structures. Interestingly, we revealed a correlation between carbon attachment events and the presence of Ni adatoms at the kink site, highlighting their important catalytic role. From extended time-series, an important difference between z and k in the average kink propagation velocity along the edge has been found. This observation pointed out a different overall energy barrier for C attachment in the two edge configurations, which might play an important role in shaping graphene islands.
In Chapter 11, we studied intrinsic defects in EG, by means of high-resolution STM and DFT calculations. This approach allowed identifying several defective structures. While the strong C-Ni interaction drives the trapping of Ni adatoms inside the graphene network during the growth, resulting in the formation of stable structures characterized by substitutional Ni (0D), the co-existence of different graphene adsorption geometries, discussed in Chapter 6, leads to grain boundaries (1D), or to gradual in-plane compression or distortion of the graphene rings (2D).
Finally, in Chapter, 12, we addressed questions regarding the formation of multilayer graphene. In particular, the growth and the electronic properties of bi-layer graphene (BLG) were investigated, showing how the formation of the second layer occurs underneath the RG regions only, similarly to what has been reported in Chapter 7 for Ni_2C precipitation. Band structure mapping revealed the free-

standing character of the BLG top layer. Despite our LEED and STM measurements suggest a twist between the two graphene layers, further measurements are required in order to directly prove the stacking of the BLG layers.

In conclusion, the work presented in this thesis allowed us to correlate CVD parameters, easily controllable during the synthesis process, with the formation on the model Ni(111) surface of graphene layers where grains with specific properties dominate (e.g. aligned/rotated, coupled/decoupled, MLG/BLG). This represents an important step towards a deeper knowledge of technologically relevant surface processes, such as CVD graphene growth on Ni surfaces. In order to extend the relevance of this work, attempts to bridge the so-called material gap are first of all required. Preliminary studies on poly-crystalline foils have already shown how most of the results obtained so far are important also for substrates commonly used for the industrial production. Another limitation commonly considered when transferring results from model to real systems is the so-called pressure gap. Actually, the experimental conditions used in our studies of the growth process are not far from the ones employed in LP-CVD (i.e. $\sim 10^{-5}$ mbar), allowing to extend the knowledge to real systems without major concerns. However, another important aspect needs to be consider, that is the environment-induced effect on the as-grown CVD graphene layer. To verify the impact of the exposure of CVD graphene to high pressure of gases (e.g. CO, H_2O, O_2, etc...), thus trying to shed light on environmental issues, a high pressure cell has been recently integrated into the STM setup, offering the possibility to expose the sample to a controlled gaseous environment up to 1 bar and, then, to characterize the surface with STM.

Part III

Appendix

Appendix A

STM height analysis

Unambiguous identification of the surface morphology in STM movies was based on a careful height analysis.
The STM image in Figure A.1a shows a typical region of the surface where the top-most Nickel layer (clean on the left) has partly converted into a Ni_2C surface carbide island (on the right). As displayed in the line profile, surface carbide appears on average ~0.2 Å higher than the adjacent bare Ni(111) layer. In Figure A.1b, the line profile measures, instead, the average height of a graphene island grown on the Ni(111) substrate. Here the height is ~1.35±0.1 Å. The image in Figure A.1c has been extracted from Figure 8.2 of chapter 8 and shows the typical appearance of a carbide island that is converting in-plane to graphene. Here graphene is ~0.8 Å lower than the coexisting carbide. Since the apparent Ni step height in STM images is ~1.95±0.1 Å, the measured height difference indicates that graphene is co-planar with the surface carbide layer, as shown in the model below the profile. The sketch below the model schematically displays expected apparent heights in STM images and helps identifying the morphology.
In the image of Figure A.1d, two different graphene islands can be recognized. The first one, labeled $Gr^{(1)}$, is apparently ~0.8 Å lower then Ni_2C (profile not shown), as expected for in-plane graphene conversion. Conversely, $Gr^{(2)}$ is ~1.15 Å higher than the adjacent Ni_2C region and ~1.95 Å higher than $Gr^{(1)}$. These height differences cannot account for a physisorbed graphene flake growing above the surface carbide, which should be 1 Å higher than the measured values, as predicted by Kozlov et al. [73] Indeed, in the paper by Jacobson et al. [9], a region where graphene is overlying a carbide island appears higher than a neighboring epitaxial graphene region. The relative height measured in our images can only be explained by identifying $Gr^{(2)}$ as a graphene flake grown on an additional Ni atomic layer, as displayed in the model.
In Figure A.2a an EG region grown at 520°C is imaged. The line profile shows that the island is ~0.6 Å lower than the encompassing terrace, which can be safely identified as clean Ni as confirmed also by the fuzzy step-edge. Based on such height difference, we can assert that the graphene island is embedded into the

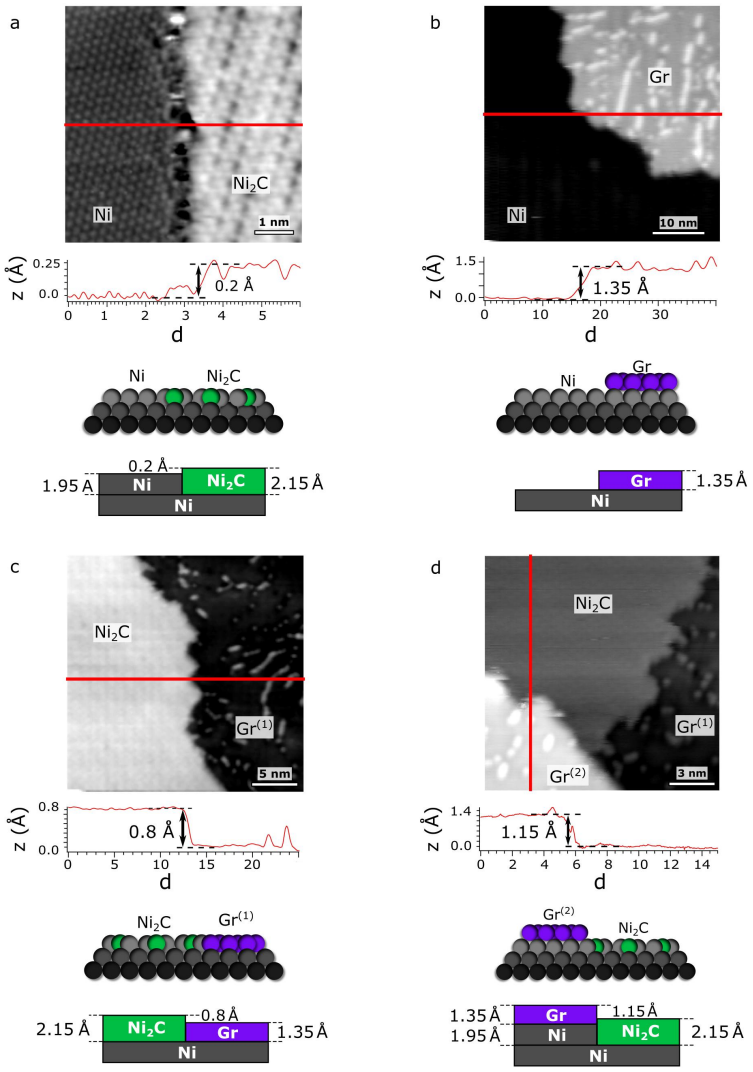

Figure A.1: Height analysis of C structures in typical STM images: (a) Ni_2C island (right) embedded in the top-nickel layer (left) [6 × 6 nm^2, V = -10 mV, I = 1 nA]; (b) graphene island (top-right) grown on a Ni(111) terrace (bottom-left) [40 × 40 nm^2, V = -600 mV, I = 0.4 nA]; (c) carbide region (left) during in-plane conversion to graphene (right). Below the line profile, model of the topography of the surface and scheme of the expected apparent height differences [25 × 25 nm^2, V = -100 mV, I = 0.1 nA]; (d) Graphene island (labeled $Gr^{(2)}$) expanding over the region previously covered by nickel carbide. Below the line profile, model of the surface at the $Gr^{(2)}$/carbide interface and related scheme of expected apparent height differences [15 × 15 nm^2, V = -250 mV, I = 0.5 nA].

Ni terrace as shown in the model and in the sketch of the related expected apparent heights. Figure A.2b presents a similar height analysis on a RG domain.

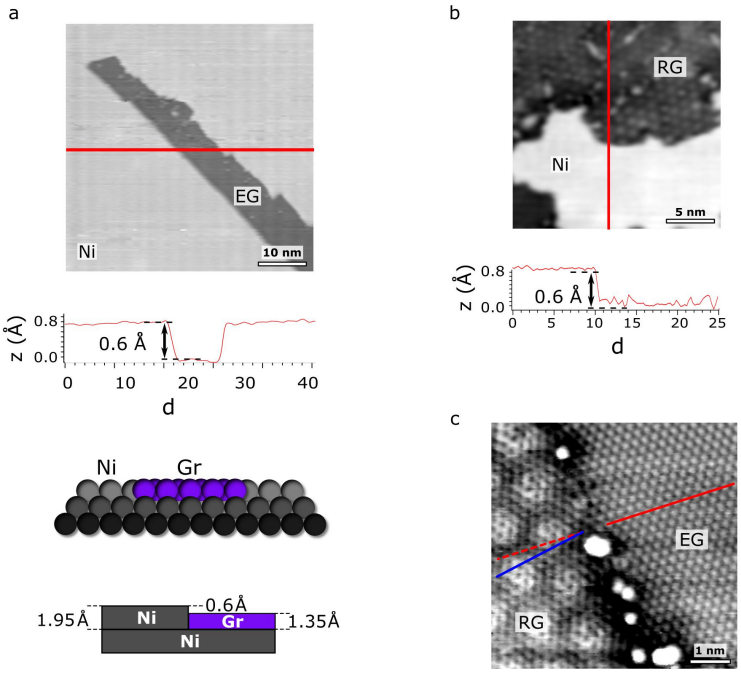

Figure A.2: Graphene growth above 500 °C: (a) height analysis of a typical embedded epitaxial graphene island imaged at 520 °C, model of the topography and sketch of the expected apparent height differences [50 × 50 nm^2, V = -500 mV, I = 0.5 nA]; (b) height analysis of an embedded moiré domain [25 × 25 nm^2, V = -800 mV, I = 0.3 nA; (c) atomic resolution image of a domain boundary proving the rotation of the graphene network in the moiré region [6 × 6 nm^2, V = -300 mV, I = 0.5 nA].

As for the island imaged in Figure A.2a, also in this case the height difference with respect to the Ni substrate indicates that RG grows embedded into the Ni top-most layer. The atomically resolved STM image in Figure A.2c evidences the lattice rotation of RG compared to EG.

Bibliography

[1] Novoselov, K. S.; Jiang, Z.; Zhang, Y.; Morozov, S.; Stormer, H.; Zeitler, U.; Maan, J.; Boebinger, G.; Kim, P.; Geim, A. *Science* **2007**, *315*, 1379–1379.

[2] Mayorov, A. S.; Gorbachev, R. V.; Morozov, S. V.; Britnell, L.; Jalil, R.; Ponomarenko, L. a.; Blake, P.; Novoselov, K. S.; Watanabe, K.; Taniguchi, T.; Geim, a. K. *Nano Letters* **2011**, *11*, 2396–2399.

[3] Lee, C.; Wei, X.; Kysar, J. W.; Hone, J. *Science* **2008**, *321*, 385–388.

[4] Balandin, A. *Nature materials* **2011**, *10*, 569–581.

[5] Novoselov, K. S.; Falko, V. I.; Colombo, L.; Gellert, P. R.; Schwab, M. G.; Kim, K. *Nature* **2012**, *490*, 192–200.

[6] Bae, S. et al. *Nature Nanotechnology* **2010**, *5*, 574–578.

[7] Weatherup, R.; Bayer, B.; Blume, R.; Ducati, C.; Baehtz, C.; Schlögl, R.; Hofmann, S. *Nano Letters* **2011**, *11*, 4154–4160.

[8] Lahiri, J.; Miller, T.; Adamska, L.; Oleynik, I. I.; Batzill, M. *Nano letters* **2011**, *11*, 518–22.

[9] Jacobson, P.; Stöger, B.; Garhofer, A.; Parkinson, G. S.; Schmid, M.; Caudillo, R.; Mittendorfer, F.; Redinger, J.; Diebold, U. *ACS Nano* **2012**, *6*, 3564–3572.

[10] Castro Neto, A. H.; Guinea, F.; Peres, N. M. R.; Novoselov, K. S.; Geim, A. K. *Reviews of Modern Physics* **2009**, *81*, 109–162.

[11] Wallace, P. *Physical Review* **1947**, *71*, 622–634.

[12] Nair, R. R.; Blake, P.; Grigorenko, A. N.; Novoselov, K. S.; Booth, T. J.; Stauber, T.; Peres, N. M. R.; Geim, A. K. *Science* **2008**, *320*, 1308.

[13] Bunch, J. S.; Verbridge, S. S. S.; Alden, J. S.; Van Der Zande, A. M.; Parpia, J. M.; Craighead, H. G.; McEuen, P. L. *Nano letters* **2008**, *8*, 2458–62.

[14] Moser, J.; Barreiro, A.; Bachtold, A. *Applied Physics Letters* **2007**, *91*, 163513.

[15] Elias, D. C.; Nair, R. R.; Mohiuddin, T. M. G.; Morozov, S. V.; Blake, P.; Halsall, M. P.; Ferrari, A. C.; Boukhvalov, D. W.; Katsnelson, M. I.; Geim, A. K.; Novoselov, K. S. *Science* **2009**, *323*, 610–613.

[16] Kuila, T.; Bose, S.; Mishra, A. K.; Khanra, P.; Kim, N. H.; Lee, J. H. *Progress in Materials Science* **2012**, *57*, 1061–1105.

[17] Blake, P.; Brimicombe, P. D.; Nair, R. R.; Booth, T. J.; Jiang, D.; Schedin, F.; Ponomarenko, L. a.; Morozov, S. V.; Gleeson, H. F.; Hill, E. W.; Geim, A. K.; Novoselov, K. S. *Nano Letters* **2008**, *8*, 1704–1708.

[18] Paton, K. R.; et al., *Nature Materials* **2014**, *13*, 624–630.

[19] Dreyer, D. R.; Ruoff, R. S.; Bielawski, C. W. **2010**, *49*, 9336–9344.

[20] Torrisi, F.; Hasan, T.; Wu, W.; Sun, Z.; Lombardo, A.; Kulmala, T. S.; Hsieh, G. W.; Jung, S.; Bonaccorso, F.; Paul, P. J.; Chu, D.; Ferrari, A. C. *ACS Nano* **2012**, *6*, 2992–3006.

[21] Forbeaux, I.; Themlin, J.-M.; Debever, J.-M. *Physical Review B* **1998**, *58*, 16396–16406.

[22] Berger, C.; Wu, X.; Brown, N.; Naud, C.; Li, X.; Song, Z.; Mayou, D.; Li, T.; Hass, J.; Marchenkov, A.; Conrad, E. H.; First, P. N.; De Heer, W. a. *Science* **2006**, *312*, 1191–1196.

[23] Emtsev, K. V.; Bostwick, A.; Horn, K.; Jobst, J.; Kellogg, G. L.; Ley, L.; McChesney, J. L.; Ohta, T.; Reshanov, S. a.; Röhrl, J.; Rotenberg, E.; Schmid, A. K.; Waldmann, D.; Weber, H. B.; Seyller, T. *Nature materials* **2009**, *8*, 203–207.

[24] Berger, C.; Song, Z.; Li, T.; Li, X.; Ogbazghi, A. Y.; Feng, R.; Dai, Z.; Marchenkov, A. N.; Conrad, E. H.; First, P. N.; de Heer, W. a. *The Journal of Physical Chemistry B* **2004**, *108*, 19912–19916.

[25] Ohta, T.; Bostwick, A.; Seyller, T.; Horn, K.; Rotenberg, E. *Science* **2006**, *313*, 951–954.

[26] Virojanadara, C.; Syväjarvi, M.; Yakimova, R.; Johansson, L. I.; Zakharov, A. A.; Balasubramanian, T. *Physical Review B* **2008**, *78*, 245403.

[27] Cai, J.; Ruffieux, P.; Jaafar, R.; Bieri, M.; Braun, T.; Blankenburg, S.; Muoth, M.; Seitsonen, A. P.; Saleh, M.; Feng, X.; Müllen, K.; Fasel, R. *Nature* **2010**, *466*, 470–473.

[28] Chen, Y.-C.; de Oteyza, D. G.; Pedramrazi, Z.; Chen, C.; Fischer, F. R.; Crommie, M. F. *ACS Nano* **2013**, *7*, 6123–8.

[29] Han, P.; Akagi, K.; Canova, F. F.; Mutoh, H.; Shiraki, S.; Iwaya, K.; Weiss, P. S.; Asao, N.; Hitosugi, T. *ACS Nano* **2014**, *8*, 9181–9187.

[30] Bennett, P. B.; Pedramrazi, Z.; Madani, A.; Chen, Y. C.; De Oteyza, D. G.; Chen, C.; Fischer, F. R.; Crommie, M. F.; Bokor, J. *Applied Physics Letters* **2013**, *103*, 1–5.

[31] Zhang, Y.; Zhang, L.; Zhou, C. *Accounts of Chemical Research* **2013**, *46*, 2329–2339.

[32] Li, X.; Cai, W.; An, J.; Kim, S.; Nah, J.; Yang, D.; Piner, R.; Velamakanni, A.; Inhwa, J.; Emanuel, T.; Banerjee, S. K.; Colombo, L.; Ruoff, R. S. *Science* **2009**, *324*, 1312–1314.

[33] Geim, A. K.; Novoselov, K. S. *Nature materials* **2007**, *7*, 183–191.

[34] Lin, L.; Liu, Z. *Nature materials* **2016**, *15*, 2015–2016.

[35] Batzill, M. *Surface Science Reports* **2012**, *67*, 83–115.

[36] Vinogradov, N. A.; Zakharov, A. A.; Kocevski, V. *Physical Review Letters* **2012**, *026101*, 1–5.

[37] Varykhalov, a.; Sánchez-Barriga, J.; Shikin, a.; Biswas, C.; Vescovo, E.; Rybkin, a.; Marchenko, D.; Rader, O. *Physical Review Letters* **2008**, *101*, 157601.

[38] Rosei, R.; De Crescenzi, M.; Sette, F.; Quaresima, C.; Savoia, A.; Perfetti, P. *Physical Review B* **1983**, *28*, 1161–1164.

[39] Dahal, A.; Addou, R.; Sutter, P.; Batzill, M. *Applied Physics Letters* **2012**, *100*, 241602.

[40] Weatherup, R.; Dlubak, B.; Hofmann, S. *ACS Nano* **2012**, *6*, 9996–10003.

[41] Reina, A.; Thiele, S.; Jia, X. *Nano Research* **2009**, *9*, 30–35.

[42] Binnig, G.; Rohrer, H. *Surface Science* **1983**, *126*, 236–244.

[43] Bardeen, J. *Physical review letters* **1961**, *6*, 57–59.

[44] Tersoff, J. and Hamann, D. R. *Physical Review B* **1985**, *31*, 805–813.

[45] Esch, F.; Dri, C.; Spessot, A.; Africh, C.; Cautero, G.; Giuressi, D.; Sergo, R.; Tommasini, R.; Comelli, G. *Review of Scientific Instruments* **2011**, *82*, 053702.

[46] Rost, M. J. et al. *Review of Scientific Instruments* **2005**, *76*, 053710.

[47] Rost, M. J.; van Baarle, G. J. C.; Katan, a. J.; van Spengen, W. M.; Schakel, P.; van Loo, W. a.; Oosterkamp, T. H.; Frenken, J. W. M. *Asian Journal of Control* **2009**, *11*, 110–129.

[48] Brune, H.; Wintterlin, J.; Trost, J.; Ertl, G.; Wiechers, J.; Behm, R. J. *The Journal of Chemical Physics* **1993**, *99*, 2128.

[49] Wintterlin, J.; Trost, J.; Renisch, S.; Schuster, R.; Zambelli, T.; Ertl, G. *Surface Science* **1997**, *394*, 159–169.

[50] Dri, C.; Esch, F.; Africh, C.; Comelli, G. *Measurement Science and Technology* **2012**, *23*, 055402.

[51] Seah, M. P.; Briggs, D. *Practical Surface Analysis: Auger and X-ray Photoelectron Spectroscopy*; John Wiley & Sons, 1990.

[52] Briggs, D.; Seah, M. P. *D. Briggs, & M. P. Seah,(Editors), John Wiley & Sons, Chichester 1983, xiv+ 533* **1983**,

[53] Zangwill, A. *Physics at surfaces*; Cambridge University Press, 1988.

[54] Wood, E. A. *Journal of applied physics* **1964**, *35*, 1306–1312.

[55] Moulder, J. F.; Chastain, J.; King, R. C. *Handbook of X-ray photoelectron spectroscopy: a reference book of standard spectra for identification and interpretation of XPS data*; Perkin-Elmer Eden Prairie, MN, 1992.

[56] Doniach, S.; Sunjic, M. *Journal of Physics C: Solid State Physics* **1970**, *3*, 285.

[57] Higashiguchi, M.; Shimada, K.; Arita, M.; Miura, Y.; Tobita, N.; Cui, X.; Aiura, Y.; Namatame, H.; Taniguchi, M. *Surface Science* **2007**, *601*, 4005–4009.

[58] Bauer, E. *Reports on Progress in Physics* **1994**, *57*, 895–938.

[59] Bauer, E. *Surface Review and Letters* **1998**, *5*, 1275–1286.

[60] Veneklasen, L. H. *Ultramicroscopy* **1991**, *36*, 76–90.

[61] Menteş, T. O.; Zamborlini, G.; Sala, A.; Locatelli, A. *Beilstein Journal of Nanotechnology* **2014**, *5*, 1873–1886.

[62] Mitchell, K. *Contemporary Physics* **1973**, *14*, 251–271.

[63] Locatelli, A.; Aballe, L.; Menteş, T. O.; Kiskinova, M.; Bauer, E. *Surface and Interface Analysis* **2006**, *38*, 1554–1557.

[64] Locatelli, A.; Bauer, E. *Journal of Physics: Condensed Matter* **2008**, *20*, 093002.

[65] Bianchini, F.; Patera, L. L.; Peressi, M.; Africh, C.; Comelli, G. *Journal of Physical Chemistry Letters* **2014**, *5*, 467–473.

[66] Africh, C.; Cepek, C.; Patera, L. L.; Zamborlini, G.; Genoni, P.; Menteş, T. O.; Sala, A.; Locatelli, A.; Comelli, G. *Scientific reports* **2016**, *6*, 19734.

[67] Shelton, J.; Patil, H.; Blakely, J. *Surface Science* **1974**, *43*, 493–520.

[68] Eizenberg, M.; Blakely, J. M. *The Journal of Chemical Physics* **1979**, *71*, 3467–3477.

[69] Gamo, Y.; Nagashima, a.; Wakabayashi, M.; Terai, M.; Oshima, C. *Surface Science* **1997**, *374*, 61–64.

[70] Bertoni, G.; Calmels, L.; Altibelli, A.; Serin, V. *Physical Review B* **2005**, *71*, 075402.

[71] Fuentes-Cabrera, M.; Baskes, M.; Melechko, A.; Simpson, M. *Physical Review B* **2008**, *77*, 035405.

[72] Zhao, W.; Kozlov, S. M.; Oliver, H.; Gotterbarm, K.; Lorenz, M. P. a.; Viñes, F.; Papp, C.; Andreas, G.; Steinrück, H.-P. *The Journal of chemical physics Letters* **2011**, *2*, 759–764.

[73] Kozlov, S. M.; Viñes, F.; Görling, A. *Journal of Physical Chemistry C* **2012**, *116*, 7360–7366.

[74] Lahiri, J.; Lin, Y.; Bozkurt, P.; Oleynik, I. I.; Batzill, M. *Nature nanotechnology* **2010**, *5*, 326–329.

[75] Sun, X.; Entani, S.; Yamauchi, Y.; Pratt, A.; Kurahashi, M. *Journal of Applied Physics* **2013**, *114*, 143713.

[76] Kang, M.; Jung, S.; Park, J. *Physical Review B* **2010**, *82*, 085409.

[77] Dzemiantsova, L.; Karolak, M.; Lofink, F. *Physical Review B* **2011**, *84*, 205431.

[78] Mittendorfer, F.; Garhofer, A.; Redinger, J.; Klimeš, J. *Physical Review B* **2011**, *84*, 201401.

[79] Hamada, I.; Otani, M. *Physical Review B* **2010**, *82*, 153412.

[80] Kolb, D.; Simeone, F. *Electrochimica Acta* **2005**, *50*, 2989–2996.

[81] Zeller, P.; Günther, S. *New Journal of Physics* **2014**, *16*, 083028.

[82] Zhang, X.; Xu, Z.; Hui, L.; Xin, J.; Ding, F. *The Journal of Physical Chemistry Letters* **2012**, *3*, 2822–2827.

[83] Klink, C.; Stensgaard, I.; Besenbacher, F.; Lægsgaard, E. *Surface Science* **1995**, *342*, 250–260.

[84] Locatelli, A.; Wang, C.; Africh, C.; Stojić, N.; Menteş, T. O.; Comelli, G.; Binggeli, N. *ACS Nano* **2013**, *7*, 6955–63.

[85] Gottardi, S.; Mu, K.; Bignardi, L.; Moreno-lo, J. C.; Pham, T. A.; Ivashenko, O.; Yablonskikh, M.; Barinov, A.; Bjo, J.; Rudolf, P.; Sto, M. *Nano Letters* **2015**, *15*, 917–922.

[86] Usachov, D.; Fedorov, A.; Otrokov, M. M.; Chikina, A.; Vilkov, O.; Petukhov, A.; Rybkin, A. G.; Koroteev, Y. M.; Chulkov, E. V.; Adamchuk, V. K.; Grüneis, A.; Laubschat, C.; Vyalikh, D. V. *Nano Letters* **2015**, *15*, 2396–2401.

[87] Sutter, P.; Hybertsen, M. S.; Sadowski, J. T.; Sutter, E. *Nano letters* **2009**, *9*, 2654–60.

[88] Voloshina, E. N.; Generalov, A.; Weser, M.; Böttcher, S.; Horn, K.; Dedkov, Y. S. *New Journal of Physics* **2011**, *13*, 113028.

[89] Sutter, P.; Sadowski, J. T.; Sutter, E. *Physical Review B - Condensed Matter and Materials Physics* **2009**, *80*, 245411.

[90] Lizzit, S.; Larciprete, R.; Lacovig, P.; Dalmiglio, M.; Orlando, F.; Baraldi, A.; Gammelgaard, L.; Barreto, L.; Bianchi, M.; Perkins, E.; Hofmann, P. *Nano Letters* **2012**, *12*, 4503–4507.

[91] Omiciuolo, L.; Hernàndez, E. R.; Miniussi, E.; Orlando, F.; Lacovig, P.; Lizzit, S.; Menteş, T. O.; Locatelli, A.; Larciprete, R.; Bianchi, M.; Ulstrup, S.; Hofmann, P.; Baraldi, A. *Nature communications* **2014**, *5*, 1–8.

[92] Leicht, P.; Zielke, L.; Bouvron, S.; Moroni, R. *ACS Nano* **2014**, *8*, 3735–3742.

[93] Addou, R.; Dahal, A.; Sutter, P.; Batzill, M. *Applied Physics Letters* **2012**, *100*, 021601.

[94] Patera, L. L.; Africh, C.; Weatherup, R. S.; Blume, R.; Bhardwaj, S.; Castellarin-Cudia, C.; Knop-Gericke, A.; Schloegl, R.; Comelli, G.; Hofmann, S.; Cepek, C. *ACS Nano* **2013**, *7*, 7901–7912.

[95] Tanuma, S.; Powell, C. J.; Penn, D. R. *Surface And Interface Analysis* **2011**, *43*, 689–713.

[96] Miniussi, E.; Pozzo, M.; Baraldi, A.; Vesselli, E. *Physical Review Letters* **2011**, *216101*, 2–5.

[97] Dedkov, Y. S.; Fonin, M.; Rüdiger, U.; Laubschat, C. *Physical Review Letters* **2008**, *100*, 107602.

[98] Varykhalov, A.; Marchenko, D.; Sánchez-Barriga, J.; Scholz, M. R.; Verberck, B.; Trauzettel, B.; Wehling, T. O.; Carbone, C.; Rader, O. *Physical Review X* **2012**, *2*, 041017.

[99] Karpan, V. M.; Giovannetti, G.; Khomyakov, P. a.; Talanana, M.; Starikov, a. a.; Zwierzycki, M.; Van Den Brink, J.; Brocks, G.; Kelly, P. J. *Physical Review Letters* **2007**, *99*, 176602.

[100] Menteş, T. O.; Locatelli, A. *Journal of Electron Spectroscopy and Related Phenomena* **2012**, *185*, 323–329.

[101] Blakely, J. M.; Kim, J. S.; Potter, H. C. *Journal of Applied Physics* **1970**, *41*, 2693–2697.

[102] Li, X.; Cai, W.; Colombo, L.; Ruoff, R. *Nano letters* **2009**, *12*, 4268–4272.

[103] Odahara, G.; Otani, S.; Oshima, C.; Suzuki, M.; Yasue, T.; Koshikawa, T. *Surface Science* **2011**, *605*, 1095–1098.

[104] Yu, Q.; Lian, J.; Siriponglert, S.; Li, H.; Chen, Y.; Pei, S. *Applied Physics Letters* **2008**, *93*, 113103.

[105] Vang, R. T.; Honkala, K.; Dahl, S.; Vestergaard, E. K.; Schnadt, J.; Lægsgaard, E.; Clausen, B. S.; Nørskov, J. K.; Besenbacher, F. *Surface Science* **2006**, *600*, 66–77.

[106] Bluhm, H.; Havecker, M.; Knop-Gericke, A. *MRS Bulletin* **2008**, *32*, 1022–1030.

[107] Dong, G. C.; van Baarle, D. W.; Rost, M. J.; Frenken, J. W. M. *New Journal of Physics* **2012**, *14*, 053033.

[108] Günther, S.; Dänhardt, S.; Wang, B.; Bocquet, M.-L.; Schmitt, S.; Wintterlin, J. *Nano letters* **2011**, *11*, 1895–900.

[109] Starodub, E.; Maier, S.; Stass, I.; Bartelt, N. C.; Feibelman, P. J.; Salmeron, M.; McCarty, K. F. *Physical Review B* **2009**, *80*, 235422.

[110] Arnoult, W. J.; McLellan, R. B. *Scripta Metallurgica* **1972**, *6*, 1013–1018.

[111] Wirth, C. T.; Bayer, B. C.; Gamalski, A. D.; Esconjauregui, S.; Weatherup, R. S.; Ducati, C.; Baehtz, C.; Robertson, J.; Hofmann, S. *Chemistry of Materials* **2012**, *24*, 4633–4640.

[112] Patera, L. L.; Bianchini, F.; Troiano, G.; Dri, C.; Cepek, C.; Peressi, M.; Africh, C.; Comelli, G. *Nano Letters* **2015**, *15*, 56–62.

[113] Ritter, K. A.; Lyding, J. W. *Nature materials* **2009**, *8*, 235–242.

[114] Fujii, S.; Enoki, T. *Accounts of Chemical Research* **2013**, *46*, 2202–2210.

[115] Lee, H.; Son, Y.-W.; Park, N.; Han, S.; Yu, J. *Physical Review B* **2005**, *72*, 174431.

[116] Yazyev, O.; Katsnelson, M. *Physical Review Letters* **2008**, *100*, 047209.

[117] Ohtsuka, M.; Fujii, S.; Kiguchi, M.; Enoki, T. *ACS Nano* **2013**, *7*, 6868–6874.

[118] Hod, O.; Barone, V.; Peralta, J. E.; Scuseria, G. E. *Nano letters* **2007**, *7*, 2295–2299.

[119] Jiang, D.-e.; Sumpter, B. G.; Dai, S. *The Journal of chemical physics* **2007**, *126*, 134701.

[120] Tao, C.; Jiao, L.; Yazyev, O. V.; Chen, Y.-C.; Feng, J.; Zhang, X.; Capaz, R. B.; Tour, J. M.; Zettl, A.; Louie, S. G.; Dai, H.; Crommie, M. F. *Nature Physics* **2011**, *7*, 616–620.

[121] Rozhkov, A. V.; Giavaras, G.; Bliokh, Y. P.; Freilikher, V.; Nori, F. *Physics Reports* **2011**, *503*, 77–114.

[122] Kawai, T.; Miyamoto, Y.; Sugino, O.; Koga, Y. *Physical Review B* **2000**, *62*, R16349–R16352.

[123] Girit, a. .; Meyer, J. C.; Erni, R.; Rossell, M. D.; Kisielowski, C.; Yang, L.; Park, C.-H.; Crommie, M. F.; Cohen, M. L.; Louie, S. G.; Zettl, A. *Science* **2009**, *323*, 1705–1708.

[124] Wassmann, T.; Seitsonen, A. P.; Saitta, A. M.; Lazzeri, M.; Mauri, F. *Physical Review Letters* **2008**, *101*, 096402.

[125] Wassmann, T.; Seitsonen, A. P.; Saitta, A. M.; Lazzeri, M.; Mauri, F. *Physica Status Solidi (B)* **2009**, *246*, 2586–2591.

[126] Koskinen, P.; Malola, S.; Häkkinen, H. *Physical Review Letters* **2008**, *101*, 1–4.

[127] Koskinen, P.; Malola, S.; Häkkinen, H. *Physical Review B* **2009**, *80*, 073401.

[128] Klein, D. *Chemical Physics Letters* **1994**, *217*, 261–265.

[129] Kobayashi, Y.; Fukui, K.; Enoki, T. *Physical Review B* **2005**, *71*, 193406.

[130] Ivanovskaya, V. V.; Zobelli, A.; Wagner, P.; Heggie, M. I.; Briddon, P. R.; Rayson, M. J.; Ewels, C. P. *Physical Review Letters* **2011**, *107*, 065502.

[131] Li, Y.; Subramaniam, D.; Atodiresei, N.; Lazic, P.; Caciuc, V.; Pauly, C.; Georgi, A.; Busse, C.; Liebmann, M.; Blügel, S.; Pratzer, M.; Morgenstern, M.; Mazzarello, R. *Advanced materials* **2013**, *25*, 1967–1972.

[132] Subramaniam, D.; Libisch, F.; Li, Y.; Pauly, C.; Geringer, V.; Reiter, R.; Mashoff, T.; Liebmann, M.; Burgdörfer, J.; Busse, C.; Michely, T.; Mazzarello, R.; Pratzer, M.; Morgenstern, M. *Physical Review Letters* **2012**, *108*, 046801.

[133] Phark, S.-H.; Borme, J.; Vanegas, A. L.; Corbetta, M.; Sander, D.; Kirschner, J. *ACS Nano* **2011**, *5*, 8162–8166.

[134] Tian, J.; Cao, H.; Wu, W.; Yu, Q.; Chen, Y. P. *Nano letters* **2011**, *11*, 3663–3668.

[135] Garcia-Lekue, A.; Balashov, T.; Olle, M.; Ceballos, G.; Arnau, A.; Gambardella, P.; Sanchez-Portal, D.; Mugarza, A. *Physical Review Letters* **2014**, *112*, 066802.

[136] Gao, J.; Zhao, J.; Ding, F. *Journal of the American Chemical Society* **2012**, *134*, 6204–6209.

[137] Olle, M.; Ceballos, G.; Serrate, D.; Gambardella, P. *Nano letters* **2012**, *12*, 4431–4436.

[138] Lacovig, P.; Pozzo, M.; Alfè, D.; Vilmercati, P.; Baraldi, A.; Lizzit, S. *Physical Review Letters* **2009**, *103*, 166101.

[139] Artyukhov, V. I.; Liu, Y.; Yakobson, B. I. *Proceedings of the National Academy of Sciences of the United States of America* **2012**, *109*, 15136–15140.

[140] Shu, H.; Chen, X.; Tao, X.; Ding, F. *ACS Nano* **2012**, *6*, 3243–3250.

[141] Zhang, X.; Wang, L.; Xin, J.; Yakobson, B. I.; Ding, F. *Journal of the American Chemical Society* **2014**, *136*, 3040–3047.

[142] Artyukhov, V.; Hao, Y.; Ruoff, R.; Yakobson, B. *Physical Review Letters* **2015**, *114*, 115502.

[143] Prezzi, D.; Eom, D.; Rim, K. T.; Zhou, H.; Xiao, S.; Nuckolls, C.; Heinz, T. F.; Flynn, G. W.; Hybertsen, M. S. *ACS Nano* **2014**, *8*, 5765–5773.

[144] Garcia-Lekue, a.; Ollé, M.; Sanchez-Portal, D.; Palacios, J. J.; Mugarza, A.; Ceballos, G.; Gambardella, P. *The Journal of Physical Chemistry C* **2015**, *119*, 4072–4078.

[145] Dinger, A.; Lutterloh, C.; Biener, J.; Küppers, J. *Surface science* **1999**, *421*, 17–26.

[146] Robota, H.; Vielhaber, W.; Lin, M.; Segner, J.; Ertl, G. *Surface Science* **1985**, *155*, 101–120.

[147] Kresse, G. *Physical Review B* **2000**, *62*, 8295–8305.

[148] Liu, B.; Lusk, M. T.; Ely, J. F. *The Journal of Physical Chemistry C* **2009**, *113*, 13715–13722.

[149] Candelaria, S. L.; Shao, Y.; Zhou, W.; Li, X.; Xiao, J.; Zhang, J.-G.; Wang, Y.; Liu, J.; Li, J.; Cao, G. *Nano Energy* **2012**, *1*, 195–220.

[150] Choi, M. H.; Min, Y. J.; Gwak, G. H.; Paek, S. M.; Oh, J. M. *Journal of Alloys and Compounds* **2014**, *610*, 231–235.

[151] Meng, L.; Wang, Z.; Jiang, J.; Yang, Y.; Wang, J. *The Journal of Physical Chemistry C* **2013**, *117*, 15260–15265.

[152] Hammer, B.; Nørskov, J. K. *Nature* **1995**, *376*, 238–240.

[153] Qiao, B.; Wang, A.; Yang, X.; Allard, L. F.; Jiang, Z.; Cui, Y.; Liu, J.; Li, J.; Zhang, T. *Nature chemistry* **2011**, *3*, 634–41.

[154] Sedona, F.; Di Marino, M.; Forrer, D.; Vittadini, a.; Casarin, M.; Cossaro, a.; Floreano, L.; Verdini, a.; Sambi, M. *Nature materials* **2012**, *11*, 970–7.

[155] Kiskinova, M. *Chemical review* **1996**, *96*, 1431–1447.

[156] Bartels, L. *Nature chemistry* **2010**, *2*, 87–95.

[157] Yang, Y. C.; Taranovskyy, A.; Magnussen, O. M. *Angewandte Chemie - International Edition* **2012**, *51*, 1966–1969.

[158] Perry, C.; Haq, S.; Frederick, B.; Richardson, N. *Surface Science* **1998**, *409*, 512–520.

[159] Wang, W. L.; Santos, E. J. G.; Jiang, B.; Cubuk, E. D.; Ophus, C.; Centeno, A.; Pesquera, A.; Zurutuza, A.; Ciston, J.; Westervelt, R.; Kaxiras, E. *Nano Letters* **2014**, *14*, 450–455.

[160] Zhao, J.; Deng, Q.; Avdoshenko, S. M.; Fu, L.; Eckert, J.; Rümmeli, M. H. *Proceedings of the National Academy of Sciences* **2014**, *111*, 15641–15646.

[161] Ehrlich, G. *Surface Science* **1991**, *246*, 1–12.

[162] Linderoth, T. R.; Horch, S.; Lægsgaard, E.; Stensgaard, I.; Besenbacher, F. *Physical Review Letters* **1997**, *78*, 4978–4981.

[163] Pai, W.; Swan, A.; Zhang, Z.; Wendelken, J. *Physical Review Letters* **1997**, *79*, 3210–3213.

[164] Morgenstern, K.; Rosenfeld, G.; Lægsgaard, E.; Besenbacher, F.; Comsa, G. *Physical Review Letters* **1998**, *80*, 556–559.

[165] Wang, L.; Zhang, X.; Chan, H. L.; Yan, F.; Ding, F. *Journal of the American Chemical Society* **2013**, *135*, 4476–4482.

[166] Rogge, P.; Nie, S.; McCarty, K.; Bartelt, N.; Dubon, O. *Nano letters* **2014**, *15*, 170–175.

[167] Rutter, G. M.; Crain, J. N.; Guisinger, N. P.; Li, T.; First, P. N.; Stroscio, J. a. *Science* **2007**, *317*, 219–222.

[168] Banhart, F.; Kotakoski, J.; Krasheninnikov, A. *ACS Nano* **2010**, *5*, 26–41.

[169] Ugeda, M. M.; Brihuega, I.; Guinea, F.; Gómez-Rodríguez, J. M. *Physical Review Letters* **2010**, *104*, 096804.

[170] Ugeda, M. M.; Fernández-Torre, D.; Brihuega, I.; Pou, P.; Martínez-Galera, a. J.; Pérez, R.; Gómez-Rodríguez, J. M. *Physical Review Letters* **2011**, *107*, 116803.

[171] Zhao, L. et al. *Science* **2011**, *333*, 999–1003.

[172] Zhao, L.; Levendorf, M.; Goncher, S.; Schiros, T.; Pálová, L.; Zabet-Khosousi, A.; Rim, K. T.; Gutiérrez, C.; Nordlund, D.; Jaye, C.; Hybertsen, M.; Reichman, D.; Flynn, G. W.; Park, J.; Pasupathy, A. N. *Nano Letters* **2013**, *13*, 4659–4665.

[173] Telychko, M.; Mutombo, P.; Ondráček, M.; Hapala, P.; Bocquet, F. C.; Kolorenč, J.; Vondráček, M.; Jelínek, P.; Svec, M. *ACS Nano* **2014**, *8*, 7318–7324.

[174] Sala, A.; Zamborlini, G.; Menteş, T. O.; Locatelli, A. *Small* **2015**, *11*, 592–5931.

[175] Krasheninnikov, a. V.; Lehtinen, P. O.; Foster, a. S.; Pyykkö, P.; Nieminen, R. M. *Physical Review Letters* **2009**, *102*, 2–5.

[176] Kaukonen, M. O.; Krasheninnikov, A.; Kauppinen, E.; Nieminen, R. M. *ACS Catalysis* **2012**, *3*, 159–165.

[177] Wannakao, S.; Nongnual, T.; Khongpracha, P.; Maihom, T.; Limtrakul, J. *The Journal of Physical Chemistry C* **2012**, *116*, 16992–16998.

[178] Sicot, M.; Leicht, P.; Zusan, A.; Bouvron, S.; Zander, O.; Weser, M.; Dedkov, Y. S.; Horn, K.; Fonin, M. *ACS Nano* **2012**, *6*, 151–158.

[179] Tapasztó, L.; Nemes-Incze, P. *Applied Physics Letters* **2012**, *100*, 053114.

[180] Koepke, J. C.; Wood, J. D.; Estrada, D.; Ong, Z. Y.; He, K. T.; Pop, E.; Lyding, J. W. *ACS Nano* **2013**, *7*, 75–86.

[181] Sutter, E.; Albrecht, P.; Sutter, P. *Applied Physics Letters* **2009**, *133109*, 5–8.

[182] Pelc, M.; Chico, L.; Ayuela, a.; Jaskólski, W. *Physical Review B* **2013**, *87*, 165427.

[183] Lin, X.; Ni, J. *Physical Review B* **2011**, *84*, 075461.

[184] Kou, L.; Tang, C.; Guo, W.; Chen, C. *ACS Nano* **2011**, *5*, 1012–1017.

[185] Kan, M.; Zhou, J.; Sun, Q.; Wang, Q.; Kawazoe, Y.; Jena, P. *Physical Review B* **2012**, *85*, 155450.

[186] Dai, Q. Q.; Zhu, Y. F.; Jiang, Q. *The Journal of Physical Chemistry C* **2013**, *117*, 4791–4799.

[187] Carcia, P. F.; McLean, R. S.; Reilly, M. H.; Nunes, G. *Applied Physics Letters* **2003**, *82*, 1117–1119.

[188] Balog, R. et al. *Nature materials* **2010**, *9*, 315–9.

[189] Zhang, Y.; Tang, T.-T.; Girit, C.; Hao, Z.; Martin, M. C.; Zettl, A.; Crommie, M. F.; Shen, Y. R.; Wang, F. *Nature* **2009**, *459*, 820–823.

[190] Kim, K. S.; Walter, A. L.; Moreschini, L.; Seyller, T.; Horn, K.; Rotenberg, E.; Bostwick, A. *Nature Materials* **2013**, *12*, 887–892.

[191] Zhou, S.; Gweon, G.-H.; Fedorov, A.; First, P.; De Heer, W.; Lee, D.-H.; Guinea, F.; Neto, A. C.; Lanzara, A. *Nature materials* **2007**, *6*, 770–775.

[192] Nie, S.; Walter, A. L.; Bartelt, N. C.; Starodub, E.; Bostwick, A.; Rotenberg, E.; McCarty, K. F. *ACS Nano* **2011**, *5*, 2298–2306.

[193] Li, Q.; Chou, H.; Zhong, J. H.; Liu, J. Y.; Dolocan, A.; Zhang, J.; Zhou, Y.; Ruoff, R. S.; Chen, S.; Cai, W. *Nano Letters* **2013**, *13*, 486–490.

[194] Yan, K.; Peng, H.; Zhou, Y.; Li, H.; Liu, Z. *Nano Letters* **2011**, *11*, 1106–1110.

[195] Zhang, Y.; Gao, T.; Xie, S.; Dai, B.; Fu, L.; Gao, Y.; Chen, Y.; Liu, M.; Liu, Z. *Nano Research* **2012**, *5*, 402–411.

[196] Locatelli, A.; Knox, K. R.; Cvetko, D.; Menteş, T. O.; Nino, M. A.; Wang, S.; Yilmaz, M. B.; Kim, P.; Osgood Jr, R. M.; Morgante, A. *ACS Nano* **2010**, *4*, 4879–4889.

[197] Díaz, J.; Paolicelli, G.; Ferrer, S.; Comin, F. *Physical Review B* **1996**, *54*, 8064.

[198] Iwasaki, T.; Zakharov, A. a.; Eelbo, T.; Waśniowska, M.; Wiesendanger, R.; Smet, J. H.; Starke, U. *Surface Science* **2014**, *625*, 44–49.

[199] Mathieu, C.; Barrett, N.; Rault, J.; Mi, Y.; Zhang, B.; De Heer, W.; Berger, C.; Conrad, E.; Renault, O. *Physical Review B* **2011**, *83*, 235436.

[200] Chernozatonskiĭ, L. A.; Sorokin, P. B.; Belova, E. É.; Brüning, J.; Fedorov, A. S. *JETP Letters* **2007**, *85*, 77–81.

[201] Ruffieux, P.; Melle-Franco, M.; Gröning, O.; Bielmann, M.; Zerbetto, F.; Gröning, P. *Physical Review B* **2005**, *71*, 153403.

List of abbreviations

AC	Armchair
ADC	Analog-to-Digital Converter
ARPES	Angle-Resolved PhotoEmission Spectroscopy
BF	Bright Field
BZ	Brillouin Zone
BLG	Bi-Layer Graphene
CCD	Charge-Coupled Device
CVD	Chemical Vapour Deposition
DAC	Digital-to-Analog Converter
DF	Dark Field
DFT	Density Functional Theory
EG	Epitaxial Graphene
FAST	Fast Acquisition of SPM Time-series
FFT	Fast Fourier Transform
FPGA	Full Programmable Gate Array
GGA	Generalized Gradient Approximation
HRTEM	High-Resolution Transmission Electron Microscopy
ILDOS	Integrated Local Density Of States
k	Klein
LDA	Local Density Approximation

LDOS	Local Density Of States
LEED	Low Energy Electron Diffraction
LEEM	Low Energy Electron Microscopy
MDC	Momentum Distribution Curves
MLG	Mono-Layer Graphene
PEEM	PhotoEmission Electron Microscopy
PBN	Pyrolitic-Boron Nitride
RG	Rotated Graphene
RGC	Rotated Graphene on Carbide
RGA	Residual Gas Analyzer
rk	Reconstructed Klein
RT	Room Temperature
SPELEEM	Spectroscopic Photo-Emission and Low Energy Electron Microscope
STM	Scanning Tunneling Microscopy
UHV	Ultra High Vacuum
VT-STM	Variable Temperature Scanning Tunneling Microscope
XAS	X-ray Absorption Spectroscopy
XPEEM	X-rays PhotoEmission Electron Microscopy
XPS	X-ray Photoemission Spectroscopy
z	zigzag